약학박사학위논문

나노구조체 기반
약물 표적 전달 및 광열치료

Nanostructure-based targeted drug delivery

and photothermal therapy

2017 년 2 월

서울대학교 대학원

약학과 약제과학전공

박 주 연

Abstract

Nanostructure-based targeted drug delivery and phototheramal therapy

Joo Yeon Park

Physical Pharmacy, Department of Pharmacy

The Graduate School

Seoul National University

Targeted drug delivery has been considered as a promising strategy to improve therapeutic effects of anticancer agents including chemicals and biomolecules. First, DNA polyaptamer nanothreads against protein tyrosine kinase 7 (PTK7) receptor anchored onto redcued graphene oxide (rGO) nanosheets (PNTrGO)

were prepared for targeted delivery. The polyaptamer was produced by rolling circle amplicifation (RCA) and introduced onto rGO nanosheets via high affinity between oligo-T sequence and rGO nanosheets. PNTrGO improved cellular uptake to PTK7 overexpressed cancer and enhanced tumor accumulation in tumor xenografted mice. Moreover, doxorubicin (Dox)-loaded PNTrGO enhanced the inhibition effect of tumor growth in PTK7-positive tumor bearing mice. Secondly, DNA nanoballs which are able to carry antisense oligonucleotide (ASO) and target to CD44 overexpressed cancer were developed. Two types of ASOs, Dz13 and OGX-427, were loaded to RCA product in complementary manner via hybridization. Furthermore, Mu peptide derived from adenovirus was condensed the ASO-loaded RCA product. Hyaluronic acid (HA) coating enhanced the cellular uptake of both Dz13 and OGX-427 to CD44-positive cancer cells, and reduced their target mRNA and proteins effectively. Photothermal therapy (PTT) has been investigated as potent and less invasive cancer treatment method. Boron nitride nanosheets (BNNSs) coated with tannic acid (TA) and iron film (TA-Fe/BNNSs) were prepared as novel and safe PTT agent. TA-Fe/BNNSs showed photothermal activity followed by NIR laser irradiation, and the photothermal effect of TA-Fe/BNNS was enough to eradicate tumor tissues after local administration to tumor-bearing mice. Lastly, gold nanocluster (AuNC)-loaded DNA nanoballs (AuDNBs) were designed as biocompatible PTT agent. AuNCs were synthesized with long single stranded DNA (ssDNA) produced by RCA and incorporated into the RCA product. The

assembly of AuNCs located in DNA nanoballs generated heat after NIR laser irradiation, and the anticancer effect was achieved by AuDNB treatment followed by NIR laser irradiation in cancer cells.

Keywords: Targeted drug delivery, photothermal therapy, rolling circle amplification, reduced graphene oxide, boron nitride nanosheet, tannic acid–Fe coating, gold nanocluster

Student Number: 2011-21722

Contents

List of Tables

List of Figures

List of Abbreviations

Abbreviation	Word
ARP	ASO-hybridized RCA product
ASOs	antisense oligonucleotides
ANOVA	analysis of variance
AuDNB	AuNC incorporated DNA nanoballs
AuNC	gold nanocluster
AuRP	RP mixed with gold ion
BNNS	boron nitride nanosheet
CCK-8	cell counting kit-8
Cy5.5	cyanine 5.5 dye
DAPI	4',6-diamidino-2-phenylindole dihydrochloride
DDS	drug delivery system
DMAB	dimethylamine borane
Dox	doxorubicin
EDS	energy dispersive spectrometer

EGFR	epidermal growth factor receptor
FAM	fluorescein
Fe/BNNS	iron-coated BNNS
GO	graphene oxide
HA	hyaluronic acid
hBN	hexagonal boron nitride
HER2	human epidermal growth factor receptor-2
HMA	HA-coated, Mu-condensed, dual ASO-hybridized DNA
MA	Mu-condensed, dual ASO-hybridized DNA
MTT	3-(4, 5-dimethylthiazol-2-yl)-2, 5-diphenyltetrazolium bromide
NIR	near-infrared
PBS	phosphate-buffered saline
PCNA	proliferating cell nuclear antigen
PEG	polyethylene glycol
PNTrGO	polyaptamer-anchored reduced graphene oxide

PCNA	proliferating cell nuclear antigen
PNTrGO	polyaptamer-anchored reduced graphene oxide
PSMA	prostate-specific membrane antigen
PTK7	protein tyrosine kinase 7
PTT	photothermal therapy
RCA	rolling circle amplification
RP	RCA product
rGO	reduced graphene oxide
ROX	6-carboxy-x-rhodamine
SEM	scanning electron microscopy
SNTrGO	scrambled polyaptamer-anchored reduced graphene oxide
ssDNA	single-stranded DNA
TA	tannic acid
TA/BNNS	TA-coated BNNS
TA-Fe/BNNS	TA and iron-coated BNNS
TDW	triple-distilled water
TEM	transmission electron microscopy
TGA	thermo-gravimetric analysis

TfR	transferrin receptor
TUNEL	terminal deoxynucleotidyl transferase dUTP nick-end labeling

Chapter I

Overview

1. Introduction

Drug delivery system (DDS) is a formulation, technology, or any type of approaches to achieve the effective effects of pharmaceutical compounds after administration to the body. To achieve desired therapeutic effects, improvement of solubility of hydrophobic drugs, control of drug release profile, change of administration routes, elongation of half-life of unstable drugs, and targeted delivery to specific cells or tissues has been demonstrated by various DDSs. Especially, since most of anticancer agents which are newly developed are hydrophobic and severely toxic, and there are many biomolecules which are developed for cancer therapy, drug delivery systems should be needed for cancer treatment.

Nanoparticle has been widely studied as a DDS system. Nanoparticles, such as polymeric nanoparticles, liposomes, nanoemulsions, and solid-lipid nanoparticles, can provide the improved delivery of anticancer agent against targeted tumor tissues [1]. Doxil® is the first commercially available liposomal drug delivery systems for cancer treatment [2]. Doxil® which is Dox-loaded polyethylene glycol (PEG) modified liposome delivered higher amount of drug to tumor tissues rather than naked Dox via enhanced permeability and retention (EPR)

effects [3,4]. Abraxane® is albumin conjugated paclitaxel to treat breast cancer and it was approved by FDA in 2005. Marqibo® is another liposomal anticancer drug delivery system which was approved by FDA in 2012. Large amount of efforts have been focused on development of efficient anticancer DDSs; however, only few drug delivery systems are commercially available. Although DDSs improved the pharmacokinetics of drugs, but passive targeting of nanoparticles is still not enough to eradicate cancer.

To enhance the delivery efficiency of anticancer drug, active targeted delivery systems have been investigated so far. Many researchers have reported that active targeting moiety which bound to a specific protein expressed on tumor cell membrane modified nanoparticles delivered their cargos to cancer selectively.

Stimuli-guided DDSs have been also reported recently to overcome limitation of traditional DDSs for remoting drug release or targeting specific area. Various exogenous stimuli like hyperthermia, ultrasound, and magnetic field have been applied to develop intelligent DDSs [5]. One of promising methods among exogenously controlled systems is photothermal therapy. Desired tumor tissues can be selectively irradiated by light after photothermal agent administration, and then it might induce cancer specific killing effect.

2. Targeted drug delivery systems for cancer treatment

For active tumor targeting, many kinds of proteins overexpressed onto cancer cells or cancer vasculature have been identified, and their binding molecules have been modified to nanoparticles.

Folate receptor, transferrin receptor (TfR), human epidermal growth factor receptor-2 (HER2), epidermal growth factor receptor (EGFR), integrin $\alpha_v\beta_3$ etc. are considered as target molecules to anticancer drug delivery (Table I-1). Especially, in active tumor targeted drug delivery systems, a ligand which binds to its target protein is introduced to the delivery system.

Various tumor targeting moieties have been adapted to nano drug delivery systems for tumor active targeting. Folate was conjugated to polymeric micelles [6,7], albumin nanoparticles [8,9], gold nanoparticles [10,11], and silica nanoparticles [12,13] to deliver anticancer drug efficiently, leading to enhancing the folate receptor overexpressed tumor killing effect both in vitro and in vivo. Folate as well as large molecules such as peptide [14,15], antibody [16,17], and nucleic acid aptamers [18,19] have been widely used with nanocarrier for tumor targeted systems. Additionally, multifunctional nanoparticles with more than one

targeting ligand for efficient drug delivery were demonstrated recently [20].

To develop an ideal active targeted system, overexpression of target proteins, high binding efficiency between ligand and the protein, ligand introduction method to the nanocarriers should be considered carefully [21].

Table I-1. Tumor cell surface proteins for active targeted drug delivery

Surface protein	Overexpressed cancer	Ligand	References
Folate receptor	Ovarian, breast cancer	Folic acid	[6-13]
Transferrin receptor (TfR)	Breast cancer, non-small cell lung cancer, glioma, non-Hodgkin's lymphoma	Transferrin, anti-TfR antibody	[22-27]
Epidermal growth factor receptor (EGFR)	Non-small cell lung cancer, squamous-cell lung carcinoma, pancreatic cancer, hepatocellular carcinoma	Anti-EGFR antibody	[28-32]
Human epidermal growth factor receptor-2 (HER2)	Breast, gastric, gastroesophageal cancers	Anti-HER2 antibody	[33-36]
Integrin $\alpha_v\beta_3$	Prostate, breast cancer, melanoma, non-small cell lung cancer	Cyclic RGD peptide	[14,15,37-39]
CD20	B cell lymphoma	Anti-CD20 antibody	[35,40,41]
CD44	Breast, lung, prostate, ovarian, cervical, and colorectal cancer, hepatocellular carcinoma and neuroblastoma	Hyaluronic acid, anti-CD44 antibody	[42-44]
Protein tyrosine kinase 7 (PTK7)	Colon, lung, gastric, breast cancer, acute myeloid leukemia	DNA aptamer	[45-47]
Prostate-specific membrane antigen (PSMA)	Prostate, colorectal, and gastric cancer	RNA aptamer, anti-PSMA antibody	[48-50]

3. Photothermal therapy for cancer treatment

Surgery is considered as a standard method to treat cancers. However, not all kinds of cancers can be removed by surgical resection because of tumor type, location, or patients' condition. Systemic chemotherapy and radiation therapy are also widely used as substitute or combination method of surgery. But these treatments could cause severe side effects such as hair loss, vomiting, skin redness due to high dose of anticancer drug or high energy of X-ray. Thus, local cancer treatment is a promising strategy to cure cancers. In this point of view, thermal ablation has been investigated for cancer treatment. Among thermal ablation methods such as radiofrequency ablation, microwave ablation, and high-intensity focused ultrasound, photothermal therapy (PTT) is considered as an attractive method to improve anticancer effect to target cancer cell specifically by cancer targeting photothermal agents.

PTT is a treatment to kill cancer via locally induced heat using photoresponsive agents followed by light irradiation. Due to its less-invasiveness, local targetability and escape recurrence, PTT is considered as a promising approach, especially for patients who suffer from various cancers having multi-drug resistance.

Diverse photoresponsive agents have been suggested for light-triggered nanomedicine. Photothermal agents convert absorbed light energy to heat. Cancer can be burned by local hyperthermia followed by irradiation. Gold nanoparticles [51,52], carbon-based nanostructures [53-55], organic polymers [56-58], and near-infrared (NIR) dyes [59,60] have been investigated as photothermal agents. These photothermal agents have common chemical structures to absorb light well, especially near-infrared light, and high photothermal conversion efficiency to achieve high anticancer effect. The representative photothermal agents including gold nanoparticles, carbon-based nanomaterials, NIR dyes, and organic polymers and their structures are shown in Fig. I-1.

For efficient PTT against cancer, sufficient amount of photothermal agents should be delivered and accumulated to tumor tissues before light irradiation. Low clearance rate of photothermal agents is also considered as toxicity issue of photothermal therapy [61]. Thus, to solve these problems, nano drug delivery technology is applied for PTT to maximize photothermal effect.

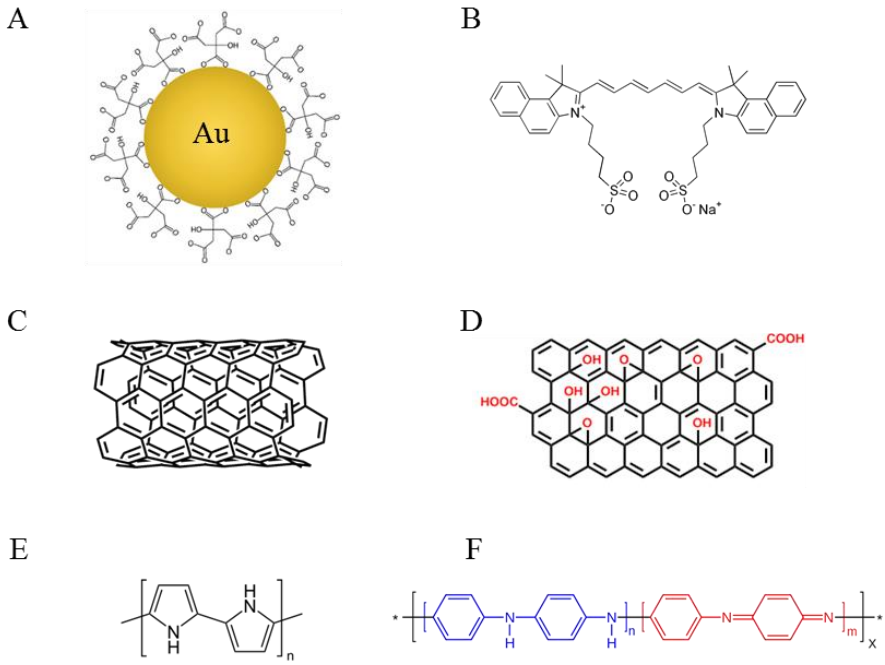

Fig.I-1. Representative photothermal agents.

(A) Citrate-stabilized gold nanoparticle (B) Indocyanine green (C) Carbon nanotube (D) Graphene oxide nanosheet (E) Polypyrrole (F) Polyaniline

4. Scope of the studies

Active targeted drug delivery systems have been considered as promising technology to treat cancer by overcoming limitations of conventional nanocarriers. Specificity against tumor tissues could reduce the side effects of anticancer drugs and improvement of cellular uptake to cancer cells. Thus, active targeted delivery systems for chemicals and antisense oligodeoxynucleotides (ASOs) were designed by using reduced graphene oxide (rGO) nanosheets and DNA nanoballs. Moreover, for efficient cancer treatment, polyphenol coated boron nitride nanosheets (BNNSs) and gold nanoclusters (AuNCs) incorporated DNA nanoballs were suggested as novel and biocompatible photothermal agents.

In chapter II, polyaptamer modified rGO was prepared for anticancer drug delivery to protein tyrosine kinase 7 (PTK7) receptor overexpressed leukemia cell specifically. Repeat of DNA apatmer which bound to PTK7 receptor was produced by rolling circle amplification and anchored onto reduced graphene oxide nanosheets via 22-mer oligoT sequence. The polyaptamer nanothreads modified-reduced graphene oxide nanosheets enhanced the cellular uptake upto 2.1–fold compared to that of scrambled polyaptamer anchored-reduced graphene oxide nanosheets.

In chapter III, biomimetic DNA nanoballs were developed for delivery of two different therapeutic ASOs. ASO loaded RCA product was condensed via Mu peptide and then coated with hyaluronic acid (HA). HA coated DNA nanoballs enhanced ASO delivery to CD44 overexpressed cancer cell line. Moreover, HA coated DNA nanoballs showed 5.9-fold higher tumor accumulation compared to DNA nanoballs without HA coating in cancer xenografted mice.

In chapter IV, BNNSs coated by tannic acid and iron complex was prepared for photothermal therapy. Tannic acid and iron chelate complex was effectively coated onto BNNSs and made them absorbing near-infrared (NIR) laser and generating heat. This polyphenol coated BNNS showed in vitro and in vivo anticancer effect followed by NIR laser irradiation.

In chapter V, DNA nanoballs which contained assembly of AuNCs were investigated as phototheraml agent. AuNCs were loaded inside of RCA product, and condensed the RCA product simultaneously. AuNC incorporated DNA nanoballs (AuDNBs) showed high photothermal activity after NIR laser irradiation, and induced anticancer effect when they were treated to the cancer cells with NIR laser irradiation; but did not without laser irradiation.

5. References

[1] Estanqueiro M, Amaral MH, Conceição J, Sousa Lobo JM. Nanotechnological carriers for cancer chemotherapy: the state of the art. Colloids Surf B Biointerfaces. 2015; 126: 631-648.

[2] Barenholz Y. Doxil® — The first FDA-approved nano-drug: lessons learned. J Control Release. 2012; 160: 117-134.

[3] Gabizon A, Barenholz Y, Bialer M. Prolongation of the circulation time of doxorubicin encapsulated in liposomes containing a polyethylene glycol-derivatized phospholipid: pharmacokinetics studies in rodents and dogs. Pharm Res. 1993; 10: 703-708.

[4] Gabizon A, Catane R, Uziely B, Kaufman B, Safra T, Cohen R, Martin F, Huang A, Barenholz Y. Prolonged circulation time and enhanced accumulation in malignant exudates of doxorubicin encapsulated in polyethylene-glycol coated liposomes. Cancer Res. 1994; 54:987-992.

[5] Mura S, Nicolas J, Couvreur P. Stimuli-responsive nanocarriers for drug delivery. Nat Mater. 2013; 12: 991-1003.

[6] Guo X, Shi C, Wang J, Di S, Zhou S. pH-triggered intracellular release from

actively targeting polymer micelles. Biomaterials. 2013; 34: 4544-4554.

[7] Dai L, Cao X, Liu K-F, Li C-X, Zhang G-F, Deng L-H, Si C-L, He J, Lei J-D. Self-assembled targeted folate-conjugated eight-arm-polyethlene glycol-betulinic acid nanoparticles for co-delivery of anticancer drugs. J Mater Chem B. 2015; 3: 3754-3766.

[8] Zhang L, Hou S, Zhang J, HuW, Wang C. Preparation, characterization, and in vivo evaluation of mitoxantrone-loaded, folate-conjugated albumin nanoparticles. Arch Pharm Res. 2010; 33: 1193–1198.

[9] Martínez A, Muñiz E, Teijón C, Iglesias I, Teijón J, Blanco M. Targeting tamoxifen to breast cancer xenograft tumours: preclinical efficacy of folate-attached nanoparticles based on alginate-cysteine/disulphide-bond-reduced albumin. Pharm Res. 2014; 31: 1264–74.

[10] Park J, JeonWI, Lee SY, Ock KS, Seo JH, Park J, Ganbold EO, Cho K, Song NW, Joo SW. Confocal Raman microspectroscopic study of folate receptor targeted delivery of 6-mercaptopurine embedded gold nanoparticles in a single cell. J Biomed Mat Res A. 2012; 100: 1221–1228.

[11] Ganeshkumar M, Ponrasu T, Raja MD, Subamekala MK, Suguna L. Green

synthesis of pullulan stabilized gold nanoparticles for cancer targeted drug delivery. Spectrochim Acta A Mol Biomol Spectrosc. 2014; 130: 64–71.

[12] Liong M, Lu J, Kovochich M, Xia T, Ruehm SG, Nel AE, Tamanoi F, Zink JI. Multifunctional inorganic nanoparticles for imaging, targeting, and drug delivery. ACS Nano. 2008; 2: 889–896.

[13] Fan J, Fang G, Wang X, Zeng F, Xiang Y, Wu S. Targeted anticancer prodrug with mesoporous silica nanoparticles as vehicles. Nanotechnology. 2011; 22: 455102.

[14] Shan D, Li J, Cai P, Prasad P, Liu F, Rauth AM, Wu XY. RGD-conjugated solid lipid nanoparticles inhibit adhesion and invasion of αvβ3 integrin-overexpressing breast cancer cells. Drug Deliv Transl Res. 2015; 5: 15-26.

[15] He X, Alves CS, Oliveira N, Rodrigues J, Zhu J, Bányai I, Tomás H, Shi X. RGD peptide-modified multifunctional dendrimer platform for drug encapsulation and targeted inhibition of cancer cells. Colloids Surf B Biointerfaces. 2015; 125: 82-89.

[16] Shargh VH, Hondermarck H, Liang M. Antibody-targeted biodegradable nanoparticles for cancer therapy. Nanomedicine (Lond). 2016; 11: 63-79.

[17] Ning ST, Lee SY, Wei MF, Peng CL, Lin SY, Tsai MH, Lee PC, Shih YH, Lin CY, Luo TY, Shieh MJ. Targeting colorectal cancer stem-like cells with anti-CD133 antibody-conjugated SN-38 nanoparticles. ACS Appl Mater Interfaces. 2016; 8: 17793-17804.

[18] Wu X, Chen J, Wu M, Zhao JX. Aptamers: active targeting ligands for cancer diagnosis and therapy. Theranostics. 2015; 5: 322-344.

[19] Liu J, Wei T, Zhao J, Huang Y, Deng H, Kumar A, Wang C, Liang Z, Ma X, Liang X-J. Multifuntional aptamer-based nanoparticles for targeted drug delivery to circumvent cancer resistance. Biomaterials. 2016; 91: 44-56.

[20] Yang Z, Luo H, Cao Z, Chen Y, Gao J, Li Y, Jiang Q, Xu R, Liu J. Dual-targeting hybrid nanoparticles for SN38 delivery to Her2 and CD44 overexpressed human gastric cancer. Nanoscale. 2016; 8:11543-11558.

[21] Srinivasarao M, Galliford CV, Low PS. Principles in the design of ligand-targeted cancer therapeutics and imaging agents. Nat Rev Drug Discov. 2015; 14: 203-219.

[22] Daniels TR, Bernabeu E, Rodriguez JA, Patel S, Kozman M, Chiappetta DA, Holler E, Ljubimova JY, Helguera G, Penichet ML. The transferrin receptor

and the targeted delivery of therapeutic agents against cancer. Biochimica et Biophysica Acta. 2012; 1820: 291-317.

[23] Yhee JY, Lee SJ, Lee S, Song S, Min HS, Kang S-W, Son S, Jeong SY, Kwon IC, Kim SH, Kim K. Tumor-targeting transferrin nanoparticles for systemic polymerized siRNA delivery in tumor-bearing mice. Bioconjugate Chem. 2013; 24: 1850-1860.

[24] Choi CHJ, Alabi CA, Webster P, Davis ME. Mechanism of active targeting in solid tumors with transferrin-containing gold nanoparticles. Proc Natl Acad Sci U S A. 2010; 107: 1235-1240.

[25] Yang X, Koh CG, Liu S, Pan X, Santhanam R, Yu B, Peng Y, Pang J, Golan S, Talmon Y, Jin Y, Muthusamy N, Byrd JC, Chan KK, Lee LJ, Marcucci G, Lee RJ. Transferrin receptor-targeted lipid nanoparticles for delivery of an antisense oligodeoxyribonucleotide against Bcl-2. Mol Pharm 2009; 6: 221-230.

[26] Whitney JF, Clark JM, Griffin TW, Gautam S, Leslie KO. Transferrin receptor expression in nonsmall cell lung cancer. Cancer. 1995; 76: 20-25.

[27] Kawamoto M, Horibe T, Kohno M, Kawakami K. A novel transferrin

receptor-targeted hybrid peptide disintegrates cancer cell membrane to induce rapid killing of cancer. BMC Cancer. 2011; 11: 359.

[28] Gao J, Liu W, Xia Y, Li W, Sun J, Chen H, Li B, Zhang D, Qian W, Meng Y, Deng L, Wang H, Chen J, Guo Y. The promotion of siRNA delivery to breast cancer overexpressing epidermal growth factor receptor through anti-EGFR antibody conjugation by immunoliposomes. Biomaterials. 2011; 32: 3459-3470.

[29] Kim Y-H, Jeon J, Hong SH, Rhim W-K, Lee Y-S, Youn H, Chung J-K, Lee MC, Lee DS, Kang KW, Nam J-M. Tumor targeting and imaging using cyclic RGD-PEGylated gold nanoparticle probes with directly conjugated Iodine-125. Small. 2011; 7: 2052-2060.

[30] El-Sayed IH, Huang X, El-Sayed MA. Selective laser photo-thermal therapy of epithelial carcinoma using anti-EGFR antibody conjugated gold nanoparticles. Cancer Letter. 2006; 239: 129-135.

[31] Yokoyama T, Tam J, Kuroda S, Scott AW, Aron J, Larson T, Shanker M, Correa AM, Kondo S, Roth JA, Sokolov K, Ramesh R. EGFR-targeted hybrid plasmonic magnetic nanoparticles synergistically induce autophagy

and apoptosis in non-small cell lung cancer cells. PLoS one. 2011; 6: e25507.

[32] Liu P, Li Z, Zhu M, Sun Y, Li Y, Wang H, Duan Y. Preparation of EGFR monoclonal antibody conjugated nanoparticles and targeting to hepatocellular carcinoma. J Mater Sci: Mater Med. 2010; 21: 551-556.

[33] Iqbal N, Iqbal N. Human epidermal growth factor receptor 2 (HER2) in cancers: overexpression and therapeutic implications. Mol Biol Int. 2014; 2014: 852748.

[34] Wartlick H, Michaelis K, Balthasar S, Strebhardt K, Kreuter J, Langer K. Highly specific HER2-mediated cellular uptake of antibody-modified nanoparticles in tumor cells. J Drug Target. 2004; 12: 461-471.

[35] Cirstoiu-Hapca A, Bossy-Nobs L, Buchegger F, Gurny R, Delie F. Differential tumor cell targeting of anti-HER2 (Herceptin®) and anti-CD20 (Mabthera®) coupled nanoparticles. Int J Pharm. 2007; 331: 190-196.

[36] Anhorn MG, Wagner S, Kreuter J, Langer K, von Briesen H. Specific targeting of HER2 overexpressing breast cancer cells with doxorubicin-loaded trastuzumab-modified human serum albumin nanoparticles. Bioconjug Chem. 2008; 19: 2321-2331.

[37] Vogetseder A, Thies S, Ingold B, Roth P, Weller M, Schrami P, Goodman SL, Moch H. v-Integrin isoform expression in primary human tumors and brain metastases. Int J Cancer. 2013; 133: 2362-2371.

[38] Danhier F, Breton AL, Préat V. RGD-based strategies to target alpha(v) beta(3) integrin in cancer therapy and diagnosis. Mol Pharm. 2012; 9: 29612973.

[39] Kim Y-H, Jeon J, Hong SH, Rhim W-K, Lee Y-S, Youn H, Chung J-K, Lee MC, Lee DS, Kang KW, Nam J-M. Tumor targeting and imaging using cyclic RGD-PEGylated gold nanoparticles probes with directly conjugated Iodine-125. Small. 2011; 7: 2052-2060.

[40] Capolla S, Garrovo C, Zorzet S, Lorenzon A, Rampazzo E, Spertz R, Pozzato G, Núñez L, Tripodo C, Macor P, Biffi S. Targeted tumor imaging of anti-CD20-polymeric nanoparticles developed for the diagnosis of B-cell malignancies. Int J Nanomedicine. 2015; 10: 4099-4109.

[41] Voltan R, Secchiero P, Ruozi B, Formi F, Agostinis C, Caruso L, Vandelli MA, Zauli G. Nanoparticles engineered with rituximab and loaded with Nutlin-3 show promising therapeutic activity in B-leukemic xenografts. Clin

Cancer Res. 2013; 19: 3871-3880.

[42] Louderbough JM, Schroeder JA. Understanding the dual nature of CD44 in breast cancer progression. Mol Cancer Res. 2011; 9: 1573-1586.

[43] Wang L, Su W, Liu Z, Zhou M, Chen S, Chen Y, Lu D, Liu Y, Fan Y, Zheng Y, Han Z, Kong D, Wu JC, Xiang R, Li Z. CD44 antibody-targeted liposomal nanoparticles for molecular imaging and therapy of hepatocellular carcinoma. Biomaterials. 2012; 33: 5107-5114.

[44] Miao W, Shim G, Kang CM, Lee S, Choe YS, Choi H-G, Oh Y-K. Cholesteryl hyaluronic acid-coated, reduced graphene oxide nanosheets for anti-cancer drug delivery. Biomaterials. 2013; 34: 9638-9647.

[45] Gärtner S, Gunesch A, Knyazeva T, Wolf P, Högel B, Eiermann W, Ullrich A, Knyazev P, Ataseven B. PTK 7 is a transforming gene and prognostic marker for breast cancer and nodal metastasis involvement. PLoS One. 2014; 9: e84472.

[46] Huang F, You M, Chen T, Zhu G, Liang H, Tan W. Self-assembled hybrid nanoparticles for targeted co-delivery of two drugs into cancer cells. Chem Commun (Camb). 2014; 50: 3103-3105.

[47] Zhang Z, Ali MM, Eckert MA, Kang DK, Chen YY, Sender LS, Fruman DA, Zhao W. A polyvalent aptamer system for targeted drug delivery. Biomaterials. 2013; 34: 9728-9735.

[48] Haffner MC, Kronberger IE, Ross JS, Sheehan CE, Zitt M, Mühlmann G, Ofner D, Zelger B, Ensinger C, Yang XJ, Geley S, Margreiter R, Bander NH. Prostate-specific membrane antigen expression in the neovasculature of gastric and colorectal cancers. Hum Pathol. 2009; 40: 1754-1761.

[49] Haffner MC, Laimer J, Chaux A, Schäfer G, Obrist P, Brunner A, Kronberger IE, Laimer K, Gurel B, Koller JB, Seifarth C, Zelger B, Klocker H, Rasse M, Doppler W, Bander NH. High expression of prostate-specific membrane antigen in the tumor-associated neo-vasculature is associated with worse prognosis in squamous cell carcinoma of the oral cavity. Mod Pathol. 2012; 25: 1079-1085.

[50] Fung EK, Cheal SM, Fareedy SB, Punzalan B, Beylergil V, Amir J, Chalasani S, Weber WA, Spratt DE, Veach DR, Bander NH, Larson SM, Zanzonico PB, Osborne JR. Targeting of radiolabeled J591 antibody to PSMA-expressing tumors: optimization of imaging and therapy based on

non-linear compartmental modeling. EJNMMI Res. 2016; 6: 7.

[51] Choi J, Park Y, Choi EB, Kim HO, Kim DJ, Hong Y, Ryu SH, Lee JH, Suh JS, Yang J, Huh YM, Haam S. Aptamer-conjugated gold nanorod for photothermal ablation of epidermal growth factor receptor-overexpressed epithelial cancer. J Biomed Opt. 2014; 19: 051203.

[52] Zelasko-Leon DC, Fuentes CM, Messersmith PB. MUC1-targeted cancer cell photothermal ablation using bioinspired gold nanorods. PLoS One. 2015; 10: e0128756.

[53] Miao W, Shim G, Lee S, Oh Y-K. Structure-dependent photothermal anticancer effects of carbon-based photoresponsive nanomaterials. Biomaterials. 2014; 35: 4058-4065.

[54] Kim SH, Lee JE, Sharker SM, Jeong JH, In I, Park SY. In vitro and in vivo tumor targeted photothermal cancer therapy using funcionalized graphene nanoparticles. Biomacromolecules. 2015; 16: 3519-3529.

[55] Hashida Y, Tanaka H, Zhou S, Kawakami S, Yamashita F, Murakami T, Umeyama T, Imahori H, Hashida M. Photothermal ablation of tumor cells using a single-walled carbon nanotube-peptide composite. J Control Release.

2014; 173: 59-66.

[56] Chen M, Fang X, Tang S, Zheng N. Polypyrrole nanoparticles for high-performance in vivo near-infrared photothermal cancer therapy. Chem Commun. 2012; 48: 8934-8936.

[57] Zha Z, Yue X, Ren Q, Dai Z. Uniform polypyrrole nanoparticles with high photothermal conversion efficiency for photothermal ablation of cancer cells. Adv Mater. 2013; 25: 777-782.

[58] Zhou J, Lu Z, Zhu X, Wang X, Liao Y, Ma Z, Li F. NIR photothermal therapy using polyaniline nanoparticles. Biomaterials. 2013; 34: 9584-9592.

[59] Yuan A, Wu J, Tang X, Zhao L, Xu F, Hu Y. Application of near-infrared dyes for tumor imaging, photothermal, and photodynamic therapies. J Pharmceut Sci. 2013; 102: 6-28.

[60] Cheng L, He W, Gong H, Wang C, Chen Q, Cheng Z, Liu Z. PEGylated micelle nanoparticles encapsulating a non-fluorescent near-infrared organic dye as a safe and highly-effective photothermal agent for in vivo cancer therapy. Adv Funct Mater. 2013; 23: 5893-5902.

[61] Zou L, Wang H, He B, Zeng L, Tan T, Cao H, He X, Zhang Z, Guo S, Li Y. Current approaches of photothermal therapy in treating cancer metastasis with nanotherapeutics. Theranostics. 2016; 6: 762-772.

Chapter II

Polyaptamer DNA nanothread-anchored, reduced graphene oxide nanosheets for targeted delivery

1. Introduction

DNA aptamers have emerged as a potential targeting moiety for drug-delivery systems. DNA aptamers have been chemically conjugated [1] or physically complexed [2] to anti-cancer drugs. Carbon nanotubes have been physically adsorbed with DNA aptamers for anticancer drug delivery [3]. Notably, surface modification of nanoparticles with DNA aptamers has been reported to improve tumor accumulation [4,5]. Despite the ability of DNA aptamers to recognize specific cellular targets, the wide application of these targeting moieties to drug delivery has been hampered in part because their binding affinity is generally lower than that of antibodies [6].

Rolling circle amplification (RCA) is a recently developed molecular technique for amplifying single-stranded DNA (ssDNA) from a circular oligonucleotide, which acts as a template [7]. The amplified ssDNA contains repeating units of sequences complementary to the circular template. RCA has been applied to produce multivalent DNA aptamers for detection of small molecules [8] and target proteins [9,10]. Moreover, RCA-derived multivalent aptamers have been used to capture specific types of cells, showing improved binding affinities

compared with monovalent DNA aptamers and antibodies in microfluidic devices [11].

Reduced graphene oxide (rGO) nanosheets have been studied as promising materials for anticancer drug delivery [12]. However, rGO nanosheets alone lack tumor-targeting ability. Conferring tumor-targeting ability to rGO nanosheets has been accomplished through modification with various molecules. Recently, modification with cholesteryl hyaluronic acid has been reported to enhance the tumor distribution of rGO nanosheets [13]. However, using aptamers with high affinity and specificity represents an important strategy for enhancing the targeted delivery of rGO to tumor cells.

In this study, it was hypothesized that coating rGO nanosheets with tumor-specific polyaptamer nanothreads would improve the tumor distribution and in vivo antitumor efficacy of anticancer drugs. To test this hypothesis, tumor cell-specific polyaptamer nanothreads were prepared by RCA. Moreover, to enhance the anchoring capability of polyaptamers onto rGO, an oligonucleotide bridge sequence was introduced between repeating aptamer sequences. As a polyaptamer target, protein tyrosine kinase 7 (PTK7), a biomarker for leukemia cells [14,15]. Here, PTK7 polyaptamer nanothread-anchored rGO nanosheets

were tested whether they could enhance the delivery of the anticancer drug, doxorubicin (Dox), to PTK7-overexpressing tumor tissues.

2. Materials and methods

2.1. Synthesis of polyaptamer nanothreads using RCA

PTK7 polyaptamer nanothreads without a bridge sequence (PN) or with a 22-mer T oligonucleotide (oligoT) bridge sequence (PNT) were synthesized using RCA reaction. Linear ssDNA templates of PN and PNT were hybridized to an RCA primer (Bioneer Corporation, Daejeon, Republic of Korea) designed to bind to 3’ and 5’ ends of the template. The sequence of the RCA primer for PN and PNT was 5'-CTG CGC CGC CGG GAA AAT ACT G-3'. The sequences of linear ssDNA templates were 5'-phosphate-CGG CGG CGC AGC AGT TAG ATT CTA ACC GTA CAG TAT TTT CC-3' for PN, and 5'-phosphate-CGG CGG CGC AGC AGT TAG ATA AAA AAA AAA AAA AAA AAA AAA TCT AAC CGT ACA GTA TTT TCC-3' for PNT. For some experiments, scrambled-sequence nanothreads containing an oligoT bridge sequence (SNT) were synthesized using an RCA reaction. The sequence of the RCA primer for SNT was 5'-ACT AGT CAG ATA TTA CTA TGA C-3', and the sequence of the linear ssDNA template for SNT was 5'-phosphate-ATC TGA CTA GTA TAT ACG GCA AAA AAA AAA AAA AAA AAA AAA GGT GCG CTC GGT CAT AGT AAT-3'. RCA templates for PN, PNT, and SNT are depicted in Fig.

1A. The RCA reaction was performed as described previously [16] with slight modifications. Briefly, 0.5 μM linear ssDNA template bearing a 5'-phosphate and 3'-hydroxyl group, and an RCA primer were first annealed in hybridization buffer (10 mM Tris-HCl pH 8.0, 1 mM EDTA, 100 mM NaCl) by heating to 95℃ for 5 min and gradually cooling to room temperature over 3 h. The complementary binding of an RCA primer to both ends of linear ssDNA allowed the formation of a circular ssDNA with a nick between 3' and 5' ends. The nick in the circular DNA was closed by adding 125 units/ml T4 DNA ligase (Thermo Scientific, Waltham, MA, USA) to 1 ml of reaction mixture and incubating at 4℃ for 12 h. π29 DNA polymerase (100 units/ml; Thermo Scientific), RCA reaction buffer, and 2 mM dNTP (Intron Biotechnology, Seoul, Republic of Korea) were then added to the ligation mixture and incubated at 30℃ for 5 min. Thereafter, π29 DNA polymerase was inactivated by heating at 70℃ for 10 min, and the remaining dNTP was removed by size-exclusion chromatography using a PD-10 desalting column (GE Healthcare, Buckinghamshire, UK). The resulting RCA products were stored at 4℃ until use.

2.2. Preparation of rGO nanosheets

Graphene oxide (GO) nanosheets were prepared from graphite by Hummer's method. In brief, 0.5 g graphite powder (Sigma-Aldrich, St. Louis, MO, USA), 3 g $KMnO_4$ (Sigma-Aldrich), and 0.5 g $NaNO_3$ (Sigma-Aldrich) were added to 23 ml cold H_2SO_4. After stirring for 1 h at 35℃, 46 ml water was added and the mixture was incubated at 90℃ for 1 h. The reaction was stopped by adding 140 ml of water and 10 ml of 30 % H_2O_2. The product was purified by washing four times with centrifugation at 1600 × g, first with 5 % HCl and then three times with triple-distilled water (TDW). The product was dispersed in TDW and sonicated for 2 h to exfoliate GO layers to GO nanosheets. Unexfoliated GO layers were removed by centrifugation at 1600 × g for 10 min. The supernatant was filtered through 0.2-μm polycarbonate membrane filters (Millipore Corp., Billerica, MA, USA) using an extruder (Northern Lipid, British Columbia, Canada).

rGO nanosheets were synthesized by reduction of GO nanosheets as previously described [13]. Briefly, 2 ml of GO nanosheets in water was mixed with 8 ml of water, 0.5 ml of ammonia solution (28 wt% in water; Junsei Chemical, Tokyo, Japan), and 5 μl of hydrazine monohydrate (64 % in water; Sigma-Aldrich). The

mixture was stirred in a water bath at 80℃ for 10 min. After cooling to room temperature, the remaining hydrazine and ammonia were eliminated by dialysis (MWCO 100K; Spectrum Laboratories Inc., Rancho Dominguez, CA, USA) against TDW.

2.3. Anchoring nanothreads onto rGO nanosheets

PN-anchored rGO nanosheets (PNrGO), PNT-anchored rGO nanosheets (PNTrGO), and SNT-anchored rGO nanosheets (SNTrGO) were prepared by mixing nanothreads with the corresponding rGO nanosheets at a weight ratio of 0.5:1 (nanothread:nanosheet) and incubating at room temperature for 10 min. Anchoring efficiency of nanothreads was evaluated using a gel-retardation assay. Briefly, nanothreads and rGO nanosheet reaction mixtures were loaded onto a 0.8 % agarose gel containing 0.5 μg/mL ethidium bromide and electrophoresed for 30 min at 50 mV in Tris-borate-ethylenediamine-tetraacetic acid buffer. For comparison, free PN or PNT was loaded onto the gel. The migration of rGO-unbound nanothreads was visualized using a Gel Doc System (Bio-Rad Lab., Hercules, CA, USA).

2.4. Characterization of nanothread-anchored rGO nanosheets

Nanothread-anchored rGO nanosheets were characterized by assessing morphology, size, zeta potential, and stability in aqueous solution. The morphology of PNT and PNTrGO was examined by transmission electron microscopy (TEM) using a JEM1010 transmission electron microscope (JEOL, Tokyo, Japan). The sizes of rGO nanosheets with or without nanothreads were measured using dynamic light scattering. The zeta potential values of rGO nanosheets with or without nanothreads were measured by laser Doppler microelectrophoresis at an angle of 22° using an ELS-8000 instrument (Photal, Osaka, Japan). The stability of rGO and PNTrGO was investigated by allowing a suspension of rGO or PNTrGO in phosphate-buffered saline (PBS; 50 mM, pH 7.4) to stand at room temperature, with periodic monitoring samples for the appearance of precipitates.

2.5. Loading of Dox onto rGO nanosheets

Dox was loaded onto rGO, SNTrGO, and PNTrGO by physical adsorption. Dox-loaded rGO (Dox/rGO), Dox-loaded SNTrGO (Dox/SNTrGO), and Dox-loaded

PNTrGO (Dox/PNTrGO) were generated by adding Dox to the corresponding rGO nanosheets at a weight ratio of 1:5 (Dox:rGO nanosheets) and incubating at room temperature for 10 min. Free Dox was then removed using a PD-10 desalting column (GE Healthcare). The extent of Dox loading onto various rGO nanosheets was determined by measuring the loss of Dox fluorescence at 485 nm caused by the quenching of rGO-adsorbed Dox using a fluorescence microplate reader (Gemini XS; Molecular Devices, Sunnyvale, CA, USA).

2.6. Preparation of fluorescent-marker–labeled rGO nanosheets

For cellular uptake studies and molecular imaging, PNTrGO and SNTrGO were labeled with cyanine 5.5 dye (Cy5.5) conjugated to the lipid, 1,2-distearoyl-*sn*-glycero-3-phosphoethanolamine-N-[amino(polyethylene glycol)-5000] (DSPE-PEG_{5000}-NH_2), containing PEG with a molecular weight of 5,000 (NOF Corporation, Tokyo, Japan). First, 4.5 mg of 1,2-DSPE-PEG_{5000}-NH_2 was dissolved in 2 ml of 0.1 M sodium bicarbonate buffer (pH 8.3), after which 1.0 mg of Cy5.5 NHS ester (Lumiprobe, Hallandale Beach, FL, USA) in 100 μl dimethyl sulfoxide was added with stirring for 4 h in the dark. The resulting 1,2-

distearoyl-*sn*-glycero-3-phosphoethanolamine-N-[poly(ethylene glycol)$_{5000}$-N`]-cyanine 5.5 (DSPE-PEG$_{5000}$-Cy5.5) was purified using a self-packed Sephadex G15 column (GE Healthcare) and stored at 4℃ until use. For labeling of various rGO nanosheets with DSPE-PEG$_{5000}$-Cy5.5, 100 μl of the corresponding rGO nanosheet solution (1 mg/ml) was mixed with 10 μl DSPE-PEG$_{5000}$-Cy5.5 (10 mg/ml). After sonication for 30 min, unbound DSPE-PEG$_{5000}$-Cy5.5 was removed by dialyzing the mixture (MWCO 1000K; Spectrum Laboratories, Inc.) against TDW for 24 h.

2.7. Cell culture

Human T-cell acute lymphoblastic leukemia (CCRF-CEM) cells and human Burkitt's lymphoma (Ramos) cells (Korean Cell Line Bank, Seoul, Republic of Korea) were cultured in RPMI-1640 medium (Welgene, Daegu, Republic of Korea) supplemented with 10 % fetal bovine serum and 100 units/ml penicillin plus 100 μg/ml streptomycin. The cells were grown at 37°C in a humidified 5 % CO_2 atmosphere.

2.8. PTK7 expression study

The expression of PTK7 on the surfaces of CCRF-CEM and Ramos cells was evaluated using flow cytometry. After harvesting, cells were incubated for 30 min at 4℃ in cold PBS containing 3 % bovine serum albumin. Next, cells were washed and incubated for 30 min at 4℃ with a monoclonal R-phycoerythrin (PE)-conjugated anti-PTK7 antibody (Miltenyi Biotec, Bergisch Gladbach, Germany) diluted 1:10 in cold PBS containing 2 % fetal bovine serum. Cells expressing PTK7 on the surface were identified by detection of fluorescent monoclonal antibodies.

2.9. Cellular uptake study

Cellular uptake of various rGO nanosheets was evaluated using confocal microscopy and flow cytometry. CCRF-CEM or Ramos cells were seeded onto 48-well plates at a density of 8×10^4 cells/well. After overnight incubation, cells were treated with DSPE-PEG_{5000}-Cy5.5–labeled rGO, SNTrGO or PNTrGO for 15 min, washed three times with PBS containing 2 % fetal bovine serum, and evaluated by confocal microscopy or flow cytometry. For flow cytometry, the

cells were analyzed using a BD FACSCalibur system equipped with Cell Quest Pro software (BD Biosciences, San Jose, CA, USA). For confocal microscopy, the cells were transferred onto poly-L-lysine coated plates (BD Biosciences) and incubated for 1 h to allow cells to attach. Cells were then fixed with 4% paraformaldehyde in PBS for 15 min and stained with 4',6-diamidino-2-phenylindole dihydrochloride (DAPI). Cy5.5 fluorescence was observed using a confocal laser-scanning microscope (LSM 5 Exciter; Carl Zeiss, Inc., Jena, Germany).

2.10. In vitro anticancer activity assay

In vitro anticancer effects of Dox/rGO, Dox/SNTrGO, and Dox/PNTrGO were assessed against CCRF-CEM and Ramos cells. CCRF-CEM and Ramos cells were seeded into 48-well plates at a density of 4×10^4 cells/well. After overnight incubation, the cells were treated for 1 h with Dox/rGO, Dox/SNTrGO, or Dox/PNTrGO (2 μM Dox). The culture medium was then replaced, cells were incubated for an additional 24 h, and viability was measured using a Cell Counting Kit 8 (CCK-8; Dojindo Laboratories, Kumamoto, Japan) or live-cell

staining assay (Molecular Probes, Eugene, OR, USA). For CCK-8 assays, 20 μl of CCK-8 solution was added to each well. After incubating for 30 min, the absorbance of the medium was measured colorimetrically at 450 nm using an enzyme-linked immunosorbent assay reader (Sunrise-Basic; TECAN, Mannedorf, Switzerland). For live-cell staining assays, live cells were stained with calcein-AM after a 1 h treatment with Dox/rGO, Dox/SNTrGO, or Dox/PNTrGO.

2.11. In vivo molecular imaging

The biodistribution of DSPE-PEG_{5000}-Cy5.5-labeled SNTrGO and PNTrGO in mice was observed by molecular imaging. CCRF-CEM cells (5×10^6) in a PBS solution containing 50 % matrigel (BD Biosciences) were subcutaneously inoculated into the dorsal right flank of 5-wk-old athymic nude mice (Orient Bio Inc., Seongnam, Republic of Korea). After tumors had become established, DSPE-PEG_{5000}-Cy5.5-labeled, nanothread-anchored rGO nanosheets were intravenously administered into mice at a dose of 1 mg/kg. At various time points after intravenous injection, Cy5.5 signals of mice were scanned using an eXplore Opitx system (Advance Research Technologies Inc., Montreal, Canada) with a

laser power of 25 mW and a count time of 0.3 s/point. A 670-nm pulsed-laser diode was used to excite Cy5.5. Long-wave fluorescence emission was detected with a fast photomultiplier tube (Hamamatsu Photonics, Hamamatsu, Japan) and a time-correlated single-photon counting system (Becker and Hickl GmbH, Berlin, Germany).

2.12. In vivo anti-tumor activity assay

The anti-tumor effects of Dox administered on various rGO nanosheets were tested using CCRF-CEM tumor-bearing mice. Five week-old athymic nude mice were subcutaneously injected in the dorsal right flank with 5×10^6 CCRF-CEM cells in 50 % matrigel/PBS. When the tumors had grown to 150–180 mm^3, the mice were intravenously administered 3 mg/kg of Dox (15 mg/kg) as Dox/rGO, Dox/SNTrGO, or Dox/PNTrGO every other day for a total of three injections. Tumor size was measured in two dimensions using a slide caliper every other day, and tumor volume was calculated as $a \times b \times b \times 0.5$, where a is the largest and b is the smallest dimension. For histopathological analyses, tumor tissues were excised and weighed on day 12. The sections were stained with anti-proliferating

cell nuclear antigen (PCNA) antibody [17], and assayed using terminal deoxynucleotidyl transferase dUTP nick-end labeling (TUNEL) [17].

2.13. Statistics

All data were statistically analyzed using ANOVA with post hoc Student–Newman–Keuls test. SigmaStat software (version 3.5; Systat Software, Richmond, CA, USA) was used for analyses, and a p-value less than 0.05 was considered statistically significant.

3. Results

3.1. Effects of the oligoT bridge on nanothread anchoring to rGO

The effects of the oligoT bridge sequences on nanothread anchoring were tested by first producing PN, and PNT by the RCA reaction, as depicted in Fig. II-1A. Unlike the case for PN, a 22-mer A oligonucleotide sequence was included within the linear ssDNA template of PNT to produce oligoT in the RCA product. PN or PNT was mixed with rGO at a weight ratio of 0.5:1 to produce PNrGO or PNTrGO (Fig. II-1B). Gel retardation assays showed the presence of migrating unbound DNA nanothreads in PNrGO complexes but not in PNTrGO complexes (Fig. II-1C). These results indicate that the oligoT bridge sequences improved the ability of RCA nanothreads to anchor onto rGO nanosheets.

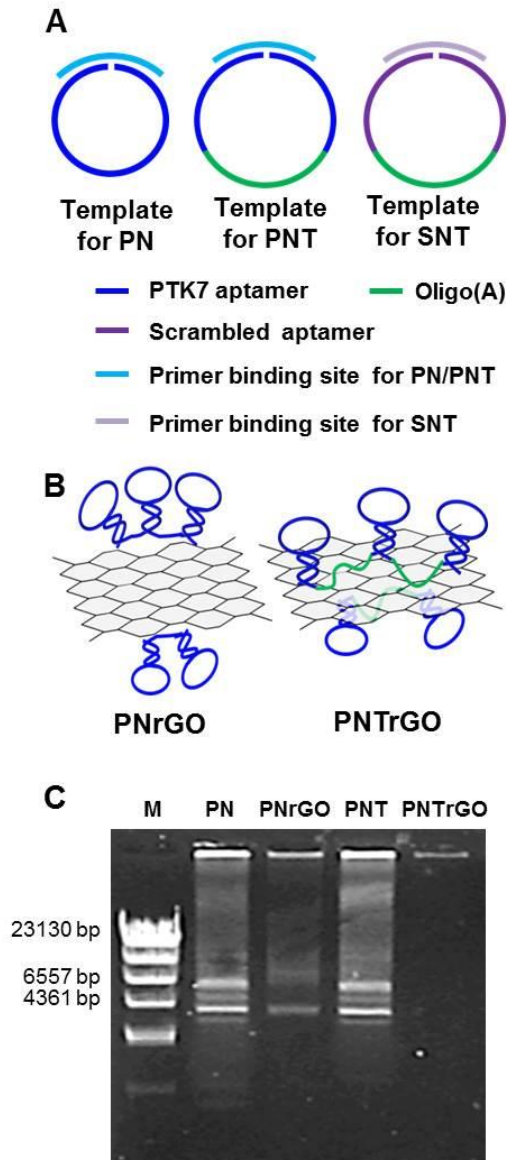

Fig. II-1. Schematic illustration of PNrGO and PNTrGO nanosheets.

(A) Templates of PN, PNT, and SNT for RCA. (B) Schematic representation of PNrGO and PNTrGO. (C) Complexation of rGO nanosheets with PN or PNT was analyzed by electrophoresis on 0.8 % (w/v) agarose gels.

3.2. Physicochemical properties of PNTrGO

The morphology, size, zeta potential, and stability of PNTrGO in buffer were characterized. Transmission electron microscopy (TEM) showed that PNT alone exhibited a nanothread-like morphology (Fig. II-2A). TEM of PNTrGO revealed the presence of PNT anchored on rGO nanosheets (Fig. II-2B). Anchoring of PNT onto rGO nanosheets did not significantly affect the mean size of rGO nanosheets (Fig. II-2C), but decreased zeta potential values (Fig. II-2D). Moreover, PNT coating enhanced the dispersion stability of rGO nanosheets in PBS (Fig. II-2E). Plain rGO nanosheets formed precipitates in PBS within 1 day. In contrast, PNTrGO remained stable in PBS for at least 7 days at room temperature.

3.3. Enhanced cellular uptake of PNTrGO nanosheets in PTK7-positive cells

The cellular uptake of PNTrGO was enhanced in PTK7-positive cells, but not in the PTK7-negative cells. The dependence of PNTrGO uptake on PTK7 expression was tested by flow cytometry and fluorescence microscopy. Flow

cytometry showed that PTK7 was not expressed on the surface of Ramos cells (Fig. II-3A), but was highly expressed on CCRF-CEM cells (Fig. II-3B), consistent with a previous report [18]. In PTK7-negative Ramos cells, the uptake of DSPE-PEG_{5000}-Cy5.5-labeled PNTrGO was not significantly different from that of DSPE-PEG_{5000}-Cy5.5-labeled SNTrGO, as determined by fluorescence microscopy (Fig. II-3C). In contrast, PTK7-positive CCRF-CEM cells showed greater uptake of fluorescent dye-labeled PNTrGO than fluorescent dye-labeled SNTrGO (Fig. II-3D). Consistent with these fluorescence microscopy data (Fig. II-3C, II-3D), flow cytometry revealed that notable cellular uptake of PNTrGO occurred in CCRF-CEM cells (Fig. II-3F), but not in Ramos cells (Fig. II-3E).

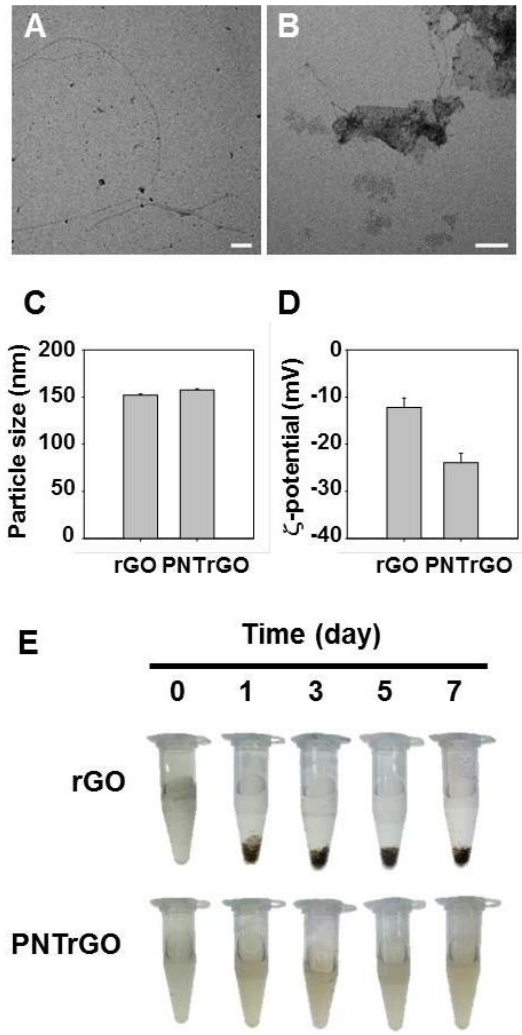

Fig. II-2. Characterization of nanothread-anchored rGO nanosheets.

The morphology of PNT (A) (scale bar, 200 nm) and PNTrGO nanosheets (B) (scale bar, 100 nm) was observed by TEM. (C) The sizes of rGO and PNTrGO were measured by dynamic light scattering. (D) Zeta potential values of rGO and PNTrGO were determined by laser Doppler microelectrophoresis at an angle of 22° using an ELS-8000 instrument. (E) The stability of rGO and PNTrGO was evaluated in PBS.

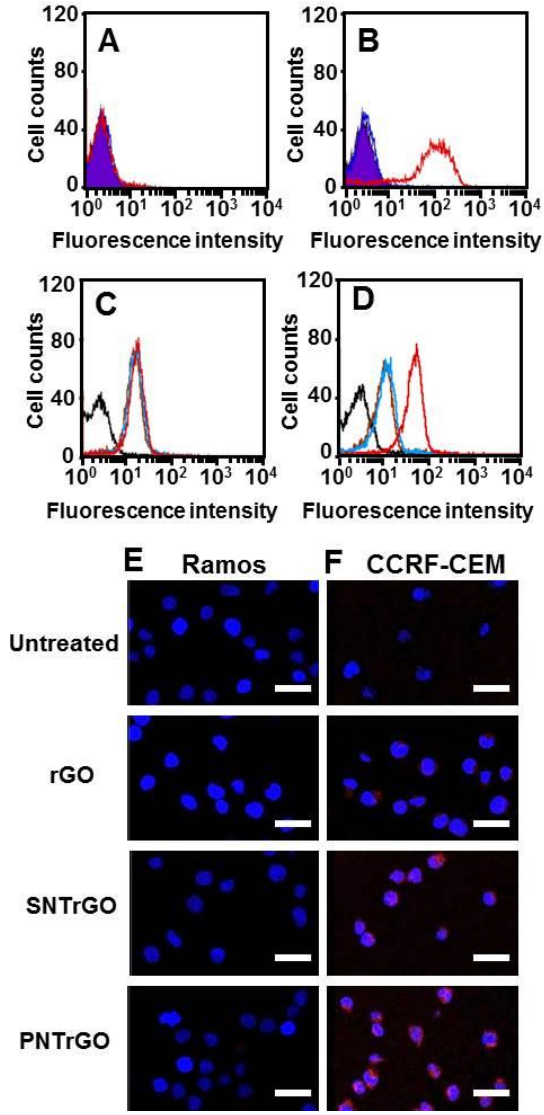

Fig. II-3. Cellular uptake of various rGO nanosheets in PTK7-positive and -negative cells.

Ramos cells (A) and CCRF-CEM cells (B) were stained with fluorescent a nti-PTK7 antibody, and fluorescence-positive cells were measured by flow

- continued next page -

cytometry. (C, E) Ramos cells were left untreated or were treated with rGO, SNTrGO, or PNTrGO. (D,F) CCRF-CEM cells were left untreated or were treated with rGO, SNTrGO, or PNTrGO. For detection of cellular uptake, rGO nanosheets were labeled with DSPE-PEG_{5000}-Cy5.5. After incubation for 15 min, cellular fluorescence was observed by flow cytometry (C,D), and confocal microscopy (E,F).

3.4. In vitro anticancer effects of Dox/PNTrGO nanosheets

Consistent with cellular uptake patterns, Dox/PNTrGO exhibited enhanced anticancer activity in PTK7-positive CCRF-CEM cells, but not in PTK7-negative Ramos cells (Fig. II-4A). In Ramos cells, the anticancer activity of Dox did not differ with respect to modification of rGO with PNT or SNT. In contrast, the anticancer activity of Dox toward CCRF-CEM cells was significantly higher following delivery with PNTrGO compared to delivery with rGO or SNTrGO (Fig. II-4B). Treatment of CCRF-CEM cells with Dox on PNTrGO reduced the viability of the cells to 43.1 % ± 9.2 % of that in control cells. Fluorescent dye-based live-cell staining assays revealed that the killing effect of Dox was greater when delivered by PNTrGO in CCRF-CEM cells (Fig. III-4D), but not in Ramos cells (Fig. II-4C).

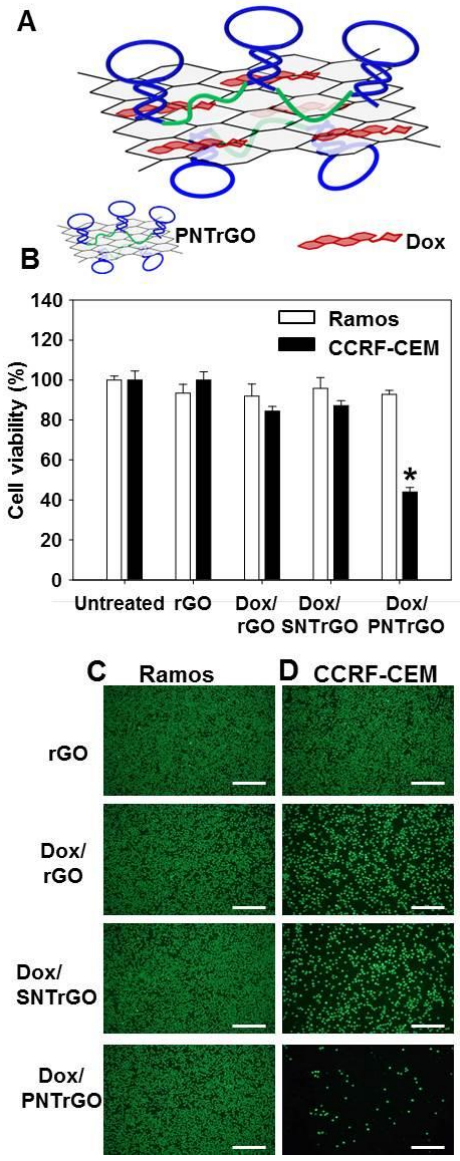

Fig. II-4. In vitro anticancer effects of Dox delivered using nanothread -anchored rGO nanosheets.

(A) A schematic depiction of Dox/PNTrGO is shown. (B) CCRF-CEM or

- continued next page -

Ramos cells were treated with rGO, Dox/SNTrGO, or Dox/PNTrGO for 1 h. Untreated cells were used as a control. After incubation for an addition al 24 h, the viability of cells was measured by CCK-8 assay. The results are the means ± SE of three independent experiments (*$p < 0.05$ compared to other groups; ANOVA and Student-Newman-Keuls test). Live Ramos ce lls (C) and CCRF-CEM cells (D) were stained with calcein-AM and obser ved by fluorescence microscopy. Scale bar, 250 μm.

3.5. Tumor tissue accumulation of nanothread-anchored rGO nanosheets

Following intravenous administration into CCRF-CEM tumor-bearing mice, fluorescent dye-labeled PNTrGO exhibited preferential tumor tissue accumulation. Compared with mice in fluorescent rGO and SNTrGO treatment groups, PNTrGO-treated mice showed tumor localization of fluorescence signal at 1 h (Fig. II-5A), 24 h (Fig. II-5B), and 48 h (Fig. II-5C). At 48 h, fluorescence intensity (photon count values) in tumor tissues was 2.3- and 2.5-fold higher in the PNTrGO-treated group than in groups treated with SNTrGO or rGO, respectively (Fig. II-5D).

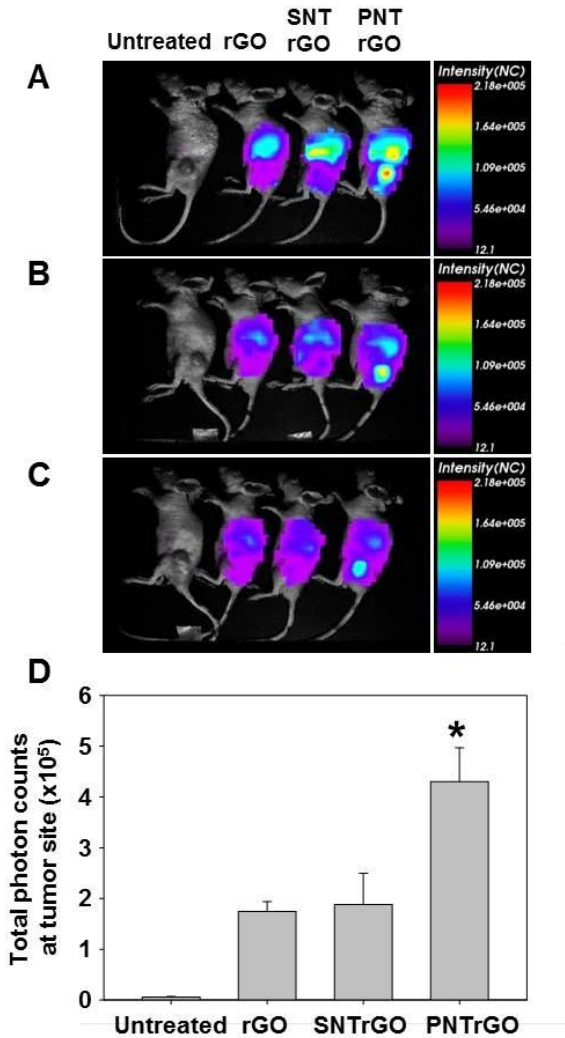

Fig. II-5. Biodistribution of nanothread-anchored rGO nanosheets.

CCRF-CEM tumor-bearing mice were intravenously injected with rGO, SN TrGO, or PNTrGO. DSPE-PEG_{5000}-Cy5.5 was used to label various rGO n anosheets for imaging. After 1 h (A), 24 h (B) and 48 h (C), the in vivo distribution of rGO nanosheets was visualized using a molecular imaging

- continued next page -

system. (D) Total photon counts in tumor sites relative to that in the untre ated group were quantified 48 h post-dose using an in vivo imaging syste m (*p < 0.05 compared to other groups; ANOVA and Student-Newman-K euls test).

3.6. In vivo anticancer effects of Dox delivered by various nanothread-anchored rGO nanosheets

Delivery of Dox by intravenous administration of Dox/PNTrGO produced the greatest antitumor effects against CCRF-CEM tumors in mice. On day 12, tumor volumes in mice treated with Dox/PNTrGO were significantly lower than those in mice treated with Dox/SNTrGO or Dox/rGO. In Dox/PNTrGO-treated mice, tumor volume was reduced to about 23 % of that in untreated mice (Fig. II-6A), and tumor weight was reduced to about 12 % (Fig. II-6B). In keeping with these tumor-growth–inhibitory effects (Fig. II-6A), PCNA staining showed that the proliferating cell population was lowest in tumor tissues of mice treated with Dox/PNTrGO (Fig. II-7A, II-7C). Moreover, TUNEL assays revealed that the apoptotic cell population in tumor tissues of mice treated with Dox/PNTrGO was 2.1- and 2.5-fold larger than that in Dox/SNTrGO-treated and Dox/rGO-treated groups, respectively (Fig. II-7B, II-7D).

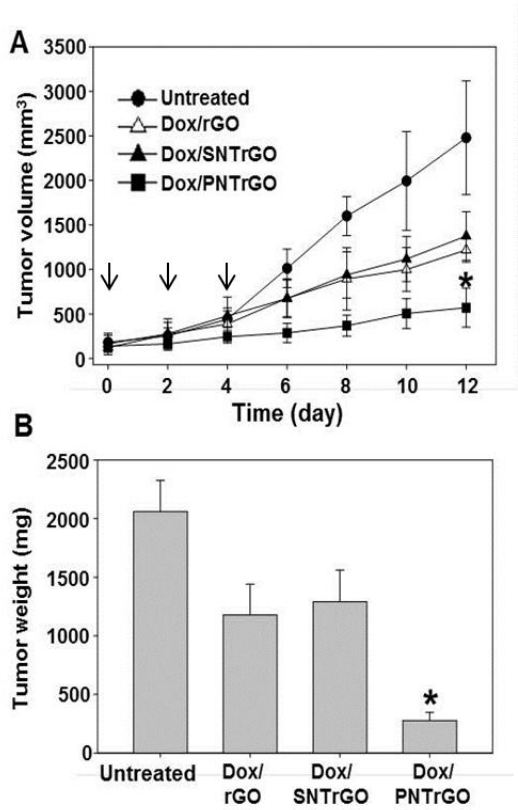

Fig. II-6. In vivo antitumor effects of Dox on nanothread-anchored rGO nanosheets.

(A) CCRF-CEM tumor-bearing mice were treated three times by intravenous administration of 3 mg/kg of Dox on rGO, SNTrGO, or PNTrGO every other day (arrows indicate administration day). (B) On day 12, tumor tissues were excised and weighed (n = 4; *p < 0.05 compared to other groups; ANOVA and Student-Newman-Keuls test).

- continued next page -

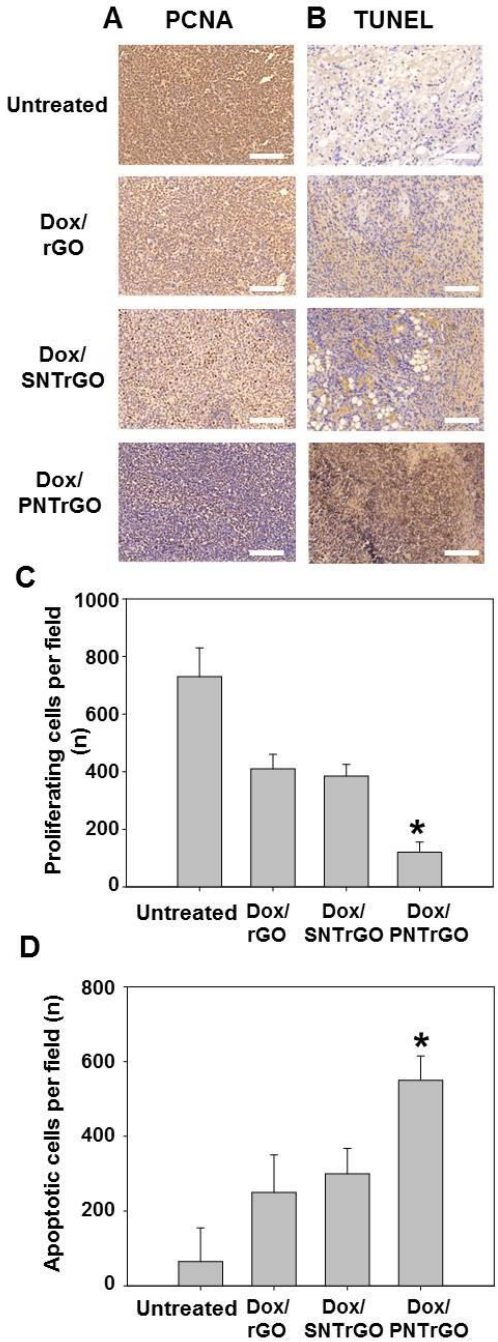
A
PCNA
B
TUNEL
Untreated
Dox/
rGO
Dox/
SNTrGO
Dox/
PNTrGO
C
Proliferating cells per field (n)
1000
800
600
400
200
0
*
Untreated
Dox/
rGO
Dox/
SNTrGO
Dox/
PNTrGO
D
Apoptotic cells per field (n)
800
600
400
200
0
*
Untreated
Dox/
rGO
Dox/
SNTrGO
Dox/
PNTrGO

Fig. II-7. Immunohistochemistry of tumor tissues.

Tumor tissues excised on day 12 after tumor inoculation were analyzed by immunostaining for PCNA (A) and by performing TUNEL assays (B). The numbers of PCNA-immunostained proliferating cells (C) and TUNEL-labeled apoptotic cells (D) in tumor tissue sections were determined (n = 4; *p < 0.05 compared to other groups; ANOVA and Student-Newman-Keuls test). Scale bar, 200 μm.

4. Discussion

In this study, it was demonstrated that PNTrGO nanosheets can be used for targeted delivery of anti-cancer drugs to PTK7-positive tumor tissues. The introduction of an oligoT bridge between aptamer sequences increased the ability of RCA nanothreads to anchor onto rGO nanosheets. Surface modification of rGO with PNT resulted in improved cellular uptake into PTK7-positive tumor cells lines and enhanced tumor tissue accumulation compared to SNTrGO nanosheets. Moreover, systemic administration of Dox using PNTrGO enhanced the antitumor effects in mice bearing PTK7-positive tumors.

TEM analyses revealed that PTK7-targeting polyaptamer sequences produced by RCA of ssDNA templates exhibited a nanothread-like morphology (Fig. II- 2A). In RCA reactions, π29 DNA polymerase replicates circular DNA templates over many rounds to yield products typically tens of thousands of nucleotides long [10,19].

PNT showed a greater ability to bind rGO nanosheets than PN (Fig. II-1C). The single-stranded oligoT bridge between each PTK7 aptamer sequence may serve as an rGO-anchoring unit. It has been reported that graphene-based nanosheets are capable of adsorbing ssDNA via π-π stacking interactions between the ring

structures in the nucleobases. Graphene-based nanosheets are known to have lower affinity for dsDNA or ssDNA with secondary and tertiary structure owing to shielding of nucleobases within the negatively charged phosphate backbone [20]. Since PTK7 aptamers possess a specific tertiary structure that enables binding to PTK7, the affinity of PTK7 aptamer alone for rGO nanosheets might be expected to be lower than that of oligoT sequences. Consistent with this supposition, the addition of oligoT sequence increased the binding of nanothreads onto rGO nanosheets.

In addition to conferring PTK7-recognition ability, PNT on rGO could serve as a dispersion stabilizer of rGO nanosheets in PBS. Poor solubility and aggregation in physiological buffers in the presence of salts have been linked to safety concerns surrounding the use of graphene-based nanosheets. Chemical modifications of surfaces with hydrophilic polymers such as PEG have been used to enhance the stability of graphene-based nanosheets [21]. In this latter study, adsorption of DNA onto the surface of GO nanosheets was reported to increase stability in aqueous solutions for several months, completely preventing aggregation [22]. The enhanced stability of PNTrGO in PBS observed here might offer greater stability of rGO nanosheets in serum after systemic administration.

PNTrGO was taken up by CCRF-CEM cells with greater efficiency than SNTrGO (Fig. II-3F). This enhanced cellular uptake of PNTrGO is attributable to the expression of PTK7 on CCRF-CEM cells (Fig. II-3B), as evidenced by the diminished uptake of PNTrGO by PTK7-negative Ramos cells (Fig. II-3A). Moreover, upon binding ligands, namely the PTK7-targeting DNA aptamer sgc8, PTK7 has been shown to undergo endocytosis [18], a crucial mechanism in the cellular entry of nanocarriers.

To visualize the cellular uptake and in vivo fate of PNTrGO, we labeled the surfaces of PNTrGO with the fluorescent lipid dye, DSPE-PEG_{5000}-Cy5.5, which adheres to the surfaces of rGO through hydrophobic interaction. Although graphene-based nanosheets exert a strong quenching effect on fluorescent probes, providing a sufficient distance from the surfaces of nanosheets can prevent fluorescence resonance energy transfer, thereby avoiding quenching. The relatively long PEG spacer in the DSPE-PEG_{5000}-Cy5.5 fluorescent lipid used here thus minimizes quenching upon adsorption to rGO surfaces.

In vivo molecular imaging data revealed that PNTrGO nanosheets exhibited enhanced tumor distribution (Fig. II-5D). The greater tumor distribution of PNTrGO implies that PNT was not degraded in the systemic circulation, and was

capable of recognizing and binding PTK7-expressing tumor cells upon arrival in tumor tissues. The adsorption of PNT onto rGO may have contributed to the enhanced stability of PNT against the nuclease-rich in vivo environment. Indeed, graphene-based nanosheets have been previously reported to protect DNA adsorbed onto the graphene surface from nuclease digestion [23]. Specifically, this latter study showed that a molecular beacon adsorbed onto graphene oxide surfaces was protected from enzymatic cleavage and was delivered to targeted cells, resulting in visualization and detection of intracellular survivin mRNA [24]. Another study reported enhanced nuclease resistance of ATP aptamers upon adsorption to graphene oxide nanosheets.

The anti-cancer effects of Dox were greatest both in vitro and in vivo after delivery using PNTrGO (Figs. II-4 and II-6). Although the release profile of Dox from graphene-based nanosheets is not fully characterized, it has been reported that release of Dox loaded onto pegylated GO nanosheets is facilitated in an acidic solution (pH 5.5), and is reduced at more neutral pH values (pH 7.4) [25]. Accordingly, as suggested by the results of a previous study , after endocytosis via PTK7, Dox on PNTrGO could be released in acidic endosomes and diffuse out to the nucleus.

Unlike CCRF-CEM cells, Ramos cells were not significantly killed by Dox on various rGO nanosheets (Fig. II-4B). The lack of anticancer effect of Dox on rGO nanosheets in Ramos cells may be attributed to the negligible cellular uptake. Regardless of surface modification of rGO nanosheets, all groups of Ramos cells showed little fluorescence signal of Cy5.5 (Fig. II-3E). In contrast, CCRF-CEM cells revealed the most intense fluorescence after treatment with DSPE-PEG_{5000}-Cy5.5 lipid-labeled PNTrGO (Fig. II-3F). The differential uptake of PNTrGO between PTK7-negative Ramos (Fig. II-A) and PTK7-positive CCRF-CEM cells (Fig. II-3B) supports the PTK7-mediated endocytosis of PNTrGO.

In conclusion, PNT containing a PTK7-recognizing polyaptamer and rGO-anchoring oligoT bridge sequences were constructed using RCA. Results in this study underscore the utility of surface coating of rGO with polyaptamer nanothreads that recognize tumor-overexpressed receptors for targeted delivery of anticancer drugs. Although PTK7 was used as the aptamer target and Dox as the anticancer drug in this study, PNTrGO could serve as a nanoplatform for other rGO loadable anticancer drugs and aptamer targets to provide specific delivery to tumor cells overexpressing other receptors.

5. References

[1] Huang YF, Chang HT, Tan W. Cancer cell targeting using multiple aptamers conjugated on nanorods. Anal Chem. 2008; 80: 567-572.

[2] Bagalkot V, Zhang L, Levy-Nissenbaum E, Jon S, Kantoff PW, Langer R. Quantum dot-aptamer conjugates for synchronous cancer imaging, therapy, and sensing of drug delivery based on bi-fluorescence resonance energy transfer. Nano Lett. 2007; 7: 3065-3070.

[3] Taghdisi SM, Lavaee P, Ramezani M, Abnous K. Reversible targeting and controlled release delivery of daunorubicin to cancer cells by aptamer-wrapped carbon nanotubes. Eur J Pharm Biopharm. 2011; 77: 200-206.

[4] Cao Z, Tong R, Mishra A, Xu W, Wong GC, Cheng J. Reversible cell-specific drug delivery with aptamer-functionalized liposomes. Angew Chem Int Edit. 2009; 48: 6494-6498.

[5] Kang H, O'Donoghue MB, Liu H, Tan W. A liposome-based nanostructure for aptamer directed delivery. Chem Commun. 2010; 46: 249-251.

[6] McNamara JO, Kolonias D, Pastor F, Mittler RS, Chen L, Giangrande PH. Multivalent 4-1BB binding aptamers costimulate CD8+ T cells and inhibit tumor growth in mice. J Clin Invest. 2008; 118: 376-386.

[7] Ali MM, Li F, Zhang Z, Zhang K, Kang DK, Ankrum JA. Rolling circle amplification: a versatile tool for chemical biology, materials science and medicine Chem Soc Rev. 2014; 43: 3324-3341.

[8] Cho EJ, Yang L, Levy M, Ellington AD. Using a deoxyribozyme ligase and rolling circle amplification to detect a non-nucleic acid analyte, ATP. J Am ChemSoc. 2005; 127: 2022-2023.

[9] Yang L, Fung CW, Cho EJ, Ellington AD. Real-time rolling circle amplification for protein detection. Anal Chem. 2007; 79: 3320-3329.

[10] Cheglakov Z, Weizmann Y, Braunschweig AB, Wilner OI, Willner I. Increasing the complexity of periodic protein nanostructures by the rolling-circle-amplified synthesis of aptamers. Angew Chem Int Edit. 2008; 47:126-130.

[11] Zhao W, Cui CH, Bose S, Guo D, Shen C, Wong WP. Bioinspired multivalent DNA network for capture and release of cells. Proc Natl Acad Sci USA. 2012; 109: 19626-19631.

[12] Liu J, Li Y, Lib J, Deng Z. Noncovalent DNA decorations of graphene oxide and reduced graphene oxide toward water-soluble metal–carbon hybrid nanostructures via self-assembly. J Mater Chem. 2010; 20: 900-906.

[13] Miao W, Shim G, Kang CM, Lee S, Choe YS, Choi HG. Cholesteryl hyaluronic acid-coated, reduced graphene oxide nanosheets for anti-cancer drug delivery. Biomaterials. 2013; 34: 9638-9647.

[14] Shangguan D, Li Y, Tang Z, Cao ZC, Chen HW, Mallikaratchy P. Aptamers evolved from live cells as effective molecular probes for cancer study. Proc Natl Acad Sci USA. 2006; 103: 11838-11843.

[15] Shangguan D, Cao Z, Meng L, Mallikaratchy P, Sefah K, Wang H. Cell-specific aptamer probes for membrane protein elucidation in cancer cells. J Proteome Res. 2008; 7: 2133-2139.

[16] Beyer S, Nickels P, Simmel FC. Periodic DNA nanotemplates synthesized by rolling circle amplification. Nano Lett. 2005; 5: 719-722.

[17] Zhang Y, Schwerbrock NMJ, Rogers AB, Kim WY, Huang L. Codelivery of VEGF siRNA and gemcitabine monophosphate in a single nanoparticle formulation for effective treatment of NSCLC. Mol Ther. 2013; 21: 1559-1569.

[18] Xiao Z, Shangguan D, Cao Z, Fang X, Tan W. Cell-specific internalization study of an aptamer from whole cell selection. Chemistry. 2008; 14: 1769-1775.

[19] Lee JB, Peng S, Yang D, Roh YH, Funabashi H, Park N. A mechanical metamaterial made from a DNA hydrogel. Nat Nanotechnol. 2012; 7: 816-820.

[20] He BS, Song B, Li D, Zhu C, Qi W, Wen Y. A graphene nanoprobe for rapid, sensitive, and multicolor fluorescent DNA analysis. Adv Funct Mater. 2010; 20:453-459.

[21] Zhu G, Zheng J, Song E, Donovan M, Zhang K, Liu C. Self-assembled, aptamer-tethered DNA nanotrains for targeted transport of molecular drugs in cancer theranostics. Proc Natl Acad Sci USA. 2013; 110:7998-8003.

[22] Lu CH, Zhu CL, Li J, Liu JJ, Chen X, Yang HH. Using graphene to protect DNA from cleavage during cellular delivery. Chem Commun. 2010; 46:3116-3118.

[23] Wang Y, Li Z, Hu D, Lin CT, Li J, Lin Y. Aptamer/graphene oxide nanocomplex for in situ molecular probing in living cells. J Am Chem Soc. 2010;132: 9274-9276.

[24] Sun X, Liu Z, Welsher K, Robinson JT, Goodwin A, Zaric S. Nano-graphene oxide for cellular imaging and drug delivery. Nano Res. 2008; 1: 203-212.

[25] Estrella V, Chen T, Lloyd M, Wojtkowiak J, Cornnell HH, Ibrahim-Hashim A. Acidity generated by the tumor microenvironment drives local invasion. Cancer Res. 2013; 73:1524-1535.

Chapter III

Biomimetic DNA nanoballs for targeted oligonucleotide delivery

1. Introduction

Recently, functional oligonucleotides have been studied as a major class of nucleic acid-based therapeutics [1]. Antisense oligonucleotides (ASOs) and micro RNA are examples of oligonucleotides with therapeutic potentials. However, these oligonucleotides suffer from drawbacks, such as instability against nucleases and limited cellular uptake owing to their high negative charges. To overcome these drawbacks, researchers delivered oligonucleotides using cationic lipids or polymer-based delivery systems. Cationic nanoparticles have previously been used to deliver single stranded oligonucleotides based on charge-charge loading to cationic liposomes [2,3] and polymer-based nanoparticles [4,5]. However, the cationic nanoparticle-associated cytotoxicity [6] requires the development of other carriers not cationic as well as biomimetic for delivery of oligonucleotides.

Rolling circle amplification (RCA) is an enzymatic process that produces a single-stranded DNA (ssDNA) from a circular template. The resulting ssDNA is composed of complementary-sequence repeats of the circular template. RCA technology was originally used for DNA detection in genomics; however, additional applications using RCA have been reported [7]. Recently, RCA was

applied to construct DNA nanostructures and DNA hydrogels [8-11].

In this study, RCA-amplified DNA was used to produce an oligonucleotide delivery system. As model oligonucleotides, two ASO oligonucleotides were selected. To load ASO to the delivery system, sequence-specific hybridization was used rather than cationic nanoparticle-based charge-charge interaction. The template for RCA was designed to have complementary sequences for two different ASOs and to produce poly-binding sites for ASOs upon RCA amplification. Exploiting the DNA condensation mechanisms of viruses, cationic Mu peptides derived from the adenovirus core complex were employed to condense ASO-hybridized RCA products (ARP) and produce DNA nanoballs. The surface of ASO-loaded DNA nanoballs was coated with hyaluronic acid (HA), a ligand for CD44 receptors overexpressed by tumor cells [12], for tumor-targeted delivery.

Here, DNA nanoballs with ASO-complementary sequences provided sequence-specific loading of dual ASOs, and coating with HA promoted CD44 receptor-mediated delivery of ASOs to tumor cells. Importantly, ASOs delivered by HA-coated DNA nanoballs silenced the expression of their target mRNAs of ASO, exerting potent anticancer effects in vitro and in vivo.

2. Materials and methods

2.1. Construction of ASO-hybridized DNA nanoballs

ASO-hybridized DNA nanoballs were constructed by (1) amplifying ssDNA containing ASO-binding sites by RCA, (2) hybridizing with ASO, and (3) condensing with cationic Mu peptides. In the first step, an RCA template for complementary binding with ASOs was circularized using primers. Briefly, 0.5 μM of 5'-phosphorylated linear ssDNA template and primer (Macrogen Inc., Daejeon, Republic of Korea) were annealed in hybridization buffer (10 mM Tris-HCl, 1 mM EDTA, 100 mM NaCl, pH 8.0) and mixed with T4 DNA ligase (125 units/mL) (Thermo Scientific, Waltham, MA, USA) to close the nick in the circular RCA template. After inactivating T4 DNA ligase by heating to 70℃, the circular RCA template (200 μL) was incubated at 30℃ for 12 h with π29 DNA polymerase (100 units/mL) (Thermo Scientific) and 2 mM dNTPs (Intron Biotechnology Inc., Seoul, Republic of Korea). In some experiments, fluorescent RCA products were prepared by adding 25 μM of Cy5-dCTP to 2 mM dNTPs during the RCA reaction. After heat-inactivating π29 DNA polymerase at 70℃ for 10 min, residual dNTPs were removed by centrifugation at 13,000 rpm for 10 min. The resulting pellet of RCA product was resuspended in water, and its

concentration was measured using a Nanodrop spectrophotometer (Thermo Scientific). Two different ASOs—Dz13 (125 μg) and OGX-427 (125 μg)—were hybridized with 1 mL of RCA products (500 μg DNA/mL) by heating at 95℃ for 10 min and then cooling gradually at room temperature. The cationic Mu peptide (Peptron, Daejeon, Republic of Korea) was added to the resulting dual ARP at a weight ratio of 1:1 to form a nanoball-like structure. The resulting complexes of Mu-condensed, dual ASO-hybridized DNA nanoballs (MA nanoballs) were mixed with 214 kDa HA (Lifecore Biomedical Inc., Chaska, MN, USA) at a DNA:Mu:HA weight ratio of 1:1:5. HA-coated, Mu-condensed, dual ASO-hybridized DNA nanoballs (HMA nanoballs) were stored at 4℃ until use. In some experiments, RCA products alone were mixed with Mu peptide at a weight ratio of 1:1, and coated with HA at a DNA:Mu:HA ratio of 1:1:5 to produce HA-coated, Mu-condensed DNA nanoballs without ASOs (HM nanoballs).

2.2. Quantification of hybridized ASOs

The two ASOs, Dz13 and OGX-427, were labeled using different fluorescent dyes to measure the efficiency of hybridization to RCA products. Fluorescein

(FAM)-conjugated Dz13 and 6-carboxy-x-rhodamine (ROX)-tagged OGX-427 were supplied by Bioneer Corporation (Daejeon, Republic of Korea). The fluorescent dye-modified ASOs, FAM-Dz13 and ROX-OGX-427 (5.5 μg each), were hybridized with 100 μL of RCA products (200 μg DNA/mL). The procedure described in section 2.1 was adopted for loading fluorescent dye-modified ASOs to RCA products. Unloaded fluorescent ASOs were removed by repeated centrifugation at 13,000 rpm for 10 min, and the fluorescence intensity of the supernatants was measured using a Spectramax Gemini XS microplate fluorometer (Molecular Devices Co., Sunnyvale, CA, USA). The amounts of hybridized Dz13 and OGX-427 were calculated from calibration curves of fluorescence intensity of each fluorescent dye-labeled ASO as a function of concentration.

2.3. Characterization study of DNA nanoballs

The sizes of various DNA nanoballs, with or without Mu peptide-induced condensation and HA coating, were measured by dynamic light scattering. The zeta potentials of DNA nanoballs were also measured by laser Doppler

microelectrophoresis at an angle of 22° using an ELSZ-1000 instrument (Photal, Osaka, Japan). The morphology of DNA nanoballs was visualized by scanning electron microscopy (SEM) using a Supra 55VP system (Carl Zeiss, Oberkochen, Germany). The stability of ARP, MA nanoballs, and HMA nanoballs against nucleases was tested by incubating 1 μg of DNA with 1 unit of DNase I (Sigma-Aldrich, St. Louis, MO, USA) at 37℃ for 30 min. The mixture was electrophoresed on 1% agarose gels and visualized by staining with Safe-Pinky dye (GenDepot, Barker, TX, USA).

2.4. Cellular uptake test of DNA nanoballs

Cellular uptake of various DNA nanoballs was evaluated by preparing fluorescent DNA nanoballs using 25 μM Cy5-dCTP (Perkin Elmer, Boston, MA, USA) and DNA nanoballs carrying fluorescent dye-modified ASOs, as described above. KB human epidermal carcinoma cells (American Type Culture Collection, Rockville, MD, USA) were cultured in RPMI-1640 medium (Welgene, Daegu, Republic of Korea) supplemented with 10 % fetal bovine serum and 100 units/mL penicillin plus 100 μg/mL streptomycin. KB cells were seeded onto

poly-L-lysine coated coverslips (BD Biosciences, San Jose, CA, USA) in 24-well plates (SPL Life Sciences, Pocheon, Republic of Korea) at a density of 8×10^4 cells/well. The next day, cells were treated with Cy5-dCTP–incorporated fluorescent DNA nanoballs or fluorescent dye-modified ASO-loaded DNA nanoballs at a concentration of 20 μg DNA/well. In some experiments, cells were pre-incubated with 10 μM HA for 2 h prior to treatment with DNA nanoballs. For fluorescence microscopy, cells were washed and fixed with 4 % paraformaldehyde in phosphate-buffered saline (PBS) for 15 min, and stained with 4',6-diamidino-2-phenylindole dihydrochloride (DAPI). The fluorescence of cells was observed using a confocal laser-scanning microscope (LSM 5 Exciter; Carl Zeiss, Inc., Jena, Germany). For flow cytometry, the cells were harvested and washed three times with cold PBS containing 2 % fetal bovine serum, and analyzed using a BD FACSCalibur system equipped with Cell Quest Pro software (BD Biosciences).

2.5. Knockdown study of target protein expression

In vitro silencing of target protein expression by DNA nanoballs was evaluated

by Western blotting. Various DNA nanoballs were applied to KB cells seeded in 6-well plates. After 1 h incubation, the cell medium was replaced and cells were incubated for an additional 24 h. Whole-cell lysates were then prepared, and extracted proteins were quantified using a BCA protein assay kit (Thermo Scientific) according to the manufacturer's instruction. Proteins in samples were separated by sodium dodecyl sulfate-polyacrylamide gel electrophoresis (SDS-PAGE) on 10 % gels and then transferred onto polyvinylidene difluoride membranes (Hybond-ECL; Amersham Biosciences, Piscataway, NJ, USA). Membranes were probed by Western blotting using specific antibodies to c-Jun (1:500, sc-1694; Santa Cruz Biotechnology, CA, USA), Hsp27 (1:500, sc-9012; Santa Cruz Biotechnology), and glyceraldehyde-3-phosphate dehydrogenase (GAPDH; 1:1000, sc25778; Santa Cruz Biotechnology).

2.6. Assessment of DNA nanoball anticancer activity

The cancer cell-killing effect of various DNA nanoballs was quantitatively evaluated using a Cell Counting Kit 8 (CCK-8; Dojindo Lab., Kumamoto, Japan) and visualized by staining of live cells after treatment with DNA nanoballs. KB

cells were seeded in 48-well plates at a density of 6×10^4 cells/well. The next day, the cells were treated with various types of DNA nanoballs at a constant amount of DNA (20 μg/well). After a 1 h incubation in the presence or absence of 1 μM doxorubicin (Dox), the cell medium was replaced and cells were incubated for an additional 24 h. Cell viability was then measured by CCK-8 assay. For CCK-8 assays, 20 μL of CCK-8 solution was added to each well and plates were incubated for 30 min. The absorbance of the medium at 450 nm was then measured colorimetrically using an enzyme-linked immunosorbent assay (ELISA) reader (Sunrise-Basic TECAN, Mannedorf, Switzerland). For live cell staining, cells were stained with calcein-AM (Molecular Probes, Eugene, OR, USA) after treatment with various DNA nanoballs.

2.7. In vivo molecular imaging

The in vivo tumor distribution of Cy5-dCTP–labeled DNA nanoballs was assessed by molecular imaging. Five-week-old athymic nude mice (Orient Bio Inc., Seongnam, Korea) were subcutaneously inoculated with 5×10^5 KB cells. After tumors had reached a volume of ~100 mm^3, fluorescent HMA or MA

nanoballs were intravenously injected into the mice at a dose of 4 mg DNA/kg. After 1 h, the intensity of Cy5 signals was monitored using an eXplore Optix system (Advanced Research Technologies Inc., Montreal, Canada) and scanned using a 670 nm laser at a power of 25 mW and a count time of 0.3 s/point.

2.8. In vivo study of anti-tumor effects

The in vivo anti-tumor activity of DNA nanoballs was evaluated by measuring tumor growth-inhibitory effects. KB cells (5×10^5 cells) were subcutaneously inoculated into the dorsal right side of 5-wk-old athymic nude mice (Orient Bio). After tumors had become established, DNA nanoballs and Dox were intravenously administrated at a DNA dose of 8 mg/kg and a Dox dose of 3 mg/kg. For MA and HMA nanoballs, the doses of ASOs were 2 mg/kg each for Dz13 and OGX-427. Mice were treated with the mixture of DNA nanoballs and Dox every other day for a total of three injections. Tumor size was measured in two dimensions using a slide caliper every 2 days, and tumor volume was calculated as $a \times b \times b \times 0.5$, where a and b are the lengths of the largest and smallest dimensions. The mice were sacrificed on day 14, and tumor tissues were

extracted and weighed.

2.9. Statistics

All statistical analyses were performed using analysis of variance (ANOVA) with a post hoc Student–Newman–Keuls test. SigmaStat software (version 3.5; Systat Software, Richmond, CA, USA) was used for the analyses, and a p-value less than 0.05 was considered statistically significant.

3. Results

3.1. Sequence-specific hybridization of dual ASOs onto DNA nanoballs

The sequences of scrambled and dual ASO-complementary RCA templates are illustrated in Fig. III-1A and III-1B, respectively. ARP was formed by hybridization of Dz13 and OGX-427 (Fig. III-1C). Loading amounts of Dz13 and OGX-427 onto RCA products depended on the sequences of RCA templates. As compared to RCA products of scrambled template, the RCA products of dual ASO-complementary RCA templates provided 8.1- and 6.7-fold higher loading amounts for Dz13 and OGX-427, respectively (Fig. III-1D). ARP was then treated with adenovirus-derived Mu peptide to produce Mu peptide-condensed, dual ASO-loaded DNA nanoballs (MA nanoballs). HA was then complexed with MA nanoballs to form HA-coated, Mu peptide-condensed, dual ASO-loaded DNA nanoballs (HMA nanoballs) for targeted delivery of ASOs to tumors overexpressing the receptor, CD44.

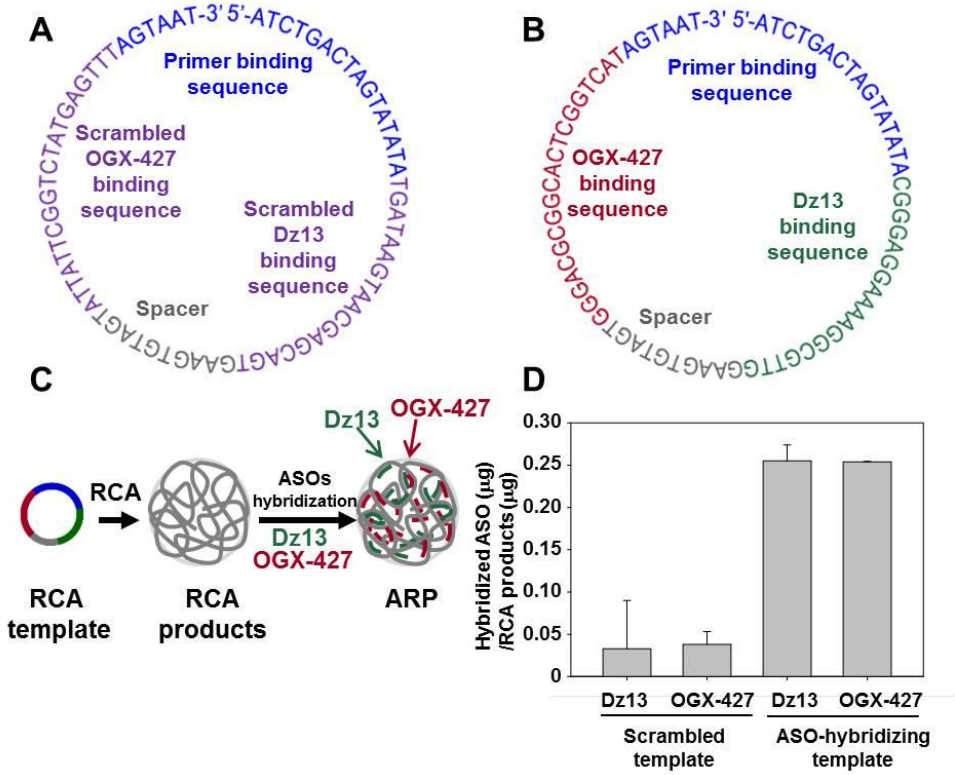

Fig. III-1. RCA template and hybridization efficiency.

(A) Secondary structure of scrambled RCA template. (B) Secondary structure of a dual ASO-hybridizing RCA template for Dz13 and OGX-427. (C) RCA products with poly ASO-binding sequences were hybridized with two ASOs, Dz13 and OGX-427, to produce dual ARP. (D) The hybridization efficiencies of the ASOs, Dz13 and OGX-427, were tested for products of scrambled RCA templates and dual ASO-hybridizing RCA templates using fluorescently labeled ASOs (FITC-Dz13, ROX-OGX-427).

3.2 Characterization of ASO-hybridized DNA nanoballs

The structures of various DNA nanoballs are illustrated in Fig. III-2A. Mu peptide-complexed ARP exhibited nanoball-like structures (Fig. III-2B, III-2C). Surface coating of MA nanoballs with HA retained nanoball-like structures (Fig. III-2B, III-2C). The size (Fig. III-2D) and zeta potential (Fig. III-2E) of ARP were 1,242.5 nm ± 320.4 nm and -29.1 mV ± 11.5 mV, respectively. Addition of cationic Mu peptide reduced the size to 162.7 nm ± 32.4 nm and increased the zeta potential to 5.0 mV ± 1.4 mV. After surface coating with HA, the size of nanoballs was 191.4 nm ± 15.1 nm, and the zeta potential was -21.8 mV ± 0.7 mV. Both MA nanoballs and HMA nanoballs showed stability against nucleases (Fig. III-2F). Upon 30 min treatment with DNase I, ARP was completely degraded and migrated to the bottom of agarose gels. In contrast, agarose gel electrophoresis showed no degraded DNA fragments of MA nanoballs or HMA nanoballs after DNase I treatment. Thus, adenovirus-derived cationic Mu peptide substantially decreased the size of ARP, increased their zeta potential values, and provided stability against nuclease.

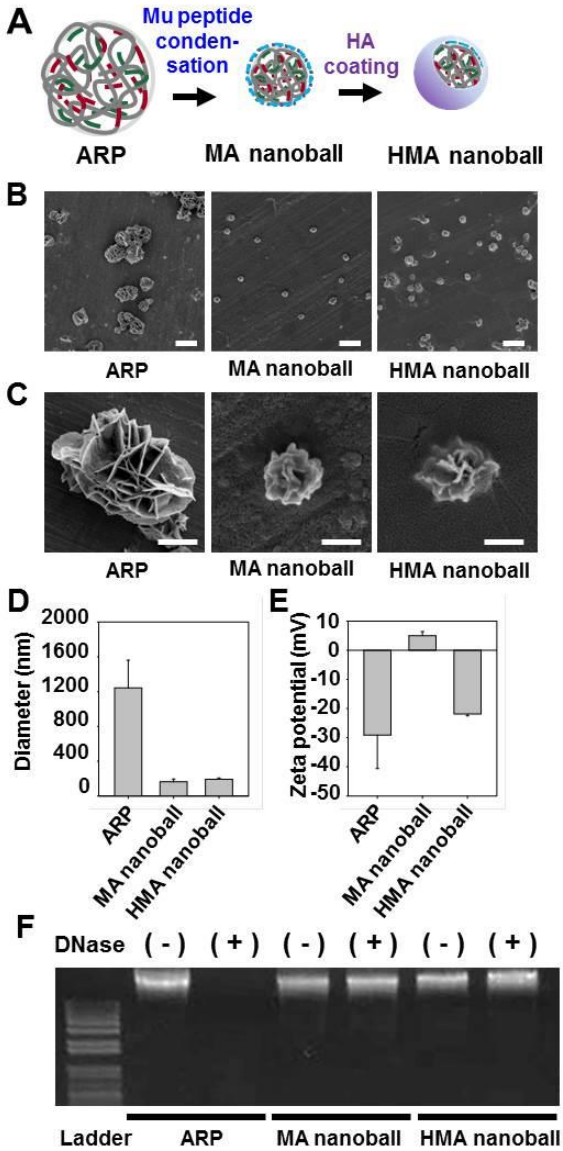

Fig. III-2. Schematic illustration and morphology of DNA nanoballs.

(A) Illustration of the HMA nanoball preparation scheme. Dual ARP were mixed with adenovirus core complex-derived Mu peptide to form MA nanoballs. The

- continued next page -

surfaces of MA nanoballs were coated with HA to produce HMA nanoballs. (B,C) The morphologies of ARP, MA nanoballs, and HMA nanoballs were observed by SEM at different magnifications. Scale bar: 2 um for all groups (B). Scale bar: 800 nm for ARP and 200 nm for MA nanoball and HMA nanoballs (C). (D) The sizes of ARP, MA nanoballs, and HMA nanoballs were measured by dynamic light scattering. (E) Zeta potential values of ARP, MA nanoballs, and HMA nanoballs were determined by laser Doppler microelectrophoresis. (F) The stability of ARP, MA nanoballs, and HMA nanoballs against DNase I was tested by incubation with 1 unit of DNase I for 30 min, followed by electrophoresis on a 1 % agarose gel.

3.3. Cellular uptake of DNA nanoballs and dual ASOs

HMA nanoballs entered KB cells via CD44 receptors. To visualize and quantitate the cellular uptake of DNA nanoballs, we used Cy5-incorporated DNA nanoballs by running RCA using Cy5-dCTP. Confocal microscopy (Fig. III-3A) and flow cytometry (Fig. III-3B, III-3C) showed little uptake of Cy5-dCTP-incoroporated fluorescent ARP or MA nanoballs by CD44-overexpressing KB cells, but revealed considerable entry of fluorescent HMA nanoballs into KB cells. The enhanced cellular uptake of MA nanoballs caused by HA-coating was not observed when the cells were pretreated with free HA.

As a complementary approach, we examined cellular uptake of DNA nanoballs containing hybridized, fluorescently labeled ASOs. Consistent with the above results, confocal microscopy (Fig. III-4A) and flow cytometry showed considerable entry of FAM-conjugated Dz13 (Fig. III-4B) and ROX-conjugated OGX-427 (Fig. III-4C) into CD44-overexpressing KB cells, but little uptake of these fluorescent ASOs when hybridized to MA nanoballs, which lack HA (Fig. III-4D). Again, this enhancement of cellular uptake of MA nanoballs by HA-coating was eliminated by pretreating cells with free HA. Collectively, these results confirm the CD44 receptor-dependence of HMA nanoball uptake.

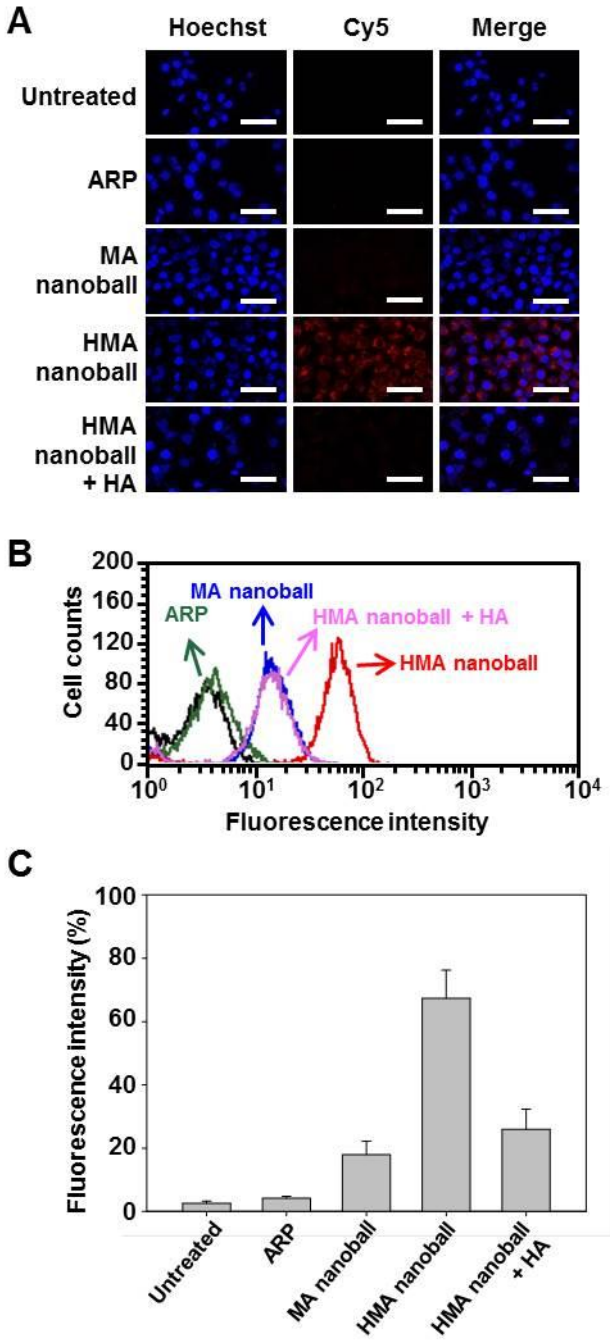

- continued next page -

Fig. III-3. Cellular uptake of DNA nanoballs.

KB cells were left untreated or were treated with ARP, MA nanoballs or HMA nanoballs, with or without HA pre-treatment. Cellular uptake of Cy5-incorporated fluorescent DNA nanoballs was visualized by confocal microscopy (A) and quantified by flow cytometry (B, C). (B) Representative flow cytometry data. (C) Quantification of populations of fluorescence-positive cells. Data are presented as means ± SE (n = 4). Scale bar: 20 μm.

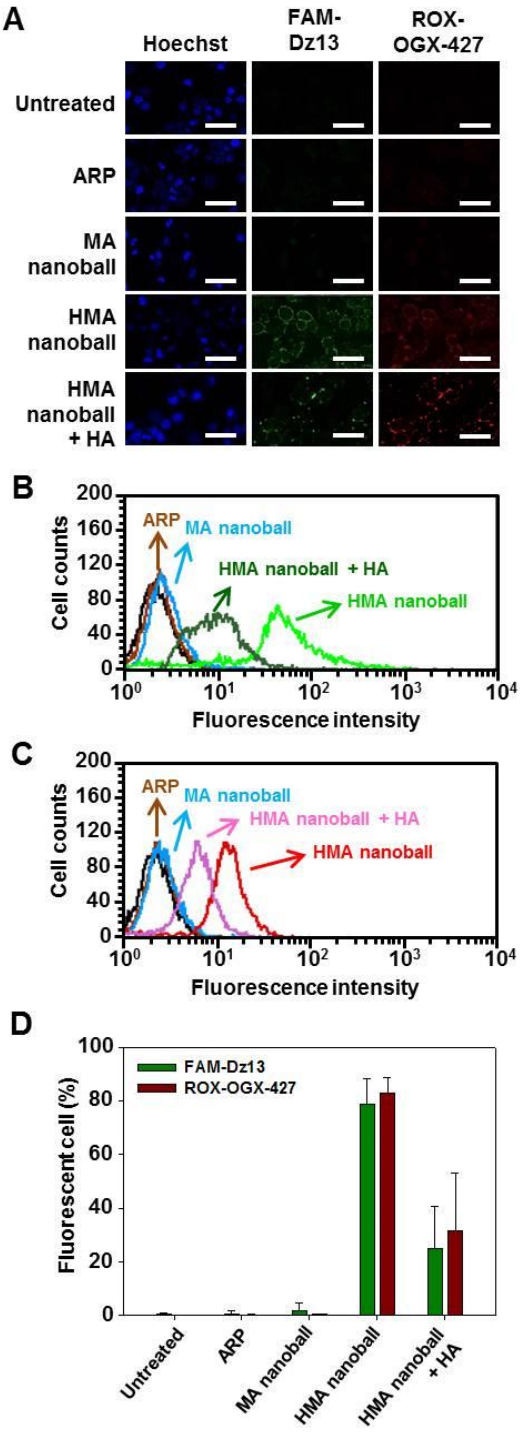

- continued next page -

Fig. III-4. Cellular uptake of ASOs.

KB cells were left untreated or were treated with ARP, MA nanoballs or HMA nanoballs, with or without HA pre-treatment. (A) Cellular uptake of FAM-Dz13 and ROX-OGX427 ASOs loaded in DNA nanoballs was visualized by confocal microscopy. (B, C) Representative flow cytometry data for cell populations positive for FAM-Dz13 (B) and ROX-OGX427 (C) under various conditions. (D) Flow cytometry-based quantification of populations of fluorescent (ASO-positive) cells. Data are presented as means ± SE (n = 3). Scale bar: 20 μm.

3.4. Reduction of target protein expression by DNA nanoballs

The effect of HMA nanoballs on the expression levels of proteins targeted by the dual hybridized ASOs: c-Jun, the target of the DNAzyme Dz13, and Hsp27, the target of OGX-427 was investigated. Downregulation of target proteins was monitored by Western blotting (Fig. III-5), which showed that treatment of KB cells with HMA nanoballs decreased the protein levels of c-Jun and Hsp27 to 33.0 % ± 9.5 % (Fig. III-5A) and 12.6 % ± 7.2 % (Fig. III-5B) of control levels, respectively. In contrast, treatment of KB cells with HM or MA nanoballs alone did not significantly reduce the levels of either protein (Fig. III-5C).

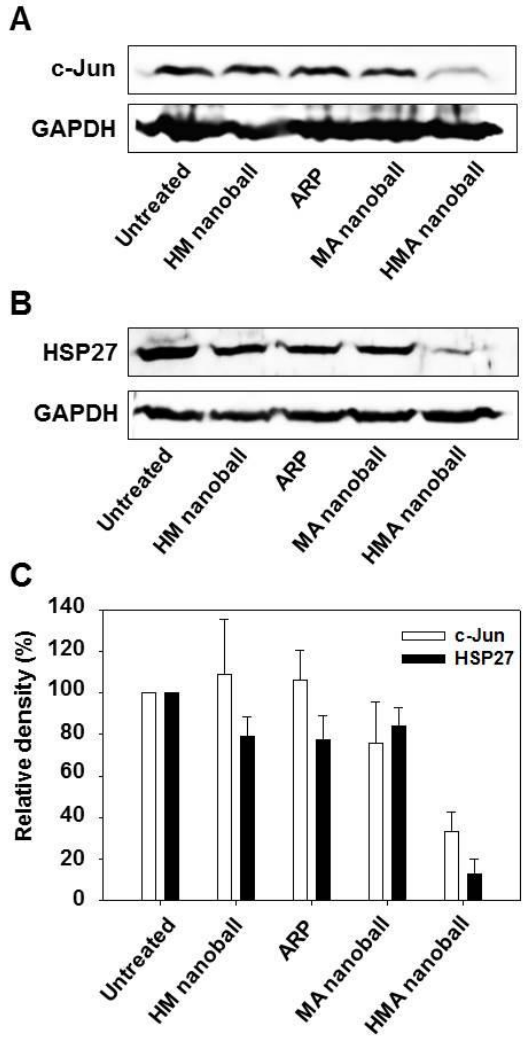

Fig. III-5. Reduction of target proteins.

The cellular protein levels of target genes, c-Jun (A) and Hsp27 (B), were measured by Western blotting. After various treatments, whole-cell extracts of KB cells were analyzed for target proteins by Western blotting. The data are expressed as means ± SE (n = 3). (C) Relative intensities of c-Jun and Hsp27 were normalized to the GAPDH signal.

3.5. In vitro anticancer effects of DNA nanoballs

Among the various DNA nanoballs, HMA nanoballs showed the greatest in vitro anticancer effect and synergized with Dox to further enhance anticancer efficacy. CCK-8 assay results reveal that the survival of KB cells was not significantly reduced by treatment with ARP, HM, or MA nanoballs (Fig. III-6A). However, treatment of KB cells with HMA nanoballs reduced the survival of KB cells to 69.3 % ± 1.7 % of control levels; co-treatment of KB cells with Dox and HMA nanoballs further reduced survival to 51.5 % ± 5.1 % (Fig. III-6A). Similar to the CCK-8 assay results, the fluorescent microscopy of live cells exhibited the lowest live cell populations in the group treated with HMA nanoballs (Fig. III-6B).

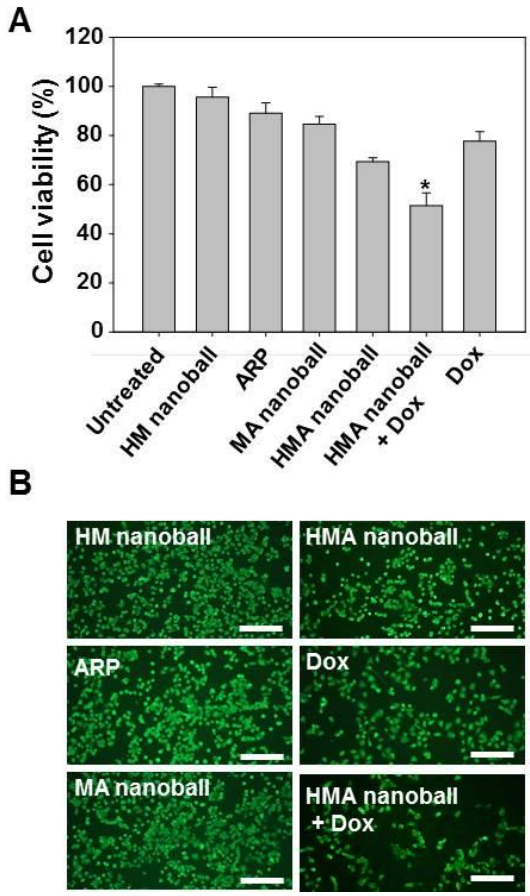

Fig. III-6. In vitro tumor cell-killing effect.

(A) KB cells were treated with ARP, MA nanoballs, HM nanoballs, or HMA nanoballs in the presence or absence of Dox for 1 h. After media replacement, the cells were incubated for an additional 24 h. The survival of cancer cells was determined by CCK-8 assay. Data are presented as means ± SE (n = 4). (B) The live cell population was stained with calcein-AM and observed by fluorescence microscopy. Scale bar: 20 μm.

3.6. Biodistribution and in vivo antitumor effects of DNA nanoballs

The effect of surface coating with HA on tumor tissue accumulation was examined. Moreover, antitumor effects of intravenously administered HMA nanoballs were also evaluated. For molecular imaging, Cy5-incorporated fluorescent nanoballs were injected into KB cell tumor-bearing nude mice. The tumor tissue distribution of Cy5-incorporated HMA nanoballs 1 h post-dose was greater than that of Cy5-incorporated MA nanoballs (Fig. III-7A). At 24 h post-injection, total photon counts in tumor tissues were 5.9-fold higher in the HMA nanoball-treated group than in the MA nanoball-treated group (Fig. III-7B).

Collectively, these results indicate that surface coating of MA nanoballs with HA enhances tumor tissue accumulation. Systemic co-administration of HMA nanoballs with Dox synergistically inhibited tumor growth in a KB cell xenograft mouse model. Compared to other groups, the HMA nanoball-treated group showed the lowest tumor volume (Fig. III-8A) and weight (Fig. III-8B).

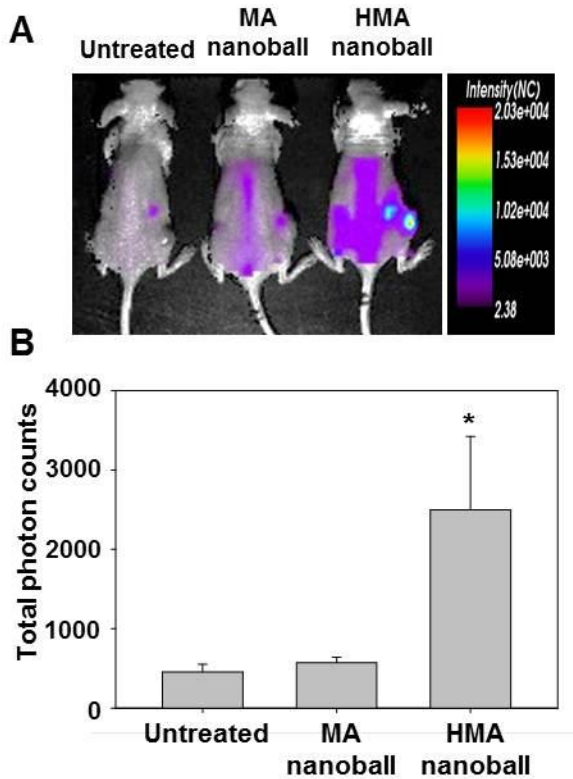

Fig. III-7. Biodistribution of ASO-loaded DNA nanoballs.

(A) KB tumor-bearing mice were intravenously injected with MA nanoballs or HMA nanoballs containing Cy5-dCTP. The biodistribution of Cy5 fluorescence was visualized using a molecular imaging system. (B) The total photon counts of tumor tissues from treated mice were quantified 1 h post-administration by in vivo imaging and compared with those of the untreated group.

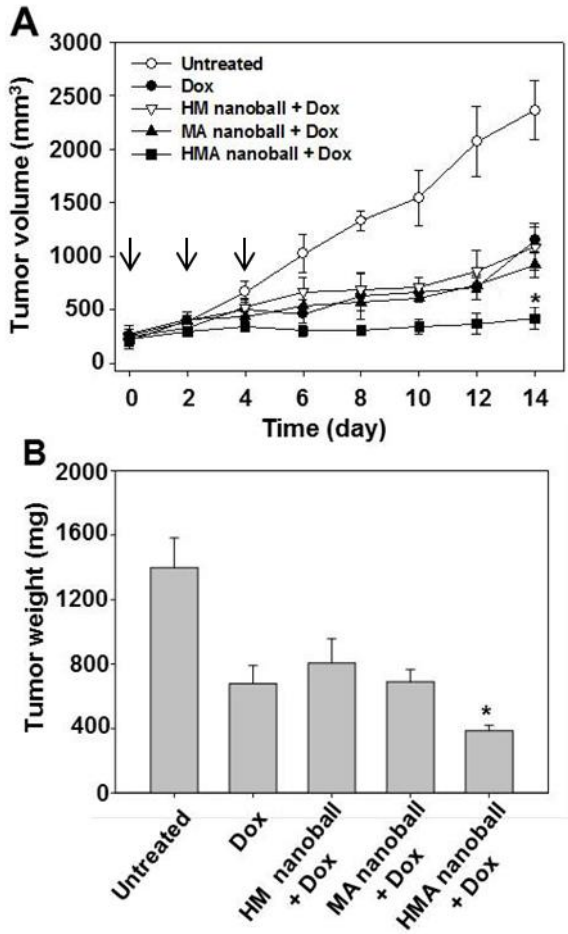

Fig. III-8. In vivo antitumor effect of ASO-loaded DNA nanoballs.

KB tumor-bearing mice were intravenously injected with HM nanoballs, MA nanoballs, or HMA nanoballs (8 mg DNA/kg) and Dox (3 mg Dox/kg) or with Dox alone (3 mg Dox/kg) every other day for a total of three injections (arrows indicate injection day). For MA and HMA nanoballs, the dose of both ASOs was 2 mg/kg. Tumor sizes were measured until day 14 (A), and tumor tissues were extracted and weighed (B).

4. Discussion

Here, the adenovirus-derived Mu peptide played an essential role in condensing ARP to form MA nanoballs, and surface coating with HA promoted CD44 receptor-mediated delivery of HMA nanoballs to tumor cells. Importantly, ASOs delivered by HMA nanoballs silenced the expression of their target mRNAs of ASO, exerting potent anticancer effects in vitro and in vivo upon co-treatment with Dox.

The goal of this study was to test the delivery of therapeutic oligonucleotides via nucleic acid-based DNA nanoballs using sequence-specific hybridization as a loading technique. ssDNA amplified by a RCA reaction can serve as an ASO sequence-specific carrier owing to its thousands of complementary sequences to the ASO. Compared to a scrambled RCA template, RCA templates containing ASO-binding sequences hybridize substantially higher amounts of ASO per RCA product (Fig. III-1D). This high hybridization capacity supports the feasibility of using hybridization-mediated ASO loading of RCA products for sequence-specific ASO delivery.

Dual ASOs—Dz13 and OGX-427 were loaded onto HMA nanoballs in a sequence-specific manner (Fig. III-1B). Dz13 is a DNAzyme with RNA-binding

hybridization arms that cleaves the mRNA of c-Jun, which is involved in cellular proliferation, transformation, and cell death [13]. OGX-427 is known to inhibit the expression of Hsp27, which is involved in cancer progression and cell death [14].

The adenovirus core complex-derived Mu peptide was used for biomimetic condensation of micrometer- to nanometer-sized DNA balls (Fig. III-2). In the absence of Mu peptide, the dual ASO-loaded ssDNAs tended to form a soft, "ball" in solution with a diameter of approximately 1.5 μm (Fig. III-2C). Our observations are consistent with a previous report, which showed that micrometer-sized DNA balls are produced by a RCA reaction [15,16]. The interaction between ARP and cationic Mu peptides is electrostatic, resulting in an increase in the zeta potential after condensation (Fig. III-2D).

Cellular uptake of ASO by CD44 receptor-overexpressing KB cells was enhanced by delivery using HMA nanoballs compared with MA nanoballs (Fig. III-3 and III-4), supporting the role of the HA moiety in enhancing CD44 receptor-mediated cellular delivery of DNA nanoballs. HA has been previously reported to increase the tumor cell delivery of nanoparticles by interacting with CD44 receptors; when conjugated to ASOs, it enhances their cellular delivery

[17].

The reduction in target protein levels after treatment of cells with HMA nanoballs is attributable to the enhanced uptake of nanoballs via the HA moiety and implies effective delivery of ASOs to the interior of the cell. The reduced cellular uptake of HMA nanoballs (Fig. III-3) and ASO (Fig. III-4) after pretreatment with HA supports the conclusion that the entry of HMA nanoballs into KB cells is mediated by the CD44 receptor. Although further study will be required to elucidate the intracellular fate of HMA nanoballs, we speculate that HMA nanoballs may be partially degraded in endolysosomes, enabling escape of ASOs into the cytosol and binding to target mRNA.

Owing to the greater affinity of the ASOs, Dz13 and OGX-427, for their target mRNA compared to that for the complementary ASO-binding sequence, the uptake of HMA nanoballs into cells resulted in the dissociation of ASOs from HMA nanoballs and binding to their target mRNA. In addition to the natural preference of ASOs for their natural target mRNAs, dissociation of ASOs from ARP was further facilitated by modifying the RCA template for complementary binding with ASO to contain one mismatched base pair for each ASO. Such facilitated dissociation caused by a single mismatch has been previously

demonstrated [18].

Combination treatment with Dox and HMA nanoballs showed the greatest in vivo antitumor effect (Fig. III-8). The target proteins of two ASOs, Dz13 and OGX-427, have been reported to be involved in the anticancer mechanisms by Dox [26, 27]. Treatment of small lung cancer cells with Dox was shown to induce multidrug resistance protein 1 [19]. In the study, the inhibition of c-Jun phosphorylation was observed to reduce the Dox-induced multidrug resistance protein 1 expression and increase sensitivity of the small lung cancer cells to Dox. Overexpression of Hsp 27, the target protein of OGX-427, was found to decrease the intracellular level of topoisomerase II, which is important for sensitivity and initiation of apoptosis by Dox [20]. Specific inhibitors of c-Jun and Hsp 27 were found to increase chemosensitivity of cancer cells to Dox [21, 22]. Inhibition of c-Jun by Dz13 was shown to enhance the sensitivity of cancer cells to Dox treatment. A recent study reported that the reduced expression of Hsp 27 by resveratrol or short hairpin interfering RNA could sensitize MCF-7 breast cancer cells to Dox. Based on these findings, the higher in vivo antitumor activity of HMA nanoballs with co-treatment of Dox would be in part due to the enhanced chemosensitivity of KB cells to Dox by reduction of c-Jun and Hsp 27.

Moreover, the enhanced in vivo antitumor activity in the Dox/HMA nanoball co-treatment group could be attributable to the higher tumor accumulation of HMA revealed by molecular imaging (Fig. III-7). The improved stability of HMA nanoballs against DNase I could contribute to prolonging the circulation of DNA nanoballs in serum following intravenous administration. Our in vitro fluorescence microscopy and flow cytometry data revealed that the cellular uptake of HMA nanoballs and ASO significantly reduced after pre-treatment with free HA, supporting the possibility of enhanced tumor distribution of CD44-positive KB xenografted mice. Previously, to test whether HA microparticles enter tumor cells by CD44 receptor-mediated endocytosis in vivo, the tumor accumulation patterns of HA microparticles were compared between CD44-positive and CD44-negative tumor bearing mice [23]. Since MA nanoballs and HMA nanoballs differ in the surface charges, we can't exclude the contribution of negative surface charges of HMA nanoballs to the in vivo tumor distribution. Future study would be thus necessary to compare the distribution and antitumor activity of HMA nanoballs in CD44-positive and CD44-negative tumor-xenografted mice models.

In this study, biomimetic HMA nanoballs were developed for in vitro and in vivo

delivery of functional oligonucleotides. RCA was used to amplify ASO-binding sequences, and dual ASOs were loaded onto HMA nanoballs through sequence-specific complementary hybridization. Soft, ball-shaped, ASO-loaded RCA products were condensed to nanoballs upon biomimetic condensation with adenovirus core complex-derived Mu peptide. Surface coating of MA nanoballs with HA facilitated the delivery of ASOs to cells and reduced the levels of target mRNAs. Co-treatment of HMA nanoballs with Dox improved anti-tumor efficacy. Although we used OGX-427 and Dz13 as model ASOs, the application of HMA nanoballs as an ASO delivery nanoplatform could be extended by replacing the ASO-binding sequences of the RCA template and hybridizing with other therapeutic ASOs. Results in this study thus suggest the potential of HMA nanoballs for non-cationic and sequence specific oligonucleotide delivery systems.

5. References

[1] Kole R, Krainer AR, Altman S. RNA therapeutics: beyond RNA interference and antisense oligonucleotides. Nature Rev Drug Discov. 2012; 11: 125-140.

[2] Cai H, Santiago FS, Prado-Lourenco L, Wang B, Patrikakis M, Davenport MP. DNAzyme targeting c-jun suppresses skin cancer growth. Sci Transl Med. 2012; 4: 1-12.

[3] Luvino D, Khiati S, Oumzil K, Rocchi P, Camplo M, Barthélémy P. Efficient delivery of therapeutic small nucleic acids to prostate cancer cells using ketal nucleoside lipid nanoparticles. J Control Release. 2013; 172: 954-961.

[4] Hadaschik BA, Jackson J, Fazli L, Zoubeidi A, Burt HM, Gleave ME. Intravesically administered antisense oligonucleotides targeting heat-shock protein-27 inhibit the growth of non-muscle-invasive bladder cancer. BJU Int. 2008; 102: 610-616.

[5] Tan ML, Dunstan DE, Friedhuber AM, Choong PF, Dass CR. A nanoparticulate system that enhances the efficacy of the tumoricide Dz13 when administered proximal to the lesion site. J Control Release. 2010;

144: 196-202.

[6] Ballarín-González B, Howard KA. Polycation-based nanoparticle delivery of RNAi therapeutics: adverse effects and solutions. Adv Drug Deliv Rev. 2012; 64: 1717-1729.

[7] Zhao W, Cui CH, Bose S, Guo D, Shen C, Wong WP. Bioinspired multivalent DNA network for capture and release of cells. Proc Natl Acad Sci U S A. 2012; 109: 19626-19631.

[8] Hamblin GD, Carneiro KM, Fakhoury JF, Bujold KE, Sleiman HF. Rolling circle amplification-templated DNA nanotubes show increased stability and cell penetration ability. J Am Chem Soc. 2012; 134: 2888-2891.

[9] Lee JB, Peng S, Yang D, Roh YH, Funabashi H, Park N. A mechanical metamaterial made from a DNA hydrogel. Nat Nanotechnol. 2012; 7: 816-820.

[10] Lee JB, Hong J, Bonner DK, Poon Z, Hammond PT. Self-assembled RNA interference microsponges for efficient siRNA delivery. Nature Mater. 2012; 11: 316-322.

[11] Zhang Z, Ali MM, Eckert MA, Kang DK, Chen YY, Sender LS. A polyvalent aptamer system for targeted drug delivery. Biomaterials. 2013; 34: 9728-9735.

[12] Zöller M. CD44: can a cancer-initiating cell profit from an abundantly expressed molecule. Nature Rev Cancer. 2011; 11: 254-267.

[13] Elahy M, Dass CR. Dz13: c-Jun downregulation and tumour cell death. Chem Biol Drug Des. 2011; 78: 909-912.

[14] Baylot V, Andrieu C, Katsogiannou M, Taieb D, Garcia S, Giusiano S. OGX-427 inhibits tumor progression and enhances gemcitabine chemotherapy in pancreatic cancer. Cell Death Dis. 2011; 2, e221.

[15] Jarvius J, Melin J, Go¨ransson J, Stenberg J, Fredriksson S, Gonzalez-Rey C, Bertilsson S. Digital quantification using amplified single molecule detection. Nature Methods. 2006; 3:725-727.

[16] Huang S, Chen Y. Polymeric sequence probe for single DNA detection. Anal Chem. 2011; 83: 7250-7254.

[17] Mok H, Park JW, Park TG. Antisense oligodeoxynucleotide-conjugated

hyaluronic acid/protamine nanocomplexes for intracellular gene inhibition. Bioconjug Chem. 2007; 18: 1483-1489.

[18] Yao L, Wang Y, Xu S. Label-free microRNA detection based on exchange-induced remnant magnetization. Chem Commun. 2013; 49: 5183-5185.

[19] Shinoda C, Maruyama M, Fujishita T, Dohkan J, Oda H, Shinoda K. Doxorubicin induces expression of multidrug resistance-associated protein 1 in human small cell lung cancer cell lines by the c-jun N-terminal kinase pathway. Int J Cancer. 2005;117:21-31.

[20] Hansen RK, Parra I, Lemieux P, Oesterreich S, Hilsenbeck SG, Fuqua SA. Hsp27 overexpression inhibits doxorubicin-induced apoptosis in human breast cancer cells. Breast Cancer Res Treat. 1999; 56: 187–196.

[21] Dass CR, Khachigian LM, Choong PF. c-Jun knockdown sensitizes osteosarcoma to doxorubicin. Mol Cancer Ther. 2008; 7: 1909-1912.

[22] Díaz-Chávez J, Fonseca-Sánchez MA, Arechaga-Ocampo E, Flores-Pérez A, Palacios-Rodríguez Y, Domínguez-Gómez G. Proteomic profiling reveals that resveratrol inhibits HSP27 expression and sensitizes breast cancer cells to doxorubicin therapy. PLoS One. 2013; 8: e64378.

[23] Li S-D, Howell SB. CD44-targeted microparticles for delivery of cisplatin to peritoneal metastases. Mol Pharm. 2010; 7:280-290.

Chapter IV

Photoresponsive boron nitride nanosheets modified with polyphenol and iron complexes

1. Introduction

Two dimensional nanomaterials have been considered as a next generation material recently because of their large surface area and high chemical stability compared to particulate nanomaterials [1,2]. Graphene nanosheet is a representative example which has been extensively investigated as 2D nanomaterials in various pharmaceutical applications because of their photothermal activity, and high drug loading capacity. Boron nitride nanosheets (BNNSs), which is called as ‘white graphene’, is a few layer of hexagonal boron nitride (hBN) which has been also investigated as a promising nanomaterial due to their high chemical stability and thermal conductivity [3,4]. Although BNNSs are novel 2D nanomaterials like graphene, few biomedical applications of BNNSs have been reported since they are not easy to be synthesized, limited water dispersity [5], and have no photothermal activity compared to graphene nanosheets.

Photothermal therapy (PTT) is a treatment to eradicate solid tumors using photoresponsive agents which convert absorbed light into heat [6]. PTT has emerged as an attractive cancer therapy because it is less invasive treatment compared to surgery and avoids side effects and multidrug resistance caused by

chemotherapy [7,8]. Gold nanoparticles [9], carbon nanotube [10,11], and graphene [10] are well-known photoresponsive agents for PTT until now. Because PTT has been noted for its potential as a promising alternative therapy, many researchers have been trying to develop photothermal-stable, biocompatible, highly photothermal conversion efficient, and easily prepared photothermal agents.

Tannic acid (TA) is a polyphenol exists in nature widely. TA is composed of decagalloyl glucose and TA coordinates with Fe^{3+} ion to form a stable complex because galloyl groups in TA share electrons with Fe^{3+} ion [12]. TA and iron complexation has been suggested as easy, low cost, and environment-friendly coating technique recently [13,14].

Here, BNNS coated with TA and iron film was developed as a novel PTT agent. As far as we know, polyphenol and metal complexes have not been reported as a PTT agent yet. We expect TA and iron complex coated BNNS could be safe PTT agent rather than conventional PTT agents since both TA and iron are exist in nature and BNNS is known as a chemically inert material. TA and iron complex can coat versatile materials like BNNS which originally has no photothermal activity, thus it could be a platform technology to prepare various PTT agents.

2. Materials and methods

2.1. Preparation of nanosheets

First, boron nitride nanosheets (BNNS) were prepared by exfoliation of hBN microsized particles followed by previously reported methods with slight modification [15,16]. In brief, hBN powder (1 g, Sigma-Aldrich, St. Louis, MO, USA) was sonicated at 40 mL of triple-distilled water (TDW) for 48 h. Resulting suspension was then centrifuged at 3,134 × g for 50 min to remove aggregated materials. The supernatant was further sonicated for 12 h and centrifuged at 3,134 × g for 50 min. The translucent supernatant containing exfoliated BNNS was then harvested.

In some experiments, for comparison of safety with plain BNNS, plain graphene oxide nanosheets were prepared using a modified Hummer's method [17]. In brief, graphite powder (0.5 g; Sigma-Aldrich) was added to cold H_2SO_4 (23 mL) then $KMnO_4$ (3 g; Sigma-Aldrich) and $NaNO_3$ (0.5 g; Sigma-Aldrich) were slowly added. The mixture was stirred on ice first and at 35 ℃ for an additional 1 h. Subsequently, the mixture was incubated at 90 ℃ for 1h after adding TDW (46 mL). To finalize the reaction, 30 % HCl (10 mL) and TDW (140 mL) were added.

The resulting product was purified by three-time repeated centrifugation after washing with 5% HCl and TDW. The product is called GO and 2 h sonication exfoliated GO layers to GO nanosheets. Unexfoliated GO layers were removed by centrifugation at 1600 ×g for 10 min. The GO nanosheets-containing supernatant was filtered through 0.2 μm polycarbonate membrane filters (Millipore Corp., Billerica, MA, USA) using an extruder (Northern Lipid, British Columbia, Canada).

To prepare TA and iron-coated BNNS (TA-Fe/BNNS), BNNS suspension (0.5 mg/mL) was added with tannic acid (2 mg/mL) and $FeCl_3$ (0.06 mg/mL). To prepare TA-coated BNNS (TA/BNNS), BNNS suspension (0.5 mg/mL) was added with TA (2 mg/mL). To prepare iron-coated BNNS (Fe/BNNS), BNNS suspension (0.5 mg/mL) was added with $FeCl_3$ (0.06 mg/mL). In all cases, the mixture was vigorously vortexed for 1 min, and centrifuged at 5,433 × g for 2 min. The pellets were resuspended in 0.25 mL of TDW, sonicated for 30 min, and stored at room temperature until use.

.

2.2. Characterization studies of surface-modified BNNS

The morphologies of plain and surface-modified BNNS were examined by

transmission electron microscopy (TEM, JEM1010, JEOL Ltd., Tokyo, Japan). The size and the zeta potentials of plain BNNS, TA/BNNS, Fe/BNNS, and TA-Fe/BNNS were analyzed using an ELSZ-1000 instrument (Photal, Osaka, Japan). The samples were diluted in TDW, and the zeta potential values were determined using laser Doppler microelectrophoresis at an angle of 22°. Atomic force microscopy (AFM) was performed to measure the thickness of the surface-modified BNNS. Pre-cut silicon wafer sections (5 mm x 5 mm, Virginia Semiconductor Inc., anFredericksburg, Virginia, USA) were incubated in the BNNS containing solution (50 μg/mL) for 30 min and completely dried for 2 days. The topography, thickness, and lateral sizes were measured using AFM (XE-100; Park Systems, Suwon, Republic of Korea) in the non-contact mode.

The absorption spectra of various BNNS were recorded over the range of 400-900 nm at the concentration of 0.5 mg nanosheets/mL using a UV-vis spectrophotometer (UV-3100, Shimadzu Corp, Tokyo, Japan). For Raman spectroscopy measurements, surface-modified BNNS samples were prepared to a final concentration of 2.0 mg nanosheets/mL and Raman spectra were monitored with a Horiba Jobin-Yvon LabRam Aramis spectrometer (Horiba Scientific, Boston, MA, USA). The Raman system used a HeNe diode laser having an

excitation source at a wavelength of 785 nm and power of 4 mW.

Energy dispersive spectroscopy (EDS) was conducted to examine elemental composition of the surface-modified BNNSs using JEM-2100F TEM with field emission power of 120 kV (JOEL Ltd., Japan). Thermo-gravimetric analysis (TGA) was performed from room temperature to 700 ^{o}C to determine TA-Fe content in TA-Fe/BNNS sample using a Q 5000 IR TGA instrument (TA instrument, USA) at a heating rate of 10 ^{o}C/min under an air flow of 20 mL/min. The stability of BNNS and surface-modified BNNS was investigated by storing the suspensions of various BNNS preparations in phosphate-buffered saline (PBS; 50 mM, pH 7.4) at room temperature. The occurrence of precipitation was monitored using a digital camera (Canon PC 1089, Canon Inc., Tokyo, Japan).

2.3. Photoresponsiveness study of surface-modified BNNS

The photothermal properties of various BNNS were measured using an IR thermal imaging system after irradiation of each sample using near-infrared (NIR) laser. The suspensions of BNNS (1.6 mg/mL) in plain or surface-modified forms were irradiated using an 808 nm NIR laser (PSU-FC, ChangChun New Industries

Optoelectronics Tech. Co., LTD, Changchun, China) with an output power of 1.5 W. In the case of TA-Fe/BNNS, the photothermal property was examined at various concentrations ranging from 0.1 to 1.6 mg/mL. The temperature and photothermal images of the suspensions with laser irradiation time were recorded using an IR thermal imaging system (FLIR T420; FLIR Systems Inc., Danderyd, Sweden). Thermal stability of TA-Fe/BNNS was evaluated by measuring temperature changes followed by 3 times of irradiation cycles, laser-on for 10 min and laser-off for 10 min, using IR thermal imaging system and FLIR QuickReport 1.2 software.

2.4. In vitro cellular temperature measurement

KB cells were seeded onto 12-well plates at a density of 1×10^5 cells/well. Next day, the cells were treated with 0.04 mg/mL of plain or surface-modified BNNS. After incubating for 4h, the cells were detached and the cell pellets were irradiated for 7 min using an 808 nm continuous NIR laser at an output power of 1.5 W. The temperature changes were then recorded using an IR thermal imaging system (FLIR T420).

2.5. Cell viability assay

The viability changes of BNNS-treated cells upon NIR irradiation was quantified by fluorescence staining of the live cells (Invitrogen Corp., Carlsbad, CA, USA) or using 3-(4, 5-dimethylthiazol-2-yl)-2, 5-diphenyltetrazolium bromide (MTT, Sigma-Aldrich) assay. KB cells were seeded onto 12-well plates at a density of 1×10^5 cells/well. Next day, the cells were treated with plain or surface-modified BNNS at a concentration of 0.04 mg/mL for 2h. After washing the cells, the cell pellets were irradiated using an 808 nm NIR laser at an output power of 1.5 W for 7 min and cultured for 24h. Live cells were fluorescently stained by adding 2 μM of calcein and the images were obtained using fluorescence microscopy (Leica DM IL, USA). MTT assay was performed by adding 0.5 mM of MTT solution and the absorbance was measured at 570 nm using a microplate reader (Tecan Group Ltd., Seestrasse, Mannedorf, Switzerland). The values were expressed as a percentage of cell viability of control cells.

2.6. In vivo safety study

Five-week-old female Balb/c mice, supplied from Daehanbiolink Inc. (Eumseong,

Chungcheongbuk-do, Republic of Korea), were used for acute toxicity tests. All animals were maintained under standard pathogen-free conditions and used in accordance with the Guidelines for the Care and Use of Laboratory Animals of the Institute of Laboratory Animal Resources, Seoul National University (approved animal experimental protocol number SNU-150609-2). GO, BNNS, or TA-Fe/BNNS nanosheets were dispersed at isotonic 5% glucose, and intravenously administered to Balb/c mice at various doses. The survival of mice was monitored until 40 days post-injection (n=5/per group).

2.7. In vivo photothermal imaging

To determine the in vivo photothermal effects of various BNNS, 3×10^6 KB cells were subcutaneously injected at the dorsal left side of five-week-old female Balb/c athymic nude mice. When the tumor volumes reached 70 mm^3, plain or surface-modified BNNS was administrated to the anesthetized mice at a dose of 10 mg/kg intratumorally. The tumor sites were then irradiated with an 808 nm NIR laser at an output power of 1.5 W for 10 min. The temperature changes at the irradiated tumor sites were recorded using a real-time infrared thermal

imaging system (FLIR T420, FLIR Systems Inc., Danderyd, Sweden). The optical images were obtained using a digital camera (Canon PC 1089, Canon Inc., Tokyo, Japan).

2.8. In vivo photothermal tumor ablation study

The in vivo photothermal anticancer effect of various BNNS was evaluated using KB tumor-bearing Balb/c nude mice. KB cells (3×10^6) were subcutaneously injected at the dorsal left side of five-week-old female Balb/c athymic nude mice. When the tumor volume reached 70 mm^3, plain or surface-modified BNNS was injected at a dose of 10 mg/kg to tumor tissues of the anesthetized mice. The tumor sites were then left unirradiated or irradiated with an 808 nm NIR laser at an output power of 1.5 W for 10 min. The tumor sizes were measured using a slide caliper and the tumor volume was calculated according to the equation 0.5 × (largest diameter) × (smallest diameter)^2. The day after administration, tumor tissues were extracted and immunostained with an anti-proliferating cell nuclear antigen (PCNA) antibody and assayed by terminal deoxynucleotidyl transferase dUTP nick-end labeling (TUNEL).

2.9. Statistics

One way ANOVA and Student-Newman-Keuls post-hoc test were used for statistical evaluation. All statistical analyses were two-sided, and performed using SigmaStat software (version 3.5; Systat Software, Richmond, CA, USA). A p-value less than 0.05 was considered significant.

3. Results

3.1. Characterization of the surface-modified BNNS

The lateral sizes of nanosheets were affected by the material types (Fig. IV-2A). Except Fe/BNNS, TA/BNNS and TA-Fe/BNNS showed the mean sizes similar to plain BNNS. The mean size of TA/BNNS, TA-Fe/BNNS was 108.2 ± 13.9 nm, and 106.3 ± 10.6 nm, respectively. However, Fe/BNNS showed larger sizes than plain BNNS, showing 287.6 ± 64.5 nm. Zeta potentials varied according to the surface modification (Fig. IV-2B). Fe/BNNS showed positive zeta potential, but TA-Fe/BNNS showed negative zeta potential.

Surface modification did not affect the morphology of BNNS. TEM imaging revealed that the morphologies of TA/BNNS (Fig. IV-2D), Fe/BNNS (Fig. IV-2E), and TA-Fe/BNNS (Fig. IV-2F) were similar to that of plain BNNS (Fig. IV-2C). Thickness of several BNNSs was measured by AFM (Fig. IV-2G-J). The plain BNNS showed 7.24 ± 0.79 nm as its thickness and introduction of TA or Fe to BNNS did not affect its thickness which was 7.06 ± 0.36 nm and 8.58 ± 1.51 nm. However, TA-Fe coating increased thickness of BNNS up to 17.92 ± 2.65 nm.

UV-vis spectra of TA-Fe/BNNS revealed greater absorption over all wavelength tested compared with those of plain BNNS, TA/BNNS, and Fe/BNNS (Fig.IV-3A). Several BNNSs were analyzed by Raman spectroscopy and TA-Fe/BNNS showed characteristic peaks of both BNNS and TA-Fe complex (Fig. 3B).

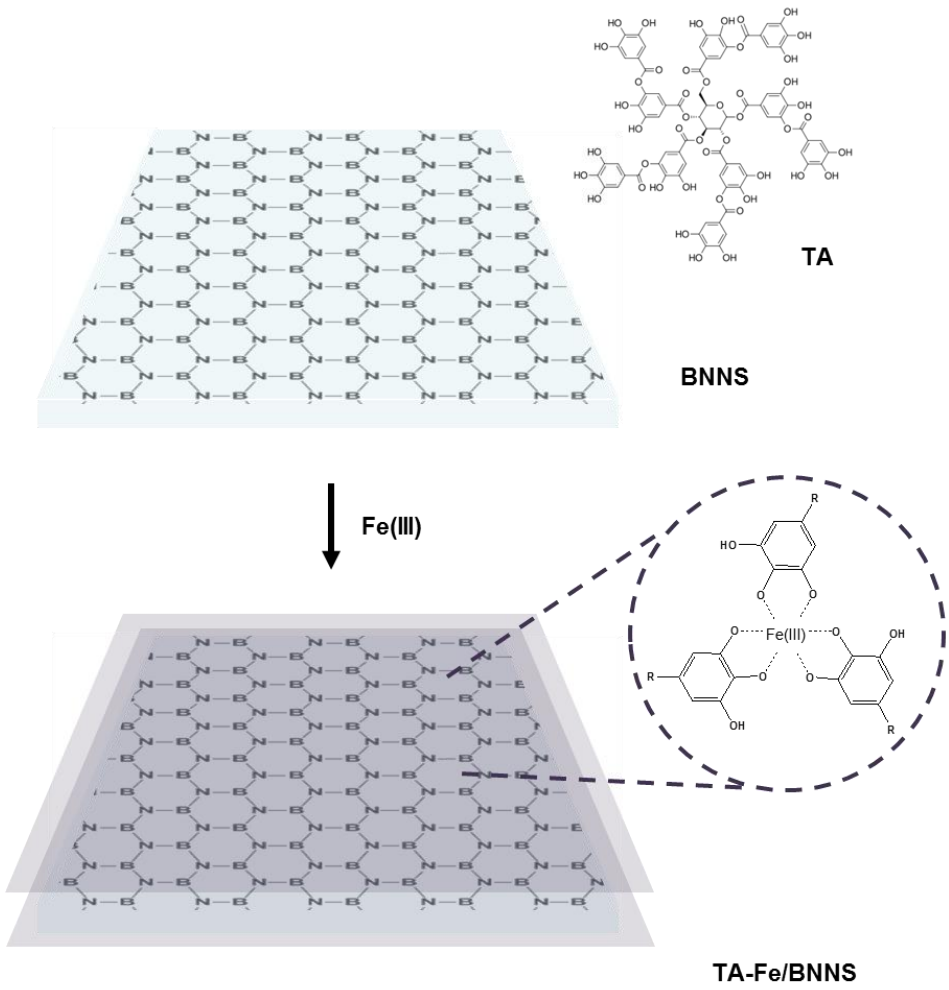

Fig. IV-1. Schematic illustration of TA-Fe/BNNS preparation.

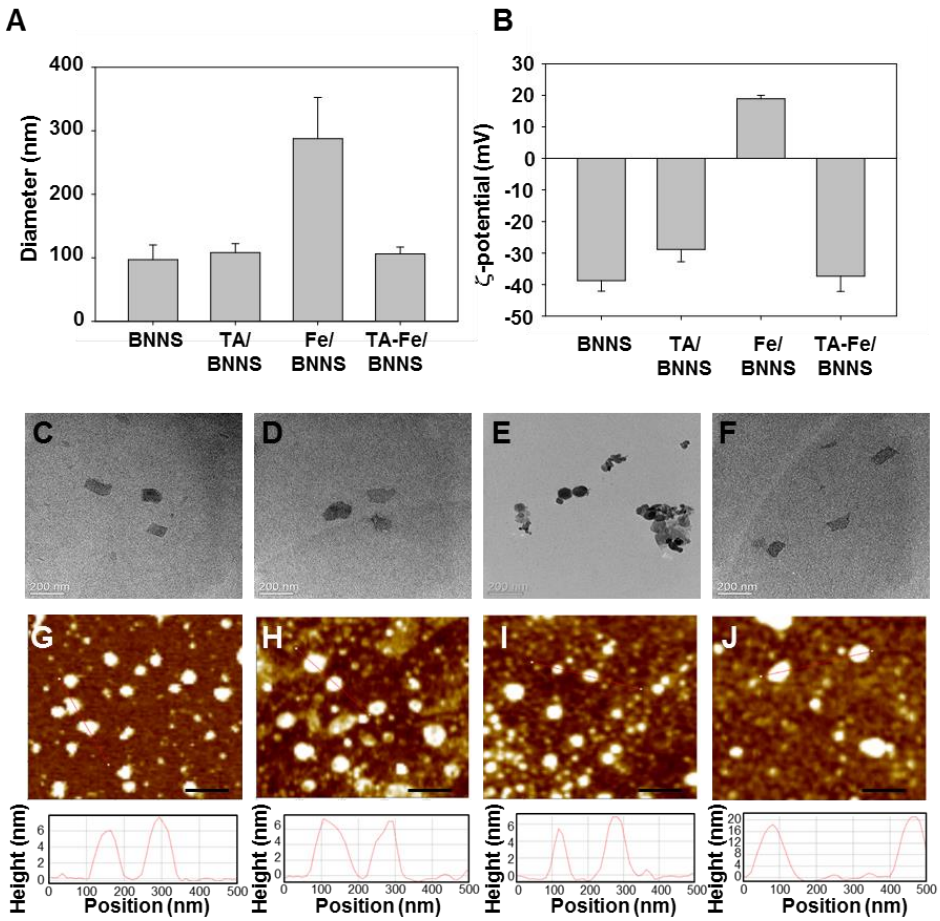

Fig. IV-2. Physicochemical properties of surface-modified BNNSs.

The size (A) and the zeta potential (B) of the surface modified BNNSs were evaluated using the laser Doppler microelectrophoresis. TEM images of BNNS (C), TA/BNNS (D), Fe/BNNS (E) and TA-Fe/BNNS (F) are presented (scale bars indicate 200 nm). AFM images and corresponding height profiles of BNNS (G), TA/BNNS (H), Fe/BNNS (I) and TA-Fe/BNNS (J) are presented (scale bar=200 nm).

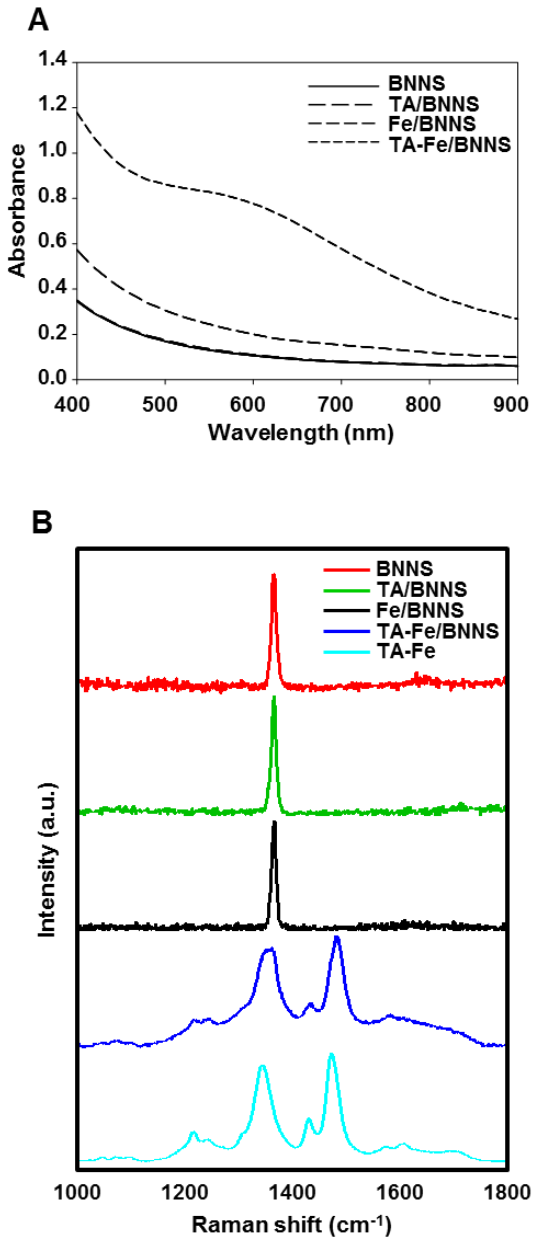

Fig. IV-3. Spectroscopic characteristics of the surface-modified BNNSs.

(A) UV-vis spectra at a range of 400 nm to 900 nm were measured. (B) Raman spectra of the surface modified BNNSs and TA-Fe complex.

3.2. Surface loading amount and stability

Content of surface-modified BNNSs was analyzed by EDS and TGA analysis. Each element of TA-Fe/BNNS was observed and quantified by EDS mapping (Fig. IV-4A, IV-4B). TA-Fe/BNNS showed uniform distribution of boron, nitrogen, oxygen and iron (Fig. IV-4A). Amount of oxygen which is component of TA and iron increased compared to plain BNNSs. Moreover, the loading amounts of TA and Fe on the surfaces of BNNS were determined by differential thermal stability of each component (Fig. IV-4C, IV-4D). After heating TA-Fe/BNNS at 700 ^{o}C, the weight decreased to 67.0 ± 4.6 % of the original value. Heating of plain BNNS at 700 ^{o}C did not change the weight. Heating of TA/BNNS and Fe/BNNS showed the decrease of weight to 79.5 ± 5.8 % and 91.2 ± 2.0 % of original weight, respectively (Fig. IV-4C).

TA-Fe/BNNS showed greater stability in PBS than other types of BNNS. Plain BNNS, TA-BNNS, and Fe-BNNS precipitated within 4 h after dispersion in PBS. In contrast, TA-Fe/BNNS showed no precipitation in PBS after 48 h of incubation (Fig. IV-5).

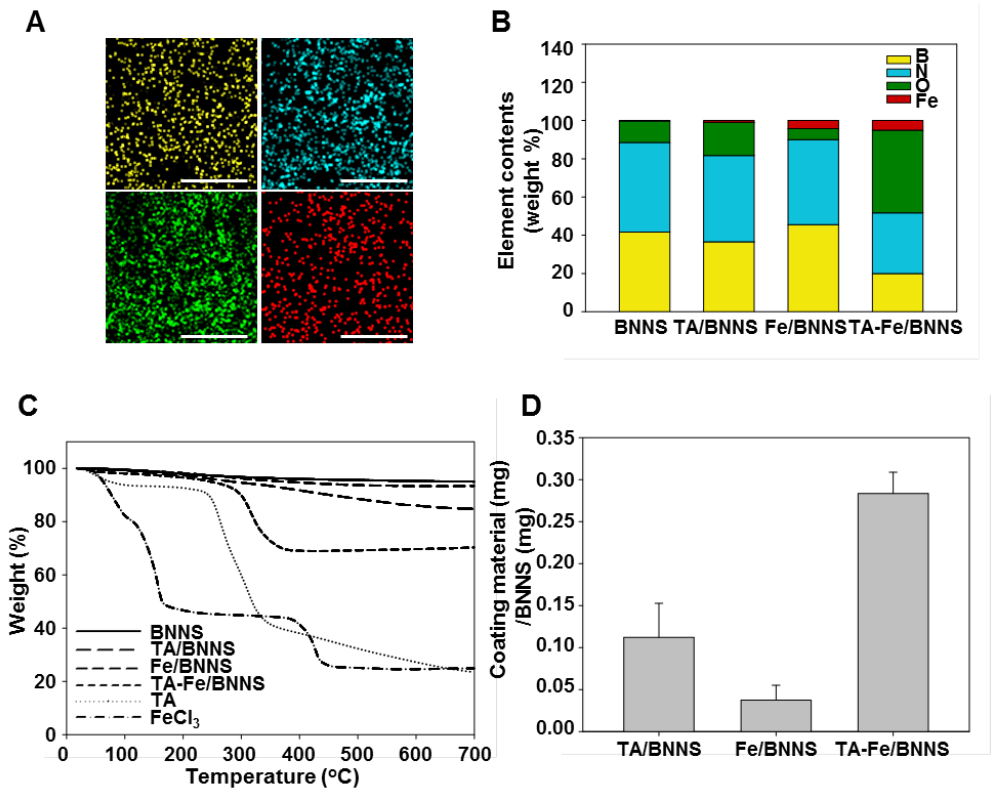

Fig. IV-4. Content analysis of surface-modified BNNSs.

Element mapping images of TA-Fe modified BNNS. EDS maps (A) of boron (yellow), nitrogen (sky blue), oxygen (green) and iron (red) illustrate localization of each element verifying co-existence of all components. (B) Element amount in surface modified BNNSs were quantified. (C) TGA curves were obtained from room temperature to 700 ^{o}C. (D) Content amount on BNNS were quantified based on TGA analysis.

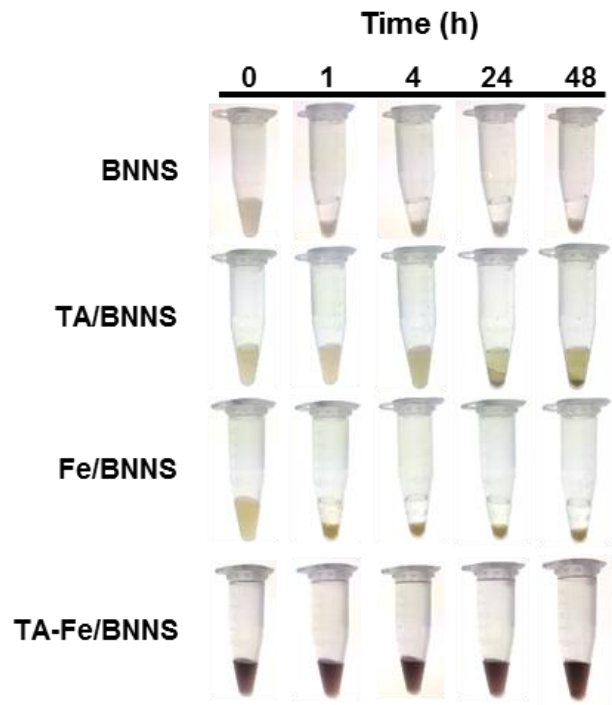

Fig. IV-5. Stability of surface-modified BNNSs in PBS.

The stability of BNNS, TA/BNNS, Fe/BNNS and TA-Fe/BNNS in PBS was monitored upto 48 h at room temperature by digital camera.

3.3. In vitro photothermal effects of TA-Fe/BNNS

BNNS could be photoresponsive depending on the type of materials on their surfaces. Upon irradiation with 808 nm laser, plain BNNS, TA/BNNS, and Fe/BNNS did not show temperature changes (Fig. IV-6A). In contrast, TA-Fe/BNNS showed gradual temperature changes upon irradiation with 808 nm laser (Fig. IV-6B). Moreover, the temperature changes were dependent on the concentrations of TA-Fe/BNNS (Fig. IV-7A). The highest temperature of 64.5 ± 2.2 ℃ was observed after irradiation of TA-Fe/BNNS at the concentration of 1.6 mg/mL (Fig. IV-7B). TA-Fe/BNNS at the concentrations higher than 0.4 mg/mL resulted in the temperature increase higher than 50 ℃. Furthermore, the repeated cyclic irradiation was capable of increasing the temperature in pulsatile manner. The 3 cycles of 10 min NIR irradiation of TA-Fe/BNNS produced the similar increase of temperatures (Fig. IV-7C).

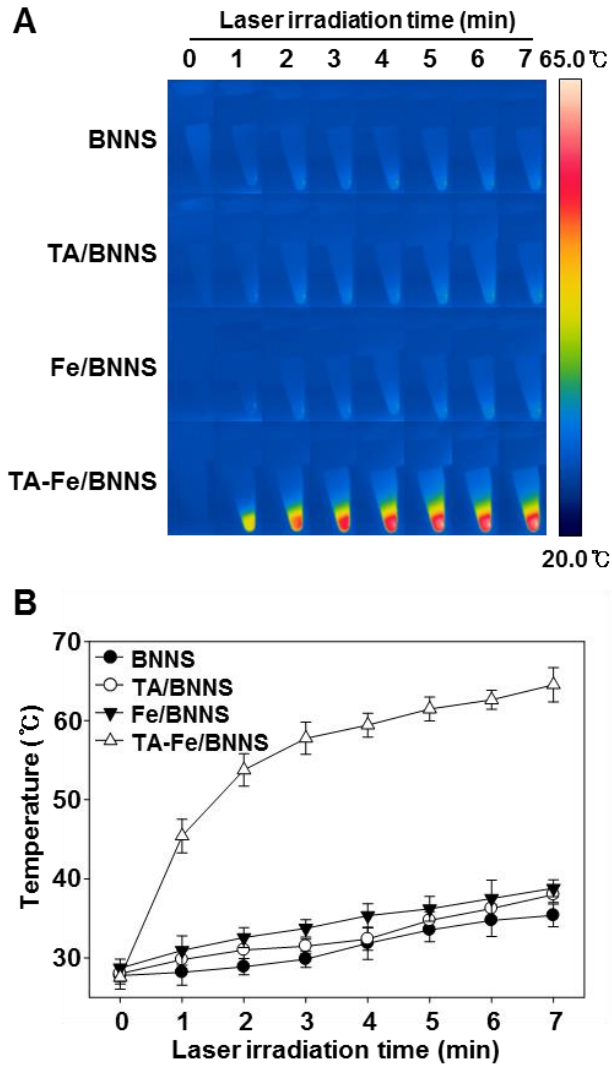

Fig. IV-6. Photothermal activity of surface-modified BNNSs.

Thermal images (A) and temperature changes (B) of various BNNSs dispersions in TDW at the concentraion of 1.6 mg nanosheets/mL after NIR laser irradiation were monitored every 1 min using IR thermal imaging system and FLIR QuickReport 1.2 software.

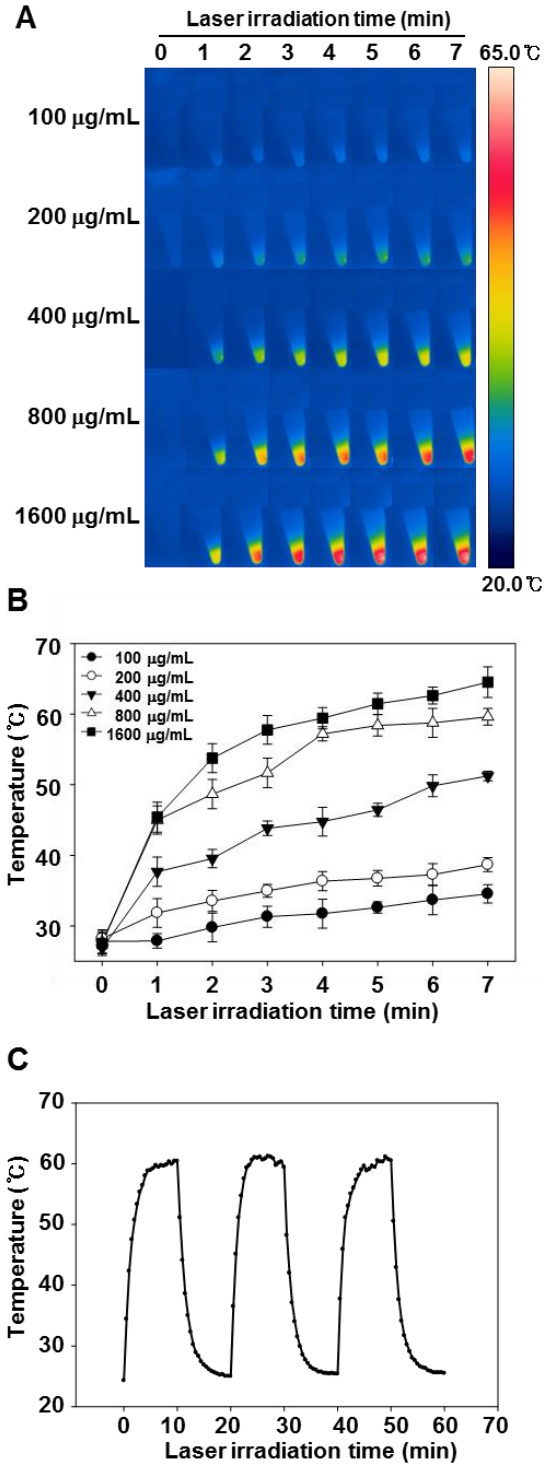

- continued next page –

Fig. IV-7. Concentration dependence of photothermal activity of TA-Fe/BNNS and thermal stability of TA-Fe/BNNS.

Thermal images (A) and temperature changes (B) of TA-Fe/BNNSs dispersions in TDW at the concentraion from 0.1 to 1.6 mg nanosheets/mL followed by NIR laser irradiation were recorded every 1 min. (C) The temperaure changes were monitored with 3 cycle of NIR laser irradiation on/off.

3.4. In vitro photothermal anticancer activity of TA-Fe/BNNS

Consistent with photothermal capacities of variously surface-modified BNNS (Fig. IV-6), NIR laser irradiation produced photothermal effects only in TA-Fe/BNNS-treated cells. Upon NIR irradiation, negligible thermal changes were observed for the cells treated with plain BNNS, TA/BNNS, or Fe/BNNS (Fig. IV-8). However, the cells treated with TA-Fe/BNNS showed the increase of temperature upto 46.9 ± 1.0 ℃ after 7 min of irradiation (Fig. IV-8B).

The photoresponsive anticancer effects were observed in TA-Fe/BNNS, but not in other types of BNNS (Fig. IV-9). Plain BNNS, TA/BNNNS, Fe/BNNS did not show significant killing of KB cells upon NIR irradiation. Unlike these, TA-Fe/BNNS exerted significant killing of KB cells upon irradiation, showing 27.0 ± 9.0 % of viability (Fig. IV-9B). The live cell staining showed that the population of live cells were similar among the three groups treated with plain BNNS, TA/BNNS, and Fe/BNNS, but lowest at the group treated with TA-Fe/BNNS (Fig. IV-9B).

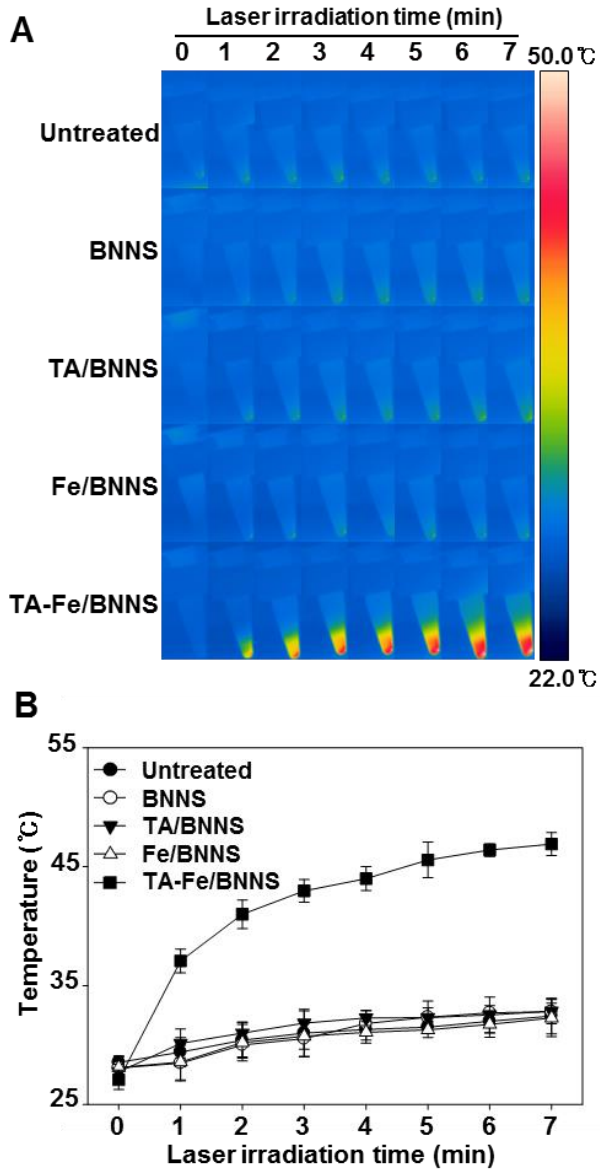

Fig. IV-8. Photothermal activity of various BNNSs after cell treatment.

Thermal images (A) and temperature changes (B) of KB cell pellets treated with BNNS, TA/BNNS, Fe/BNNS, or TA-Fe/BNNS followed by NIR laser irradiation were recorded every 1 min.

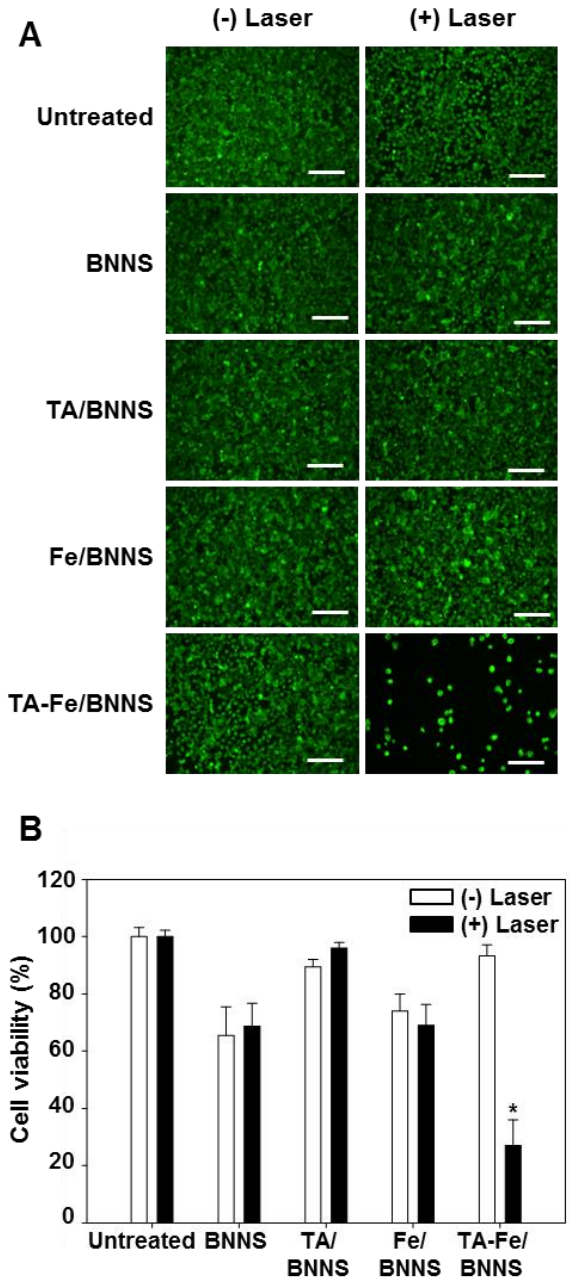

- continued next page -

Fig. IV-9. In vitro anticancer effects of surface-modified BNNSs.

(A) KB cells were treated with BNNS, TA/BNNS, Fe/BNNS, or TA-Fe/BNNS for 2 h. After media replacement, the cell pelletes were irradiated with 808 nm lser for 7 min. After additional 24 h incubation, the live cell population was stained with calcein-AM and observed by fluorescence microscopy. Scale bar: 250 μm. (B) The viability of KB cells was determined by MTT assay. Data are presented as means ± SE (n = 4). (*$p < 0.05$ compared to other groups; ANOVA and Student-Newman-Keuls test).

3.5. In vivo safety of nanosheets

The in vivo safety of nanosheets depended on the type and surface modifications. The safety of TA-Fe/BNNS was compared with those of plain BNNS and plain GO, one of widely studied nanosheets. The survival of mice after single intravenous administration showed that plain BNNS and TA-Fe/BNNS were less toxic than plain GO (Fig. IV-10). The survival of intravenously administered GO nanosheets was 20 % at a dose of 20 mg/kg. No survival of GO-administered mice was observed at doses higher than 60 mg/kg. In contrast, the survival rate of mice administrated with BNNS or TA-Fe/BNNS was 100 % at a dose of up to 60 mg/kg. The mice treated with plain BNNS or TA-Fe/BNNS survived until 40 days after administration.

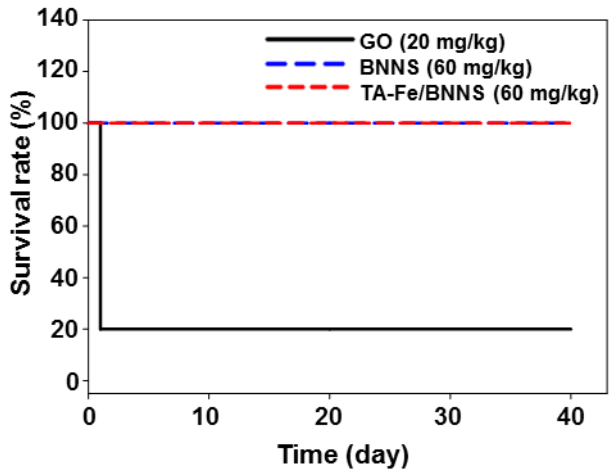

Fig. IV-10. In vivo safety of GO, BNNS, and TA-Fe/BNNS.

Various nanoheets were intraveneously injected to Balb/c mice at a dose of 20 mg/kg, 40 mg/kg, and 60 mg/kg (n=5). The survival rate of the mice was maintained upto 40 days after administration.

3.6. In vivo photothermal antitumor effect of TA-Fe/BNNS

The photothermal property was provided by TA-Fe/BNNS, but not by other groups (Fig.IV-6). Upon NIR irradiation, mice treated with plain BNNS, TA/BNNS, or Fe/BNNS showed similar temperature to untreated mice (Fig. IV-11). Mice treated with TA-Fe/BNNS provided substantial increase upon irradiation, showing the increase of temperature at tumor tissues upto 57.2 ± 0.7℃ (Fig. IV-11B)

Upon NIR irradiation, the photothermal antitumor effects were notable only in the mice treated with TA-Fe/BNNS, but not in the mice treated with other nanosheets (Fig. IV-12). In the absence of NIR irradiation, there were no significant differences among the groups (Fig. IV-12). However, the irradiation made differences among the groups. One day after laser irradiation, the formation of black scabs was observed at the tumor sites of mice treated with TA-Fe/BNNS (Fig.IV-12A). On day 10 after TA-Fe/BNNS treatment, the black scabs were detached from the tumor sites, and the tumor ablation was observed.

Immunohistochemistry showed that the cell proliferation and apoptosis were related to the tumor ablation of mice treated with TA-Fe/BNNS, and NIR-

irradiated (Fig. IV-13). The smallest population of PCNA-positive cells in tumor tissues was observed in TA-Fe/BNNS-treated group (Fig. IV-13C). Similarly, smallest number of apoptotic cells were observed in tumor tissues treated with TA-Fe/BNNS and NIR-irradiated (Fig. IV-13D).

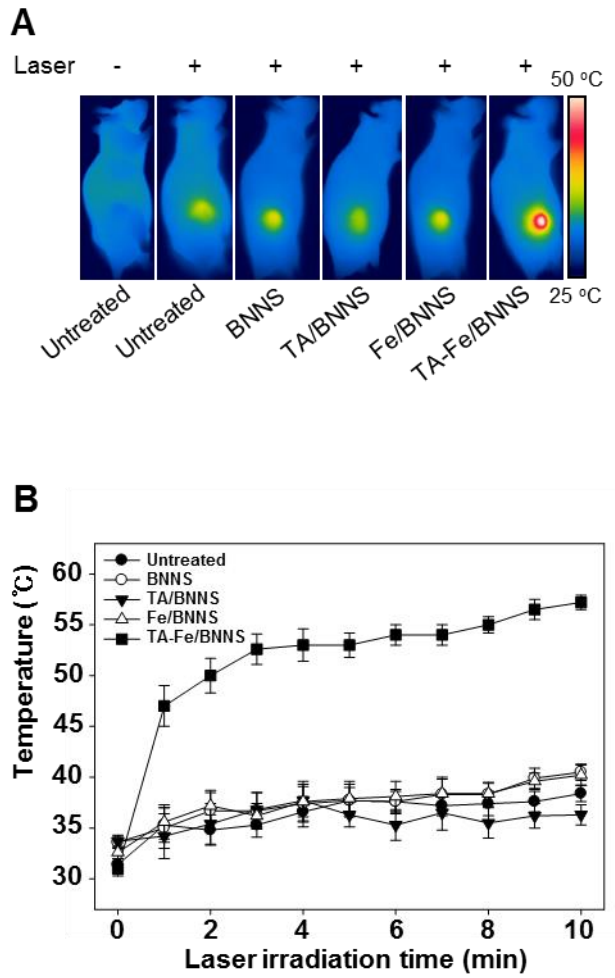

Fig. IV-11. In vivo photothermal activity of surface-modified BNNSs.

Various BNNSs were intratumorally administrated to KB-bearing mice at a BNNS dose of 10 mg/kg. Immediately, 808 nm laser was applied to the tumor site for 10 min. The thermal images (A) and temperature increase (B) were monitored every 1 min.

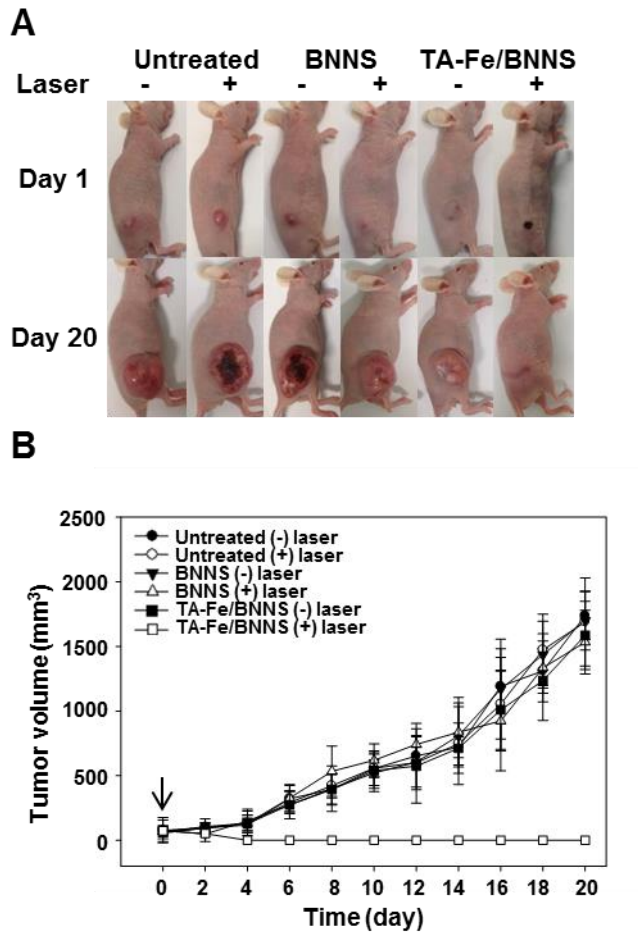

Fig. IV-12. In vivo photothermal anticaner effect of TA-Fe/BNNSs.

BNNS or TA-Fe/BNNS was intratumorally administrated to KB-bearing mice at BNNS dose of 10 mg/kg with NIR laser irradiation for 10 min. (A) The optical images of tumor xenografted mice on the next day after administration (day 1) and on day 20. (B) The tumor volumes were measured every 2 days using a caliper.

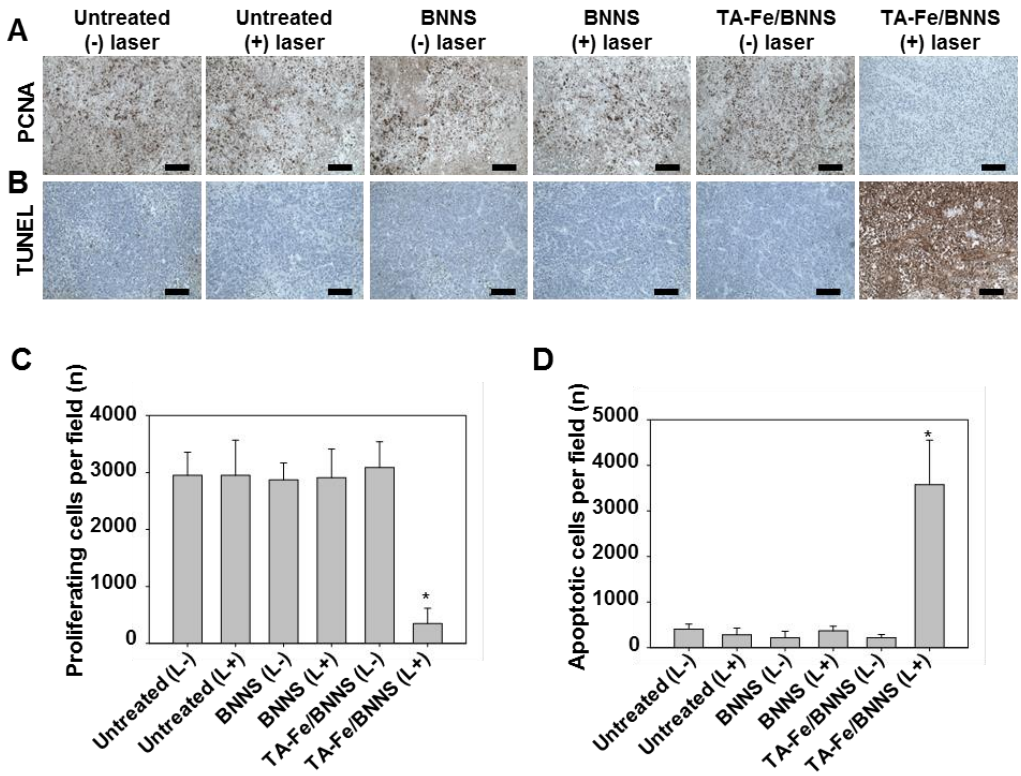

Fig. IV-13. Immunohistochemistry of BNNS treated tumor tissues.

Tumor tissues excised on day 8 after tumor inoculation were analyzed by immunostaining for PCNA (A) and by performing TUNEL assays (B). The numbers of PCNA-immunostained proliferating cells (C) and TUNEL-labeled apoptotic cells (D) in tumor tissue sections were determined (n = 3; *p < 0.001 compared to other groups; ANOVA and Student-Newman-Keuls test). Scale bar, 100 μm.

4. Discussion

Here, BNNS was demonstrated less toxic than GO, and the surface modification of plain BNNS with TA and Fe could confer photoresponsiveness. Upon NIR irradiation, TA-Fe/BNNS could generate heat, which can be applied to photothermal antitumor activity. The substantial photothermal antitumor effect observed by TA-Fe/BNNS was supported by the lowered cell proliferation and enhanced apoptosis at the tumor tissues compared with other groups.

In this study, TA and Fe were used for surface modification of BNNS. Previously the surfaces of BNNS were modified with chitosan [18], poly(vinyl alcohol) [19,20], or polydopamine [21,22]. Here, TA was initially loaded on the surfaces of BNNS before Fe. TA alone, might be loaded onto BNNS via π–π interactions and Fe ion alone, could interact with BNNS via charge-charge interaction. However, the coating with TA or Fe lone was not sufficient to provide photothermal activity. The modification with both TA and Fe was effective in providing photothermal activity to BNNS. Although more studies would be necessary, there exists a possibility that TA and Fe form complexes to enhance the adsorption onto BNNS nanosheets. It has been reported that TA-Fe complex can coat various nanoparticles via high adsorption property [13].

TA-Fe coating increased the thickness of the BNNS upto 17.92 ± 2.65 nm (Fig. IV-2J). Thickness of BNNS has been reported as around 1 to 10 nm and it depends on the number of layer [15,23,24]. In our observation, thickness of TA-Fe in TA-Fe/BNNS was determined as 10.68 nm. In previous studies, thickness of TA-Fe film was reported as around 3 nm to 20 nm which was affected by iron concentration and number of coating cycle [13,25].

Element analysis was carried out by EDS mapping and amount of TA and Fe was estimated by TGA analysis (Fig. IV-4). Major element of BNNS was boron and nitrogen and oxygen was also detected and oxygen might exist at the edges of the nanosheets [16]. Iron amount in TA-Fe/BNNS was not significantly changed compared to Fe/BNNS but oxygen, which consists of TA, amount in TA-Fe/BNNS significantly increased compared to TA/BNNS (Fig IV-4B). This result is correlated with TGA data (Fig. IV-4D) which means higher amount of TA-Fe complex could coat BNNS rather than TA or Fe alone.

Dispersion stability of nanosheets is crucial for biomedical applications. We observed that TA-Fe/BNNS enhanced dispersion stability in PBS. The precipitation of nanomaterials in aqueous media was previously observed in graphene oxide nanosheets [26], carbon nanotubes [27], and gold nanoparticles

[28]. The dispersion stability of TA-Fe/BNNS might be in part attributed to the presence of galloyl groups on TA, which provide negative zeta potential values to TA-Fe/BNNS and reduced the hydrophobic interaction among the nanosheets in PBS.

Polyphenol has been used as stabilizers with PTT agents such as gold nanoparticles [29] and graphene nanosheets [30], but photothermally active component was not polyphenol in these PTT systems. In this study, plain BNNS without being photoresponsive could convert to be photoresponsive by surface modification with TA-Fe. The photoresponsiveness of TA-Fe/BNNS could be explained in part due to the change in light absorption spectra. It has been reported that light absorption spectrum could be changed after coordination of metal ion and ligands [31]. Galloyl groups in TA donated lone pair electrons and formed coordinate bonds with Fe^{3+} ion by overlapping with d-orbitals of Fe^{3+} ion. Then the d-orbitals split into two energy levels and the chelate complex can absorb light energy as much as the two energy level gap. Even the maximum absorption wavelength of TA-Fe/BNNS was not exactly 808 nm but TA-Fe/BNNS showed the highest light absorption at the NIR region (Fig. IV-2G). The NIR-absorbing property could explain the NIR photoresponsieness of TA-

Fe/BNNS.

In the perspective of photothermal conversion efficiency alone, TA-Fe/BNNS are not efficient compared to graphene nanosheets. At least 0.4 mg/mL of TA-Fe/BNNS was required to increase the temperature upto 50 ^{o}C upon 808 nm laser irradiation (Fig. IV-6B). However, we previously observed that 0.01 mg/mL of pegylated graphene nanosheets was enough to show comparable photothermal activity [10]. The reason why TA-Fe/BNNS has relatively lower photothermal conversion efficiency is considered that low NIR absorption of TA-Fe/BNNS because the maximum wavelength of BNNS/TA-Fe was visible region. Moreover, the coating amount of TA-Fe might be limited and the amount of TA-Fe was calculated as 33.0 ± 4.6 % as weight percentage based on TGA results (Fig. IV-3).

The photothermal effect of TA-Fe/BNNS was greatest in KB cells compared to other groups (Fig. IV-7). Although further study will be required to elucidate the interaction between BNNS and cells, we speculate that BNNS may be taken up by cells via non-specific endocytosis. Non-specific endocytosis has been observed for various nanomaterials [32,33]. It has been reported that graphene oxide nanosheets with size ranging from 100 nm to 200 nm were taken up by cells via clathrin-mediated endocytosis [34]. Although mechanism of cell uptake

of BNNS has not been reported yet, BNNS could be taken up by adsorptive endocytosis.

Both BNNS and TA-Fe/BNNS showed a much higher safety in our in vivo toxicity test compared to GO nanosheets when they were administrated intravenously to Balb/c mice (Fig. IV-9). GO nanosheets may adsorb proteins in vivo via hydrophobic interaction or π–π interaction but little protein may adsorb to BNNS and BNNS/TA-Fe. Biocompatibility of hBN nanomaterials has been investigated recently. Boron nitride nanotube (BNNT) did not induce cytotoxic effect [35]. Polyethyleneimine modified BNNT also did not show significant toxicity in vitro [36]. However, Horváth et al., reported cytotoxicity of BNNT [37]. Until now, there is still remaining controversial debate of toxicity issue of BNNT. In case of BNNS, there is no investigation about its cytotoxicity and in vivo safety yet. We observed that BNNS did not affect cancer cell viability at a concentration of 0.04 mg/mL and provided the survival of mice upto 60 mg/kg of intravenous dose (Fig . IV-8, IV-9).

TA-Fe/BNNS provided photothermal antitumor effect higher than other groups (Fig. IV-11, IV-12). It is considered that BNNS could transfer heat to nearby tissues effectively because of high thermal conductivity of BNNS. And two-

dimensional structure of BNNS which has large surface area is also suitable for high amount of TA-Fe coating.

In conclusion, the surface modification with TA and Fe complex can convert the photoresponsiveness of BNNS. The surfaces of BNNS were conveniently modified with TA and Fe complexes by physical adsorption. TA-Fe/BNNS provided higher in vivo safety than GO nanosheets. The photothermal properties of TA-Fe/BNNS was high enough to provide tumor ablation after NIR irradiation. Results in this study suggest the potential of TA-Fe/BNNS for a new modality of photothermal nanomaterials for noninvasive anticancer therapy.

5. References

[1] Yang G, Zhu C, Du D, Zhu J, Lin Y. Graphene-like two-dimensional layered nanomaterials: applications in biosensors and nanomedicine. Nanoscale 2015;7:14217-31.

[2] Chimene D, Alge DL, Gaharwar AK. Two-dimensional nanomaterials for biomedical applications : emerging trends and future prospects. Adv Mater 2015;27:7261-84.

[3] Li LH, Cervenka J, Watanabe K, Taniquchi T, Chen Y. Strong oxidation resistance of atomically thin boron nitride nanosheets. ACS Nano 2014;8:1457-62.

[4] Ouyang T, Chen Y, Xie Y, Yang K, Bao Z, Zhoug J. Thermal transport in hexagonal boron nitride nanoribbons. Nanotechnology 2010;21:245701.

[5] Golberg D, Bando Y, Huang Y, Terao T, Mitome M, Tang C, Zhi C. Boron nitride nanotubes and nanosheets. ACS Nano 2010;4:2979–93.

[6] Zhang Z, Wang J, Chen C. Near-infrared light-mediated nanoplatforms for cancer thermo-chemotherapy and optical imaging. Adv Mater

2013;25:3869-80.

[7] Jaque D, Martínez Maestro L, del Rosal B, Haro-Gonzalez P, Benayas A, Plaza JL, Martín Rodríguez E, García Solé J. Nanoparticles for photothermal therapies. Nanoscale 2014;6:9494-530.

[8] Lee S-M, Kim HJ, Kim SY, Kwon M-K, Kim S, Cho A, Yun M, Shin J-S, Yoo K-H. Drug-loaded gold plasmonic nanoparticles for treatment of multidrug resistance in cancer. Biomaterials 2014;35:2272-82.

[9] Sun M, Liu F, Zhu Y, Wang W, Hu J, Liu J, Dai Z, Wang K, Wei Y, Bai J, Gao W. Salt-induced aggregation of gold nanoparticles for photoacoustic imaging and photothermal therapy of cancer. Nanoscale 2016;8:4452-7.

[10] Miao W, Shim G, Lee S, Oh Y. Structure-dependent photothermal anticancer effects of carbon-based photoresponsive nanomaterials. Biomaterials 2014;35:4058-65.

[11] Lin Z, Liu Y, Ma X, Hu S, Zhang J, Wu Q, Ye W, Zhu S, Yang D, Qu D, Jiang J. Photothermal ablation of bone metastasis of breast cancer using PEGylated multi-walled carbon nanotubes. Sci Rep 2015;5:11709.

[12] Ross TK, Francis RA. The treatment of rusted steel with mimosa tannin. Corros Sci 1978;18:351–61.

[13] Ejima H, Richardson JJ, Liang K, Best JP, van Koeverden MP, Such GK, Cui J, Caruso F. One-step assembly of coordination complexes for versatile film and particle engineering. Science 2013;341:154-7.

[14] Fan L, Ma Y, Su Y, Zhang R, Liu Y, Zhang Q, Jiang Z. Green coating by coordination of tannic acid and iron ions for antioxidant nanofiltration membranes. RSC Adv 2015;5:107777-84.

[15] Zhi BC, Bando Y, Tang C, Kuwahara TH, Golberg D. Large-scale fabrication of boron nitride nanosheets and their utilization in polymeric composites with improved thermal and mechanical properties. Adv Mater. 2009; 21: 2889-2893.

[16] Lin Y, Williams TV, Xu T-B, Cao W, Elsayed-Ali H, Connel JW. Aqueous dispersions of few-layered and monolayered hexagonal boron nitride nanosheets from sonication-assisted hydrolysis: critical role of water. J Phys Chem C 2011;115:2679-85.

[17] Miao W., Shim G., Kim G., Lee S., Lee H., Kim Y. B., Byun Y., Oh Y. K.

Image-guided synergistic photothermal therapy using photoresponsive imaging agent-loaded graphene-based nanosheets. J Controlled Release 2015;211:28-36.

[18] Kisku SK, Swain SK. Synthesis and characterization of chitosan/boron nitride composites. J Am Ceram Soc 2012;95:2753–7.

[19] Khan U, May P, O'Neill A, Bell AP, Boussac E, Martin A, Semple J, Coleman JN. Polymer reinforcement using liquid-exfoliated boron nitride nanosheets. Nanoscale 2013;5:581-7.

[20] Song W-L, Wang P, Cao L, Anderson A, Meziani MJ, Farr AJ, Sun Y-P. Polymer/boron nitride nanocomposite materials for superior thermal transport performance. Angew Chem 2012;124: 6604 –7.

[21] Roy AK, Park B, Lee KS, Park SY, In I. Boron nitride nanosheets decorated with silver nanoparticles through mussel-inspired chemistry of dopamine. Nanotechnology 2014;25:445603.

[22] Roy AK, Park SY, In I. Mussel-inspired synthesis of boron nitride nanosheet-supported gold nanoparticles and their application for catalytic reduction of 4-nitrophenol. Nanotechnology 2015;26:105601.

[23] Lin Y, Williams TV, Connel JW. Soluble, exfoliated hexagonal boron nitride nanosheets. J Phys Chem Lett 2010;1:277-83.

[24] Wang X, Zhi C, Weng Q, Bando Y, Golberg D. Boron nitride nanosheets: novel syntheses and applications in polymeric composites. J Phys: Conf Ser 2013;471:012003.

[25] Zeng T, Zhang X, Guo Y, Niu H, Cai Y. Enhanced catalytic application of Au@polyphenol-metal nanocomposites synthesized by a facile and green method. J Mater Chem A 2014;2:14807-11.

[26] Xu S-X, Zhang L-L, Zhang H-C, Zeng Y, Shi Z-M, Ni S-J. A salt-assisted graphene oxide aggregation method for the determination of dimethylamine and trimethylamine by ion chromatography with conductivity detection. Anal Methods 2016; 8:1828-35.

[27] Niyogi S, Boukhalfa S, Chikkannanavar SB, McDonald TJ, Heben MJ, Doorn SK. Selective aggregation of single-walled carbon nanotubes via salt addition. J Am Chem Soc 2007;129:1898-9.

[28] Jiao H, Chen J, Li W, Wang F, Zhou H, Li Y, Yu C. Nucleic acid-regulated perylene probe-induced gold nanoparticle aggregation: a new strategy for

colorimetric sensing of alkaline phosphatase activity and inhibitor screening. ACS Appl Mater Interfaces 2014;6:1979−85.

[29] Zhang X-L, Zheng C, Zhang Y, Yang H-H, Liu X, Liu J. One-pot synthesis of gold nanostars using plant polyphenols for cancer photoacoustic imaging and photothermal therapy. J Nanopart Res. 2016; 18: 174

[30] Abdolahad M, Janmaleki M, Mohajerzadeh S, Akhavan O, Abbasi S. Polyphenols attached graphene nanosheets for high efficiency NIR mediated photodestruction of cancer cells. Mater Sci Eng C Mater Biol Appl. 2013; 33: 1498-1505.

[31] Müller F, Hemmerich P, Ehrenberg A. Light absorption of flavosemiquinone metal chelates. Eur J Biochem 1968;5:158-64.

[32] Rejman J, Oberle V, Zuhorn IS, Hoekstra D. Size-dependent internalization of particles via the pathways of clathrin- and caveolae-mediated endocytosis. Biochem J 2004;377:159-69.

[33] Mao Z, Zhou X, Gao C. Influence of structure and properties of colloidal biomaterials on cellular uptake and cell functions. Biomater Sci 2013;1:896-911.

[34] Huang J, Zong C, Shen H, Liu M, Chen B, Ren B, Zhang Z. Mechanism of cellular uptake of graphene oxide studied by surface-enhanced Raman spectroscopy. Small 2012;8:2577-84.

[35] Chen X, Wu P, Rousseas M, Okawa D, Gartner Z, Zettl A, Bertozzi CR. Boron nitride nanotubes are noncytotoxic and can be functionalized for interaction with proteins and cells. J Am Chem Soc 2009;131:890-1.

[36] Ciofani G, Raffa V, Menciassi A, Cuschieri A. Cytocompatibility, interactions, and uptake of polyethyleneimine-coated boron nitride nanotubes by living cells: confirmation of their potential for biomedical applications. Biotechnol Bioeng 2008;101:850-8.

[37] Horváth L, Magrez A, Golberg D, Zhi C, Bando Y, Smajda R, Horváth E, Forró L, Schwaller B. In vitro investigation of the cellular toxicity of boron nitride nanotubes. ACS Nano 2011;5:3800-10.

Chapter V

Gold nanoclusters loaded DNA nanoballs for photothermal anticancer therapy

1. Introduction

Photothermal therapy (PTT) is a therapy using photoresponsive agents which convert absorbed light energy to heat to kill tumor tissues. PTT is relatively less invasive and able to apply specific local area that expect minimal systemic side effect. Moreover, destroy tumor by local heat do not cause multidrug resistance which is one of limitation of chemotherapy [1]. Thus, PTT has been considered as attractive cancer therapy.

Several types of PTT agents have been investigated so far. Gold nanoparticles [2,3], carbon-based nanomaterials including carbon nanotube [4,5] and graphene nanosheet [6,7], organic polymers such as polypyrrole [8-10], polyaniline [11], polydopamine [12], and small NIR dyes like indocyanine green [13-15] have been used as PTT agents. Among them, gold nanomaterials are promising PTT agents because they are known to be biocompatible, high photothermal conversion efficiency, and photothermal stable. However, gold nanoparticles whose size is several dozens or hundreds nanometer could remain in body and accumulate to cause some toxic effect [16,17].

Gold nanoclusters (AuNCs) which are composed several dozens of gold atoms

have been attracted high interest in nanomedicine area because of its ultrasmall size around 3 nm. Small size AuNC could be excreted by kidney and induce low toxicity due to unwanted accumulation [18]. Until now, AuNCs have been widely investigated for biosensor [19-21] and bioimaging [19,22]. However, therapeutic application of AuNCs is at infancy stage.

Rolling circle amplification (RCA) is a technology to produce a single stranded DNA (ssDNA) from a circular DNA template. Using RCA, ssDNA which is complementary sequence repeats of the circular template is generated by enzyme. Because RCA can produce a specific sequence repeats of DNA which is very biocompatible, several approaches have been reported using RCA in biomedical applications. Chemical anticancer drugs [23,24], antibiotics [25], and oligonucleotide [26] have been delivered via DNA nanostructures produced by RCA technology.

AuNCs assembly in RCA product which is a long ssDNA, called DNA nanoball, was developed in this study. It was hypothesized that large amount of AuNCs could gather and located inside of DNA nanoballs. The AuNCs incorporated DNA nanoballs could generate heat followed by irradiation and exerted enough temperature increase to kill cancer cells.

2. Materials and methods

2.1. Preparation of AuNC incorporated DNA nanoballs

Gold incorporated DNA nanoballs were prepared by (1) producing ssDNA by RCA, (2) incubating with Au(III) ion, and (3) reducing gold by dimethylamine borane (DMAB). In the first step, an RCA template for gold loading was circularized via hybridization with primers. In brief, 0.5 μM of 5'-phosphorylated linear ssDNA template and primer (Macrogen Inc., Daejeon, Republic of Korea) were annealed in hybridization buffer (10 mM Tris-HCl, 1 mM EDTA, 100 mM NaCl, pH 8.0) and mixed with T4 DNA ligase (125 units/mL) (Thermo Scientific, Waltham, MA, USA) to close the nick in the circular RCA template. After inactivating T4 DNA ligase by heating to 70 ^{o}C, the circular RCA template (200 μL) was incubated at 30 ^{o}C for 12 h with phi29 DNA polymerase (100 units/mL) (Thermo Scientific) and 2 mM dNTP (Intron Biotechnology Inc., Seoul, Republic of Korea). After heat-inactivating phi29 DNA polymerase at 70 ^{o}C for 10 min, residual dNTPs were removed by centrifugation at 13,000 rpm for 10 min. The resulting pellet of RCA product was resuspended in water, and its concentration was measured using a Nanodrop spectrophotometer (Thermo Scientific). 12 μg of RCA product was incubated in 20 mM phosphate buffer containing 1 mM

magnesium acetate (pH 4.4) with 11 mM chloroauric acid ($HAuCl_4$, Sigma-Aldrich, St. Louis, MO, USA) at room temperature for 12 h. The reducing agent, dimethylamine borane (DMAB) (Sigma-Aldrich) was added at a concentration of 1.1 mM. After 5 min at room temperature, the remaining Au(III) ion and DMAB were removed by centrifugation at 5,000 rpm for 5 min. The resulting pellet was resuspended in PBS.

2.2. Characterization studies of AuNC incorporated DNA nanoballs

RCA product (RP), RCA product mixed with gold ion (AuRP), and gold nanocluster-incorporated DNA nanoballs (AuDNB) were characterized by morphology, size, zeta potential, and UV-Vis spectrum. The size of RP, AuRP, and AuDNB were measured by dynamic light scattering. The zeta potentials of RP, AuRP, and AuDNB were also measured by laser Doppler microelectrophoresis at an angle of 22^o using an ELSZ-1000 instrument (Photal, Osaka, Japan). The morphology of RP and AuDNB was examined by transmission electron microscopy (TEM, JEM-2100F, JEOL, Tokyo, Japan) and the elements distribution analysis was conducted by energy dispersive

spectrometer (EDS) attached to the JEM-2100F instrument. The absorption spectra of RP, AuRP, and AuDNB were measured over the range of 400-800 nm at a DNA concentration of 240 ng/μL using a UV-vis spectrophotomter (UV-3100, Shimadzu Corp., Tokyo, Japan).

2.3. Photoresponsiveness study of AuNC incorporated DNA nanoballs

Photothermal properties were measured using an IR thermal imaging system after irradiation using an 808 nm NIR laser (PSU-FC, ChangChun New Industries Optoelectronics Tech. Co., LTD, Changchun, China) with an output power of 1.5 W. The temperature and photothermal images of the RP, AuRP, and AuDNB were recorded every 1 min using an IR thermal imaging system (FLIR T420, FLIR Systems Inc., Danderyd, Sweden).

2.4. Cell culture

Human T-cell acute lymphoblastic leukemia (CCRF-CEM) cells (Korean Cell Line Bank, Seoul, Republic of Korea) were culture in RPMI-1640 medium

(Welgene, Daegu, Republic of Krea) supplemented with 10 % fetal bovine serum and 100 units/mL penicillin plus 100 μg/mL streptomycin. The cells were grown at 37 ^{o}C in a humidified 5 % CO_2 atmosphere.

2.5. Laser irradiation of cells treated with gold incorporated DNA nanoballs

CCRF-CEM cells were seed into 24 well plates at a density of 8 x 10^4 cells/well. After overnight incubation, the cells were treated for 30 min with RP, AuRP, or AuDNB at a DNA concentration of 24 μg/mL. The cell suspensions were centrifuged at 800 rpm for 3 min. The cell pellets were monitored using a digital camera (Canon PC1089, Canon Inc., Tokyo, Japan). The harvested cells were irradiated with NIR laser at an output power of 1.5 W. The temperature and photothermal images of the cells during irradiation were recorded every 1 min using an IR thermal imaging system (FLIR T420).

2.6. Cell viability assay following laser irradiation

In vitro photothermal anticancer effect of AuDNB was assessed using 3-(4, 5-dimethylthiazol-2-yl)-2, 5-diphenyltetrazolium bromide (MTT, Sigma-Aldrich) assay after treatment with RP, AuRP, and AuDNB following laser irradiation. For quantative cell viability test, 0.5 mM of MTT solution was added to the cells and incubated for 2 h and the absorbance was measured at 570 nm using a microplate reader (Tecan Group Ltd., Seestrasse, Mannedorf, Switzerland). The values were expressed as a percentage of cell viability of control cells. Live cells were stained with 2 μM of calcein-AM (Invitrogen Corp., Carlsbad, CA, USA) and observed using fluorescence microscopy (Leica DM IL, USA).

2.7. Statistics

All data were statistically analyzed using ANOVA with post hoc Student-Newman-Keuls test. SigmaStat software (version 3.5, Systat Software, Richmond, CA, USA) was used for analyses, and a p-value less than 0.05 was considered statistically significant.

3. Results

3.1. Characterization of AuNC incorporated DNA nanoballs

The structures of RP, AuRP, AuDNB are illustrated in Fig. V-1. The diameter (Fig. V-2E) and zeta potential (Fig. V-2F) of RP was 1275.0 nm ± 272.0 nm and -29.2 mV ± 7.5 mV, respectively. Incubation with Au(III) ion did not significantly alter the size and zeta potential of RP. Reduction by DMAB using Au(III) ion reduced the size to 230.7 nm ± 20.9 nm, but maintained the zeta potential as -25.7 mV ± 0.4 mV. TEM showed the morphology of RP and AuDNB (Fig.V-2A, V-2C). TEM image of AuDNB revealed ball-like nanosized structure (Fig. V-2C) and EDS analysis showed that AuNCs were located inside of the DNA (Fig. V-2D). Only UV-vis spectra of AuDNB showed a characteristic peak at around 580 nm which was not shown in UV-vis spectra of RP and AuRP (Fig. V-2G).

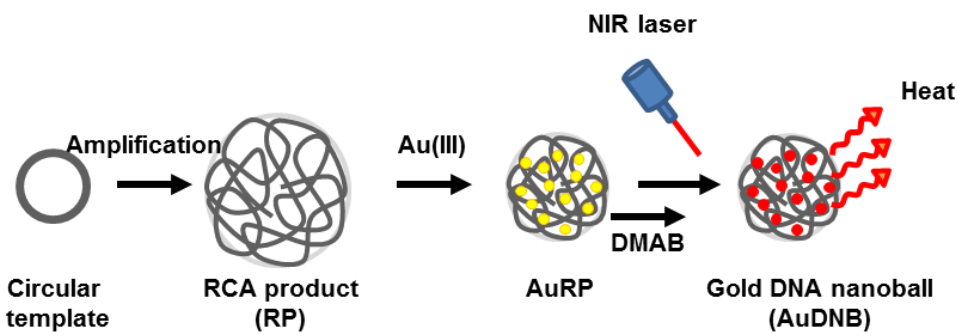

Fig. V-1. Schematic illustration of AuDNB preparation

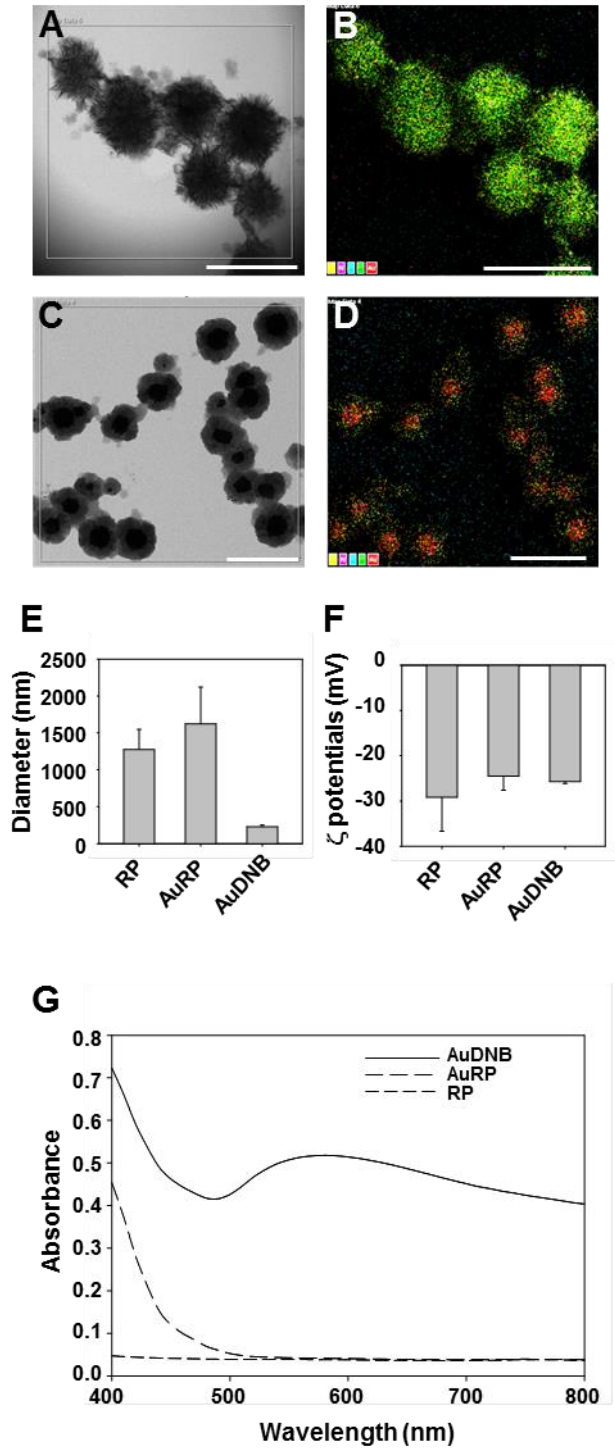

- continued next page -

Fig. V-2. Characterization of AuDNBs

The morphology of RP (A) (scale bar, 2.5 μm) and AuDNB (C) (scale bar, 500 nm) was observed by TEM. Atom composition of RB (B) (scale bar, 2.5 μm), and AuDNB (D) (scale bar, 500 nm) was analyzed by EDS mapping . (Red;gold, green; phosphorous, yellow; oxygen, sky blue; carbon, purple; nitroen). (E) The sizes of RP, AuRP and AuDNB were measured by dynamic light scattering. (F) Zeta potential values of RP, AuRP, and AuDNB were determined by laser Doppler microelectrophoresis at an angle of 22^{o} using ELISZ-1000 instrument. (G) UV-vis absorbance spectrum were measured by UV-vis spectrophotometer.

3.2. Photothermal activity of AuNC loaded DNA nanoballs

Photothermal activity of RP, AuRP, and AuDNB were measured. Upon irradiation with laser, RP and AuRP showed little increase of temperature (Fig. V-3). The temperature increase after 5 min of irradiation for RP and AuRP was 3.5 ^{o}C ± 0.4 ^{o}C, 2.8 ^{o}C ± 0.4 ^{o}C. In contrast, AuDNB exhibited the largest temperature increase, 30.4 ^{o}C ± 0.6 ^{o}C, after 5 min of NIR irradiation.

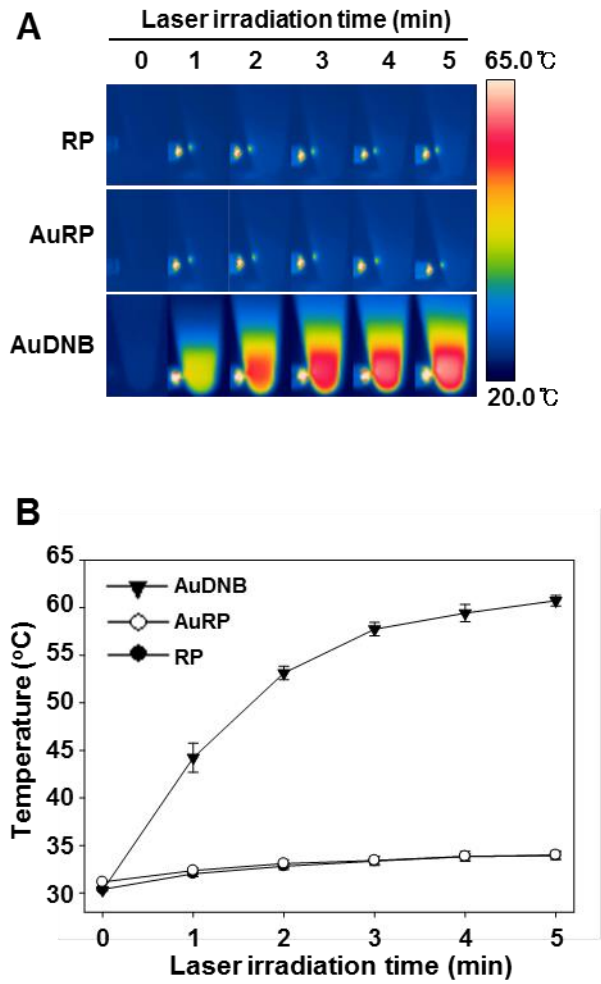

Fig. V-3. Photothermal activity of AuDNB.

(A) Thermal images of RP, AuRP, and AuDNB at DNA concentration of 240 μg/mL with NIR laser irradiation were taken by IR thermal imaging systems every 1 min. (B) Temperature changes of RP, AuRP, and AuDNB suspesnion followed by NIR laser irradiation were monitored.

3.3. Photothermal cell-killing effect of AuNC incorporated DNA nanoballs

Consistent with photoresponsiveness of RP, AuRP and AuDNB, only AuDNB induced temperature increase after treatment to cells followed by irradiation. RP and AuRP did not change the temperature. In contrast, the temperature increased upto 51.0 ^{o}C ± 2.5 ^{o}C in AuDNB treated cells (Fig.V-4C). Since the temperature increase was little after treatment of RP or AuRP followed by irradiation, the cell viability was similar to that of untreated cells. Unlike these, AuDNB with NIR laser irradiation exerted the greatest photothermal cancer cell-killing effect, showing the cell viability was 48.6 % ± 1.5 % (Fig. V-5).

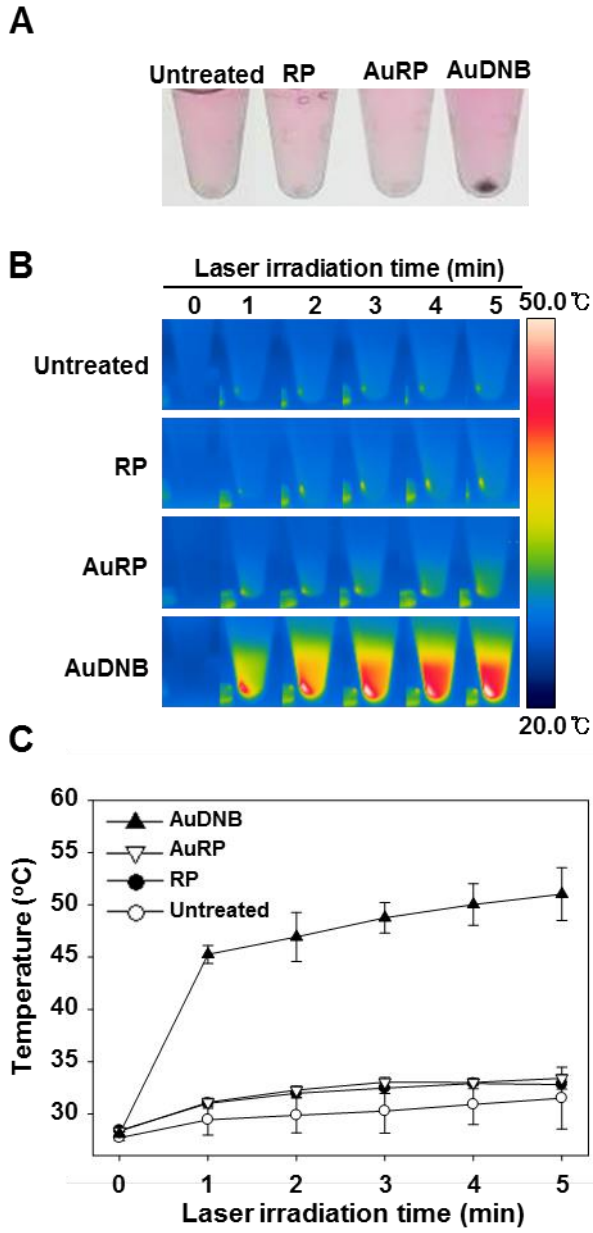

- continued next page -

Fig. V-4. Temperature increase in cancer cells treated with AuDNB.

(A) Optical images of CCRF-CEM cell pellets after 30 min incubation with RP, AuRP and AuDNB were taken by digital camera. (B) Thermo images of cell pellets treated with RP, AuRP, and AuDNB followed by 808 nm laser irradiation were recorded by IR thermal imaging systems every 1 min. (C) Temperature changes in cell pellets treated with RP, AuRP, and AuDNB were monitored simutaneously.

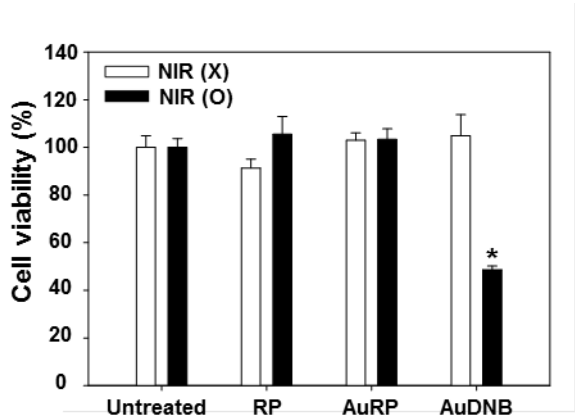

Fig. V-5. In vitro anticancer effect of AuDNB.

CCRF-CEM cells were treated with RP, AuRP or AuDNB for 30 min. Harvested cells were irradiated by 808 nm laser for 5 min.. After incubation for an additional 24 h, the cell viability was measured by MTT assay. The data are presented as the means ± SE (n=3) (*$p < 0.05$ compared to other gr oups; ANOVA and Student-Newman-Keuls test).

4. Discussion

Here, AuNCs loaded DNA nanoballs generated heat after NIR laser irradiation. Moreover, RP which is composed of long ssDNA can be used as stabilizer for AuNCs synthesis and the size of RP decreased during gold reduction. The AuDNB treatment with NIR 808 nm laser irradiation to human leukemia cells decreased cell viability because of high temperature.

TEM images revealed that RP alone showed micrometer size sphere (Fig. V-2A). This result is consistent with previously reported RCA-based nanomaterial [26,27]. After reduction of Au(III) ion, the DNB size decreased to around 200 nm (Fig. V-2C, V-2E). The DNA condensation mechanism is unclear. But the hypothesis is that binding between gold atom and DNA might be maintained after AuNCs formulation because AuNCs located in ssDNA has been demonstrated previously [28]. Thus, in AuDNB system, AuNCs act as photothermal component as well as DNA condensing material. The zeta potential values of RP, AuRP, and AuDNB were not statistically different each other (Fig. V-2F). This results are consistent with EDS analysis observation that AuNCs are located inside of DNA ball-like structure rather than its surface (Fig. V-2D).

Various materials such as protein [29], DNA [28], and synthetic polymer [30] have been used as stabilizer for AuNC synthesis. Here, we firstly demonstrated AuNC synthesis with RCA product. The formation of AuNCs under the condition existing long ssDNA was confirmed by exhibiting an absorbance peak at around 580 nm because AuNCs are known to show a characteristic absorbance at a range from 556 nm to 585 nm [29].

AuDNB showed great PTT activity followed by NIR laser irradiation (Fig. V-3). Because of AuNCs in RCA product, AuDNB could absorb NIR light (Fig.V-2G). It was hypothesized that long ssDNA could incorporate larger amount of AuNCs than that of short ssDNA. The assembly consisted of high amount of AuNCs might give AuDNB photothermal activity and the photothermal activity of AuDNB was high enough to kill the cancer cells (Fig.V- 4,V-5).

The cellular uptake mechanism of AuDNB is not investigated in this study. However, black cell pellet was observed after treatment with AuDNB which means that AuDNB is taken up by cells or bound to the cell membrane (Fig. V-4A). Consistent with this observation, CCRF-CEM cells treated with thiazole orange-loaded AuDNB also showed fluorescence by flow cytometry (data not shown).

It would be necessary to clarify cellular uptake mechanism and conduct in vivo safety study which compares with traditional gold nanoparticles or gold nanorods. Even there was in vitro photothermal anticancer effect of AuDNB, in vivo efficacy study would be also conducted because DNA is degradable in physiological condition easily. However, it is possible that AuNC could improve stability of DNA because it condensed the RP like Mu peptide condensed DNA nanoballs showed resistance against DNase.

In conclusion, AuNC loaded DNA nanoballs were prepared and identified their physicochemical properties. AuNC was formed under the condition existing long ssDNA and located inside of the RCA product simultaneously. The AuDNB showed photothermal activity after NIR laser irradiation and the temperature increase was enough to kill the cancer cells.

5. References

[1] Goldberg SN, Gazelle G.S, Mueller PR. Thermal ablation therapy for focal malignancy. AJR Am J Roentgenol. 2000; 174: 323–331.

[2] Maltzahn GV, Park JH, Agrawal A, Bandaru NK, Das SK, Sailor MJ, Bhatia SN. Computationally guided photothermal tumor therapy using long-circulating gold nanorod antennas. Cancer Res. 2009; 69: 3892-3900.

[3] Wang Y, Black KC, Luehmann H, Li W, Zhang Y, Cai X,Wan D, Liu SY, Li M, Kim P, Li ZY, Wang LV, Liu Y, Xia Y. Comparison study of gold nanohexapods, nanorods, and nanocages for photothermal cancer treatment. ACS Nano. 2013; 7: 2068-2077.

[4] Moon HK, Lee SH, Choi HC. In vivo near-infrared mediated tumor destruction by photothermal effect of carbon nanotubes. ACS Nano. 2009; 3: 3707-3713.

[5] Huang X, El-Sayed IH, Qian W, El-Sayed MA. Cancer cell imaging and photothermal therapy in the near-infrared region by using gold nanorods. J Am Chem Soc. 2006; 128: 2115-2120.

[6] Yang K, Zhang S, Zhang G, Sun X, Lee S-T, Liu Z. Graphene in mice: ultrahigh in vivo tumor uptake and efficient photothermal therapy. Nano Lett. 2010; 10: 3318-3323.

[7] Robinson JT, Tabakman SM, Liang Y, Wang H, Casalongue HS, Vinh D, Dai H. Ultrasmall reduced graphene oxide with high near-infrared absorbance for photothermal therapy. J Am Chem Soc. 2011; 133: 6825-6831.

[8] Zha Z, Yue X, Ren Q, Dai Z. Uniform polypyrrole nanoparticles with high photothermal conversion efficiency for photothermal ablation of cancer cells. Adv Mater. 2013; 25: 777-782.

[9] Yang K, Xu H, Cheng L, Sun C, Wang J, Liu Z. In vitro and in vivo near-infrared photothermal therapy of cancer using polypyrrole organic nanoparticles. Adv Mater. 2012; 24: 5586-5592.

[10] Chen M, Fang X, Tang S, Zheng N. Polypyrrole nanoparticles for high-performance in vivo near-infrared photothermal cancer therapy. Chem Commun (Camb). 2012; 48: 8934-8936.

[11] Yang J, Choi J, Bang D, Kim E, Lim EK, Park H, Suh JS, Lee K, Yoo KH, Kim EK, Huh YM, Haam S. Convertible organic nanoparticles for near-

infrared photothermal ablation of cancer cells. Angew Chem Int Ed Engl. 2011; 50: 441-444.

[12] Zhang D, Wu M, Zeng Y, Wu L, Wang Q, Han X, Liu X, Liu J. Chlorin e6 conjugated poly(dopamine) nanospheres as PDT/PTT dual-modal therapeutic agents for enhanced cancer therapy. ACS Appl Mater Interfaces. 2015; 7: 8176-8187.

[13] Chen WR, Adams RL, Higgins AK, Bartels KE, Nordquist RE. Photothermal effects on murine mammary tumors using indocyanine green and an 808-nm diode laser: an in vivo efficacy study. Cancer Lett. 1996; 98: 169-173.

[14] Zheng X, Xing D, Zhou F, Wu B, Chen WR. Indocyanine green-containing nanostructure as near infrared dual-functional targeting probes for optical imaging and photothermal therapy. Mol Pharm. 2011; 8: 447-456.

[15] Jian WH, Yu TW, Chen CJ, Huang WC, Chiu HC, Chiang WH. Indocyanine green-encapsulated hybrid polymeric nanomicelles for photothermal cancer therapy. Langmuir. 2015; 31: 6202-6210.

[16] De Jong WH, Hagens WI, Krystek P, Burger MC, Sips AJ, Geertsma RE. Particle size-dependent organ distribution of gold nanoparticles after

intravenous administration. Biomaterials. 2008; 29: 1912-1919.

[17] Zhang XD, Wu D, Shen X, Liu PX, Yang N, Zhao B, Zhang H, Sun YM, Zhang LA, Fan FY. Size-dependent in vivo toxicity of PEG-coated gold nanoparticles. Int J Nanomedicine. 2011; 6: 2071-2081.

[18] Zhang XD, Wu D, Shen X, Liu PX, Fan FY, Fan SJ. In vivo renal clearance, biodistribution, toxicity of gold nanoclusters. Biomaterials. 2012; 33: 4628-4638.

[19] Chen L, Wang C, Yuan Z, Chang H. Fluorescent gold nanoclusters: recent advances in sensing and imaging. Anal Chem. 2015; 87: 216−229.

[20] Le Guevel X. Recent advances on the synthesis of metal quantum nanoclusters and their application for bioimaging. IEEE J Sel Top Quantum Electron. 2014; 20: 1−12.

[21] Shang L, Stockmar F, Azadfar N, Nienhaus GU. Intracellular thermometry by using fluorescent gold nanoclusters. Angew Chem Int Ed. 2013; 52: 11154−11157.

[22] Zhang L, Wang E. Metal nanoclusters: new fluorescent probes for sensors and bioimaging. Nano Today. 2014; 9: 132−157.

[23] Zhang Z, Ali MM, Eckert MA, Kang DK, Chen YY, Sender LS, Fruman DA,

Zhao W. A polyvalent aptamer system for targeted drug delivery. Biomaterials. 2013; 34: 9728-9735.

[24] Sun W, Jiang T, Lu Y, Reiff M, Mo R, Gu Z. Cocoon-like self-degradable DNA nanoclew for anticancer drug delivery. J Am Chem Soc. 2014; 136: 14722-14725.

[25] Kim M-G, Shon Y, Miao W, Lee J, Oh Y-K. Biodegradable graphene oxide and polyaptamer DNA hybrid hydrogels for implantable drug delivery. Carbon. 2016; 105: 14-22.

[26] Roh YH, Lee JB, Shopsowitz KE, Dreaden EC, Morton SW, Poon Z, Hong J, Yamin I, Bonner DK, Hammond PT. Layer-by-layer assembled antisense DNA microsponge particles for efficient delivery of cancer therapeutics. ACS Nano. 2014; 8: 9767-9780.

[27] Lee JB, Hong J, Bonner DK, Poon Z, Hammond PT. Self-assembled RNA interference microsponges for efficient siRNA delivery. Nat Mater. 2012; 11: 316-322.

[28] Liu G, Shao Y, Wu F, Xu S, Peng J, Liu L. DNA-hosted fluorescent gold nanoclusters: sequence-dependent formation. Nanotechnology. 2013; 24: 015503.

[29] Lin J, Zhou Z, Li Z, Zhang C, Wang X, Wang K, Gao G, Huang P, Cui D. Biomimetic one-pot synthesis of gold nanoclusters/nanoparticles for targeted tumor cellular dual-modality imaging. Nanoscale Res Lett. 2013; 8: 170.

[30] Chen Y, Zheng X, Wang X, Wang C, Ding Y, Jiang X. Near-infrared emitting gold cluster-poly(acrylic acid) hybrid nanogels. ACS Macro Lett.

2014; 3: 74-76.

Conclusion

For effective cancer treatment, targeted anticancer drug delivery is necessary. Effective PTK7 overexpressed cancer targeted delivery system was developed using PTK7-binding polyaptamer and rGO nanosheets. In CCRF-CEM xenografted mice model, PNTrGO showed very high tumor tissue accumulation and more effective inhibited tumor growth.

Not only chemical drugs, but also nucleic acid therapeutics are considered as promising anticancer agents. DNA nanoballs were designed as various ASO loadable carrier for targeting against CD44 overexpressed cancer using RCA product, Mu peptide, and HA. HMA nanoballs effectively delivered Dz13 and OGX-427 to KB cells via CD44 receptor-medicated endocytosis.

Two types of novel PTT agents were suggested. First, facile TA-Fe coating technology was applied to BNNS. TA-Fe/BNNS showed phototheraml activity and it was enough to induce anticancer effect both in vitro and in vivo. Secondly, we demonstrated AuNC-loaded DNA nanoballs for PTT. The long ssDNA produced by RCA could carry AuNCs followed by condensing via AuNCs. AuDNB showed notable temperature increase and induced cancer cell killing

effect with NIR laser irradiation.

In this study, two dimensional nanosheets structures and RCA technology has been applied to anticancer drugs delivery for targeted delivery and photothermal therapy against cancer. Two dimenstional nanostucrues could deliver drugs and play a role as backbone material for surface coating technique. RCA technology was useful to produce targeting moiety and ASO nanocarrier. Nanostructure-based targeted drug delivery systems and nanomaterials for photothermal therapy are promising strategies for cancer therapy.

요약

나노구조체 기반 약물 표적 전달 및 광열치료

서울대학교 대학원

약학과 약제과학전공

박주연

표적 약물 전달은 항암제의 치료효과를 증진시키는 유망한 전략 중의 하나로 여겨져 왔다. Protein tyrosine kinase 7 (PTK7)에 특이적으로 결합하는 것으로 알려진 DNA aptamer의 반복서열인 polyaptamer nanothread가 rolling circle amplification (RCA) 기술을 통하여 합성되었고, 환원 그래핀 나노시트 (rGO)에 polyaptamer nanothread를 수식하여 PTK7 과발현 세포주에 항암제 전달 효율을 증진시켰다. 또한

polyaptamer nanothread가 수식된 rGO (PNT/rGO)는 PTK7 과발현 암종이 이식된 쥐에 정맥주사를 통해 항암제인 doxorubicin을 효과적으로 전달하여 암의 성장을 억제하였다. RCA 기법을 통해 antisense oligonucleotide (ASO)에 상보적인 서열을 갖는 DNA nanoball을 제조하였다. Dz13과 OGX-427이 DNA nanoball에 탑재되었고, Mu peptide와 히알루론산(HA)으로 수식되어 CD44를 과발현하는 암세포에 전달하였다. Dz13과 OGX-427을 탑재한 DNA nanoball은 효과적으로 타겟 mRNA와 단백질의 발현을 억제하였고, 세포 수준과 암이식 쥐 모델에서 뛰어난 항암효과를 보였다. 광열치료는 강력하고, 상대적으로 비침습적인 암치료법으로 연구되고 있다. 본 연구에서는 탄닌산 (TA)과 철의 킬레이트 화합물에 의해 표면이 개질된 boron nitride nanosheets (BNNSs)를 안전하고 새로운 광열 치료 물질로 제시하였다. TA-Fe/BNNS는 근적외선 레이저 조사에 의해 온도가 올라가는 광감응성을 보였고, TA-Fe/BNNS의 광열효과는 암세포주의 세포사멸을 유도하였고, 암이 이식된 쥐 모델에 국소 투여 되었을 때 암조직을 완전히 제거하였다. 마지막으로, 금 나노클러스터가 봉입된 DNA nanoball (AuDNB)을 RCA 기술을 통하여 제조하였고, AuDNB는 근적외선 조사에 의한 광열효과를 나타내었다. 또한 AuDNB를 암세포주에 처리하고, 근적외선을

조사함으로써 AuDNB의 광열 효과에 의한 암세포 사멸효과를 확인하였다.

주요어: Targeted drug delivery, photothermal therapy, rolling circle amplification, reduced graphene oxide, boron nitride nanosheet, tannic acid–Fe coating, gold nanocluster